Interplay between superconductivity and spin polarization in thin-film bilayers

An experimental study

Trude Bjørgås Hjelmeland

Thesis submitted for the degree of
Master of Science in Physics
60 credits

Department of Physics
Faculty of Mathematics and Natural Sciences

UNIVERSITY OF OSLO

Spring 2018

Interplay between superconductivity and spin polarization in thin-film bilayers

An experimental study

Trude Bjørgås Hjelmeland

Interplay between superconductivity and spin polarization in thin-film bilayers

http://www.duo.uio.no/

Printed: The University Print Centre

Abstract

This project is focused on studying the interplay between superconductivity and ferromagnetism in heterostructures of the high temperature superconductor $YBa_2Cu_30_{7-\delta}$ (YBCO) and the highly spin-polarized manganite $La_{0.76}Ca_{0,33}MnO_3$ (LCMO).

One will see that the two materials competing order parameters lead to fascinating and novel physics emerging close to their interface, like resistive states found both when the superconductor is in its normal and superconducting phase.

A short introduction will be given, outlining main objectives, followed by a brief theory section where high temperature superconductors and colossal magnetoresistive manganites are presented. Then experimental methods utilized will be described, with focus on the two main techniques: electrical transport measurements and magneto-optical imaging. Results are presented and discussion is given. For the most eager reader, an extensive appendix is added, containing a more sizeable review on conventional superconductors, experimental results not found in main part, some critical reflection comparing local and global resistance for the samples, Matlab scripts and two conference articles that came from the work performed for this thesis.

Acknowledgements

This master thesis concludes my degree in Condensed Matter Physics at the Department of Physics.

First and foremost I would like to thank my supervisor, Associate Professor Pavlo Mikheenko, for his teaching and wise guidance. Your extraordinary enthusiasm for the field has served as a continued inspiration throughout this process. Thank you for providing samples, experimental equipment and helium to facilitate the experimental work performed for this thesis, and for your critical review of my thesis.

Thanks to everyone associated with the superconductivity group, especially Professor Tom Henning Johansen, Ph.D candidate Thomas Håbu Qureishy and fellow master student Hans Jakob Mollatt. Thank you Tom Henning for providing magneto-optical indicator films. Thank you Thomas for teaching me to run the magneto-optical imaging setup, and for guiding and supervising my use of the scanning electron microscopy at the research park. Our discussions and weekly chats have always put a smile on my face. Thank you Hans for teaching me to use the transport measurement equipment and for letting me continue the research you started.

Gratitude is given to Asbjørn Slagtern Fjellvåg and Øystein Slagtern Fjellvåg at the Department of Chemistry for obtaining and analysing magnetic measurements and x-ray diffraction patterns. Thank you, Ole-Bjørn Karlsen, for teaching me how to operate the table top scanning electron microscopy and utilizing its energy dispersive spectrometer. Atomic force microscopy was possible thanks to Anja Røyne for letting us use the equipment at her laboratory and to Kjell-Erik Kvamsdal for helping me obtain the measurements. Thank you, Professor S.Soltan, for our inspirational scientific correspondence and your comments on obtained experimental results. You are a legend within this field of research.

Finally, I want to give a very special thank you to my love, Carl-Axel, for his continued support and encouragement throughout this exciting, but at times frustrating journey. You always know exactly what to say and without you this would never have been possible.

Contents

List of Figures

CHAPTER 1

Introduction

Superconductivity is both fascinating and useful. With its application for constructing powerful electromagnets, it takes part in activities spanning from investigation of the fundamental particles in the universe to the inside of the human body. Recently, superconductors have been incorporated into traps for transport of antimatter and have shown big potential in the fields of quantum computing, quantum entanglement and spintronics.

Colossal magnetoresistive (CMR) materials have found use as magnetic field sensors, where their large change in resistance as function of applied magnetic field have been utilized. As these materials have strongly correlated electron system, a large variety of properties emerges as a consequence of strong coupling between spin, charge, lattice and orbital degrees of freedom, like half-metallicity, offering the possibility to create highly spin-polarized currents.

Spintonics is the field of research in which the electrons spin degree of freedom is utilized in addition to or rather in combination with its charge. Spintronic-based devices have already been realized in memory storage, spin field-effect transistors and spin-valves. In the future, there is hope for spin-based qubits as the principal components of quantum computers.

The high temperature superconducting compound $YBa_2Cu_3O_{7-\delta}$ (YBCO) and the CMR material $La_{1-x}Ca_xMnO_3$ have very similar crystal structure and lattice parameters, which make these materials suitable for epitaxially grown heterostructures with transparent interfaces due to little strain. These heterostructures serve as excellent candidates for studying the two materials' competing order parameters to clarify how they interact: whereas ferromagnetism tends to align spin in one direction, the superconductivity is based on paring of electron with opposite spin.

My fascination for the concept of a dissipation less current lead me to write a project about superconductivity for my condensed matter physics course. This gave me a basic theoretical understanding of the concept of superconductivity and I familiarised myself with all its amazing applications, in everything from levitating trains to particle accelerators. Through this project, I was introduced to the superconductivity laboratory and its research group, and in my first visits I was impressed by demonstrations of levitation experiments, even with a

small-scale levitating train. After that my interest for superconductivity grew even larger.

Simultaneously, another very interesting activity was going on: a novel resistive state had been observed experimentally in a bilayer thin film of YBCO and $La_{0.67}Ca_{0.33}MnO_3$ (LCMO), a highly spin-polarized half metal, with the electrical transport measurement setup. The experimentalist in me wanted to know more. And as a matter of luck, the possibility to do a master under the supervision of Pavlo Mikheenko appeared, and I joined the current research project and later continued to investigate similar thin films.

The main objectives for this thesis have been to further clarify the origin of the resistive state found below the superconducting transition in the bilayer of LCMO and YBCO. Then through work on similar systems, it became clear that the experimental work would evolve into a study of the effect of polarized spin injection into both the superconducting and normal state of the high temperature superconductor, namely YBCO.

CHAPTER 2

Theory

2.1 Superconductivity

In 1911, Heinke Kamerlingh Onnes and his assistant discovered a new state of matter that was named superconductivity. This state is characterized by zero resistivity below a critical temperature, T_c. Later it was found that superconductivity have more critical parameters that must not be exceeded for the material to be in its superconducting state. Namely, these are critical magnetic field, H_c, and critical current density, j_c. There is an intimate relationship between these critical parameters, as shown in figure 2.1 in the form of a critical surface. Coordinates of any point on the critical surface give the critical values of the parameters. When one of these parameters moves towards its critical value, the other two must move towards zero for the material to stay in its superconducting state.

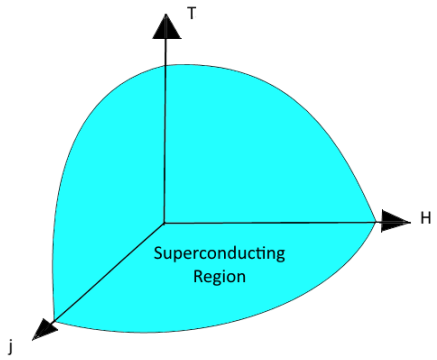

Figure 2.1: The figure shows the relationship between the critical parameters T_c, H_c and j_c as a critical surface.

Later experiments have shown that superconductors are not only perfect conductors but also perfect diamagnets, expelling magnetic flux from their interior. This effect is known as Meissner effect. It is this amazing property that allows superconductors to levitate above, or suspend under, magnets.

It has been shown that two different types of superconductors exist, which have

different behaviour in a magnetic field, and this difference is defined by the surface energy of the interface between a superconducting and normal state. Type I superconductors are found to have positive surface energy and only allow magnetic flux to penetrate close to its surface at a depth known as the London penetration depth, λ_L. Type II superconductors have negative surface energy, favouring the creation of many interfaces, and magnetic flux is allowed to penetrate as vortices with quantized values of magnetic flux, for magnetic fields between two critical values, H_{c1} to H_{c2}, in a structure known as Abrikosov lattice.

The mechanism allowing for superconductivity is the paring of electrons into Cooper pairs, where the two constituents are thought to have opposite spin and momentum. Thus, two electrons form a composite boson, allowing them to follow Bose-Einstein statistics, and condensate on the same ground state, as they are no longer obeying the Fermi-Dirac statistics, and can move without dissipation as long as the pairs are in phase.

For a more extensive review of conventional superconductors and how they differ from unconventional superconductors, the reader is referred to appendix A.

2.1.1 Discovery of high-temperature superconductors (HTSC)

In the decades to follow Kamerlingh Onnes's discovery, superconductivity was found to exist in other elements and simple alloys with their critical temperatures shown by the green line in figure 2.2. This line represents conventional superconducting materials. The discoveries behind it slowly raised the values of the critical temperature, making applications more feasible [15].

The real breakthrough for superconductivity came in 1986 when Alex Müller and Johannes Georg Bednorz associated with the IBM laboratory in Switzerland found superconductivity in a brittle ceramic compound comprised of lanthanum, barium, copper and oxygen, with a critical temperature of 35 K [12]. It was a considerable jump in T_c from 23 K for the compound niobium germanium discovered to be superconducting 13 years earlier. Müller and Bednorz's discovery marked the start for a new category of superconductors, high temperature cuprate superconductors. It earned them the Nobel Prize in Physics only one year later and sparked an intense activity on synthesizing other similar ceramic compounds in the quest for yet higher transition temperatures [41].

In 1987, Maw-Kuen Wu and Chu Ching-Wu reported the discovery of superconductivity in a compound of yttrium, barium, copper and oxygen, $YBa_2Cu_3O_{7-\delta}$ (YBCO), with a critical temperature of 93 K [68], well above the boiling temperature for liquid nitrogen (77 K), making this compound more suitable for low-cost applications due to the abundance of nitrogen. In the following years, more cuprate-based superconductors were discovered with increasingly higher critical temperatures as seen from the blue line in figure 2.2. The figure gives a chronological overview of the discovery of superconducting elements and simple compounds (green), cuprate based high temperature superconductors (blue) and the more recent discovery of iron-based superconductors (red) [54].

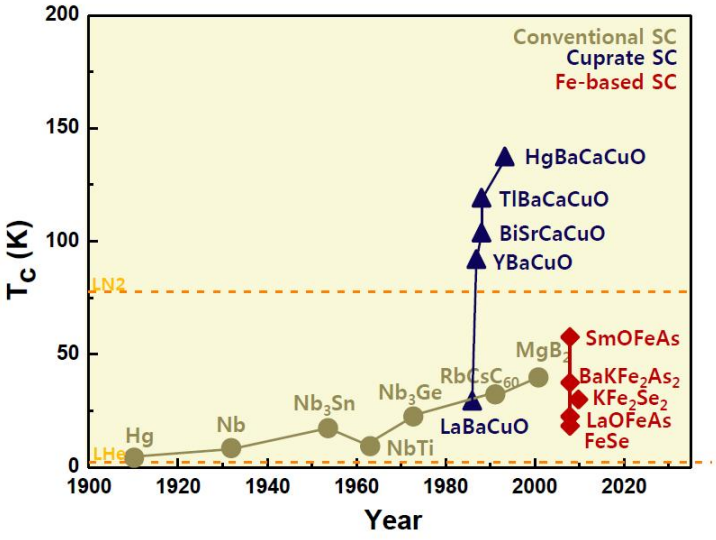

Figure 2.2: Outline of chronological discovery of superconducting materials with their corresponding critical temperature shown on the y-axis. Superconducting materials that exhibit superconductivity under high pressure have been omitted from this figure, taken from [9].

As YBCO is the superconductor investigated in the experimental work performed for this thesis, the following sections will focus on cuprate high temperature superconductors (HTSC) in general and YBCO in particular.

2.1.2 The crystalline structure of cuprate HTSC

Many of the HTSC crystallize in the perovskite structure, which is generalized as an ABO_3 structure [15]. Here O is oxygen and both A and B are cations, i.e. positively charged ions. The A atoms sit at every corner and B in the center of the unit cell, shown as red and green, respectively, in figure 2.3. The oxygen atoms form an octahedron around the B atom and thus sit at all the face centered positions in the unit cell [14], shown as blue in figure 2.3. Many materials crystallize in a distorted version of the lattice shown in figure 2.3.

The specific behaviour of cuprate HTSCs emerges as a consequence of that these compounds contain anionic copper oxides. The following section contains a detailed description of YBCO, both its crystalline structure and physical properties, especially when the oxygen content in this compound is varied.

2.1.2.1 $\mathbf{YBa_2Cu_3O_{7-\delta}}$

YBCO crystallizes in a layered, quasi two-dimensional, distorted perovskite structure. The A positions are occupied by copper atoms, whereas the B positions are occupied by yttrium and barium. Three unit cells are stacked on top of each other along the c-axis, with a Ba-Y-Ba order, forming the basis for the YBCO unit cell shown in figure 2.4. Here the dark blue spheres represent

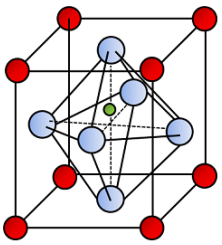

Figure 2.3: The figure shows the schematic crystallographic representation of the perovskite cubic unit cell. The figure is taken from [5] and modified.

barium, the green-yttrium, red-copper and light blue spheres-oxygen. The crystalline structure and physical properties of YBCO vary strongly, depending on the oxygen content in the structurer [62] [54]. The oxygen content is given as $O_{7-\delta}$, where δ varies from 0 to 1.

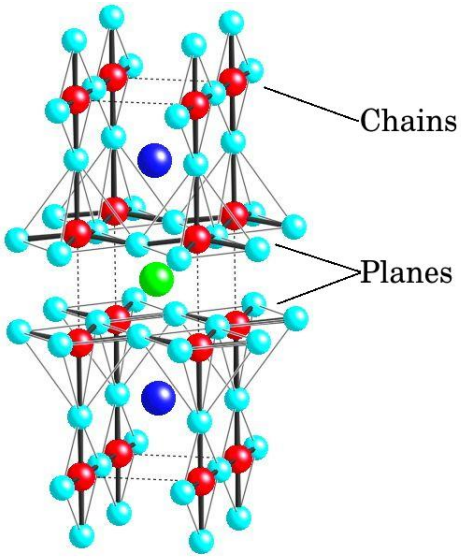

Figure 2.4: The figure shows the schematic crystallographic representation of $YBa_2Cu_3O_7$. The figure is taken from [10] and modified.

For δ equal to one, we have $YBa_2Cu_3O_6$, a non-superconducting antiferromagnetic insulator. The tetragonal distortion of the unit cell is found with lattice parameters a = b = 3.86 Å and c = 11.7 Å [52].

YBCO becomes superconducting for δ smaller then 0.6. For δ equal to zero, the orthorhombic structure of $YBa_2Cu_3O_7$ with lattice parameters a = 3.82 Å, b = 3.89 Å and c = 11.7 Å is formed [52] and its structure is schematically shown in figure 2.4. For YBCO utilized within this thesis, oxygen has been partially removed from the idealized perovskite structure and the material is said to be oxygen deficient (non-stoichiometric). Optimal oxygen content, yielding the highest critical temperature of 92 K, is found experimentally to be for δ very

close to zero.

In its superconducting phase, i.e. for δ smaller then 0.6, the compound contains crystallographic copper oxygen plains and chains [35]. The CuO_2 planes are responsible for the transport of superconducting electrons, while one dimensional copper oxygen chains, along the b-axis, act as charge reservoirs. The latter finds support in the fact that vacancies in the copper-oxygen chains are absent for the non-superconducting $YBa_2Cu_3O_6$ [13]. In this structure, yttrium and barium act as spacers for layers of copper and oxygen, and with weak interaction between the copper-oxygen planes, YBCO transforms from a 3-dimensional to quasi 2-dimensional material.

Like many other high temperature superconductors, YBCO is highly anisotropic between the ab-plane and c-axis direction, which results in anisotropic resistivity above T_c, critical current density, j_c, critical magnetic field, H_c, penetration depth and coherence length.

2.1.3 Applications of superconductors

After Kramerlingh Onnes discovered the first superconducting elements, he quickly realized the important role that superconductors could play for application to coils generating magnetic fields. The low critical field for the elemental superconductors hampered this development. With the later discovery of type II superconductors yielding much higher critical field and critical current density, superconducting coils for high magnetic field generation have become one of their most important applications. Modern superconducting materials are able to provide fields higher than 20 T, much higher than those produced by normal conductors, which is at about 2 T [54].

Today superconducting magnets play a key role providing high magnetic fields needed in particle accelerators, medical equipment, experimental studies, nuclear magnetic resonance spectroscopy, field containments of plasma in fusion reactors [16] and levitating trains. In the future, a hydrogen-based economy could be developed with a superconducting grid as its basic structure optimizing energy efficiency in the sector [43]. In an exciting field of research, quantum computing utilizing superconductors [37] [21], successful 10-qubit entanglement was demonstrated [61], as well as 49, 50 and 72-qubit processors were announced.

2.1.4 Proximity effect and Andreev reflection

Proximity effect is a phenomenon that occurs when a superconductor is in good electrical contact with a normal (non-superconducting) material. Superconducting electrons, united in Cooper pairs, can diffuse into the normal material and induce superconductivity in the proximity of the interface [41]. As the superconducting electrons move in the normal material, they get scattered and the Cooper pairs lose their coherence. The distance, over which coherence persists, depends on properties of the two materials and their interface and has been shown to range from nanometers to microns [41].

When a superconductor (SC) and a ferromagnetic (FM) material are in good

electrical contact, proximity effect tends to be suppressed by the presence of the exchange field, favouring lining the spins in one direction, thus breaking up Cooper pairs.

In thin films of superconducting material in contact with a normal metal, the penetration of Cooper pairs into the normal metal induces superconductivity there, but it also weakens the superconductivity near the interface lowering T_c in the superconductor. If the superconducting layer is thin enough, superconductivity is suppressed altogether [18].

Andreev reflection is a charge transfer process occurring at the interface between a normal metal and a superconductor (SC-N). Here a normal current in N is transformed to a super current in SC through interface scattering. The forbidden single-particle transfer, due to the superconducting gap, is avoided by the reflection of a hole in N with the same momentum as the transmitted electron, but with opposite spin and velocity. In the superconductor, the transmitted electron forms a Cooper pair with another electron that balances the reflected hole and the charge transfer takes place across the interface in the form of 2e quanta. This process is shown in figure 2.5.

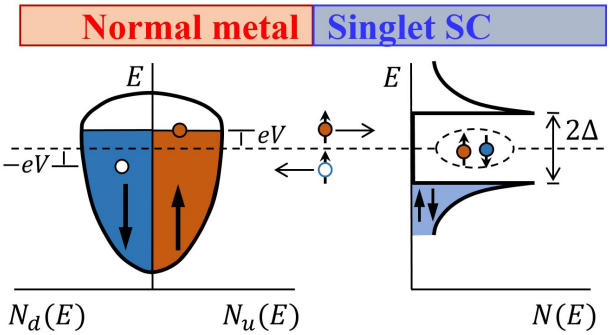

Figure 2.5: Schematic representation of Andreev reflection at the interface between a superconductor and a normal metal. The figure is taken from [27].

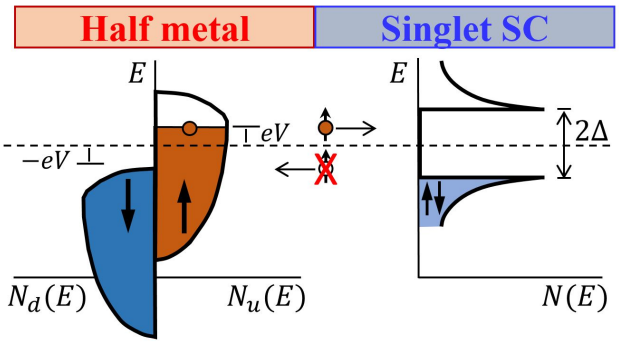

Figure 2.6: Schematic representation of Andreev reflection at the interface between a superconductor and a half-metal. The figure is taken from [27].

Andreev reflection is spin-dependent, so when only one spin band is present at

the Fermi level on the left, like in a half-metal, Andreev reflection is impeded, and in many cases fully suppressed, as seen in figure 2.6 [18] [59].

2.2 Magnetism

Magnetization, M, is defined as magnetic moments per unit volume and magnetic susceptibility, χ, per unit volume is defined in SI-units as $\chi = \frac{M}{H}$, where H is the auxiliary magnetic field.

Materials that exhibit small positive susceptibility are paramagnetic [36]. This allows them to become magnetized by externally applied magnetic fields, when the magnetic moments inside the paramagnetic material tend to line up in the direction of the applied field.

A ferromagnetic material displays spontaneous magnetization due to magnetic moments lining up parallel to each other even without external magnetic field. This can be described as a result of the presence of an internal field called exchange field, B_E, that is competing with thermal fluctuations. Their competition results in spin ordering to be smeared out and vanishing for higher temperatures, causing the material to be paramagnetic. The temperature, for which the material changes its state from being ferromagnetic to paramagnetic is named Curie temperature, T_{Curie}, and the transition from ferromagnetic to paramagnetic state is of second order [36].

2.2.1 Colossal magnetoresistive materials

The perovskite manganites offer a rich field of activities, ranging from fundamental physics research to possible applications in spintronics. This is due to their specific strongly correlated electron system offering strong coupling between charge, spin, orbital and lattice degrees of freedom, leading to a wide variety of properties and complex electronic, magnetic and structural phase diagrams [19] [70].

Colossal magnetoresistive (CMR) manganites typical chemical composition is $RE_{1-x}AE_xMnO_3$, where RE is a trivalent rare-earth element like La, Pr, Sm or Sc and AE is a divalent alkaline-earth ion like Mg, Ca, Ba or Sr [29]. Mn in the compound has a mixed valency of 3+ and 4+, which is strongly affecting magnetic and conduction properties of the material [19].

The magnetoresistance of a material is expressed in a change of its resistivity in the presence of external magnetic fields. This effect was discovered by Volger in 1954 [64], but showed low resistivity changes of only 10%. Later, with the discovery of CMR manganites, resistivity changes of several orders of magnitude have been experimentally documented [70]. One of the most used CMR materials is calcium substituted manganite, $La_{1-x}Ca_xMnO_3$.

From the phase diagram of $La_{1-x}Ca_xMnO_3$ in figure 2.7, one can see the wide variety of phases that emerge as a consequence of the calcium doping in the compound. The CMR manganite used in this work is $La_{0.67}Ca_{0.33}MnO_3$, LCMO. From the phase diagram, one can see that this material is ferromagnetic

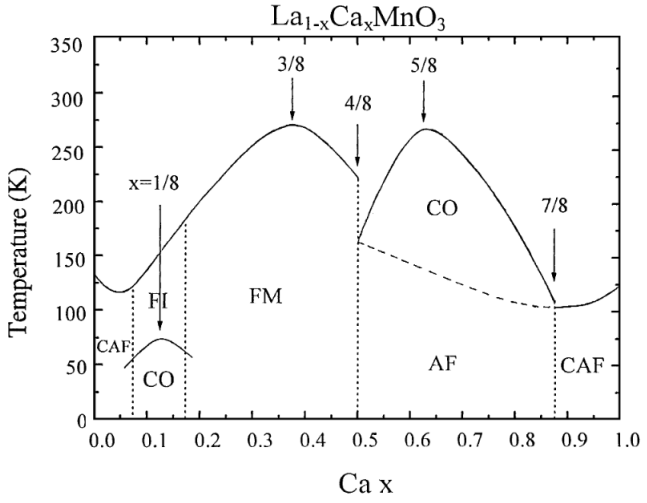

Figure 2.7: Phase diagram for $La_{1-x}Ca_xMnO_3$ as function of both temperature and Ca doping level. Here CAF stands for canted antiferromagnetic, FI for ferromagnetic insolator, FM for ferromagnetic, AF for antiferromagnetic and CO for charge-ordered phase. The figure is taken from [20].

below a temperature of about 250K. Above this temperature, T_{Curie}, the material is paramagnetic.

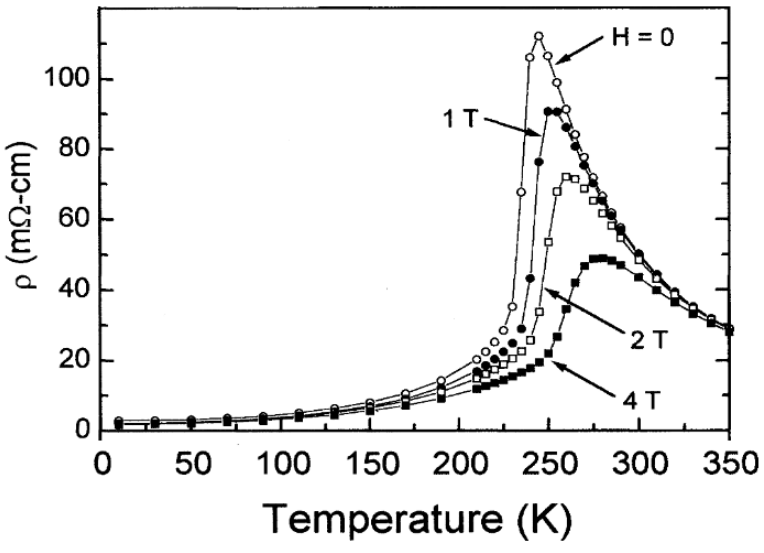

Figure 2.8: Resistivity as function of temperature for $La_{0.67}Ca_{0.33}MnO_3$, displaying its dramatic change at T_{Curie}. The figure is taken from [53] and expresses behaviour of resistivity in strong magnetic fields.

There is a strong change in the materials resistivity associated with the transition from paramagnetic to ferromagnetic phase, as shown in figure 2.8. As the temperature decreases towards T_{Curie}, the resistivity increases like in an isolator. Below T_{Curie}, the resistivity decreases with decrease of temperature exhibiting metal-like resistive behaviour.

An important property of CMR manganites like LCMO is their half-metallicity, which is crucial for the experimental investigation performed in this thesis. As a half-metal, fully polarized spin currents flow in LCMO, with electrons of only one spin direction contributing to the conduction in the material. This takes place because there is a band gap for one of the two spin directions at the Fermi level, [23] as shown schematically to the right in figure 2.9.

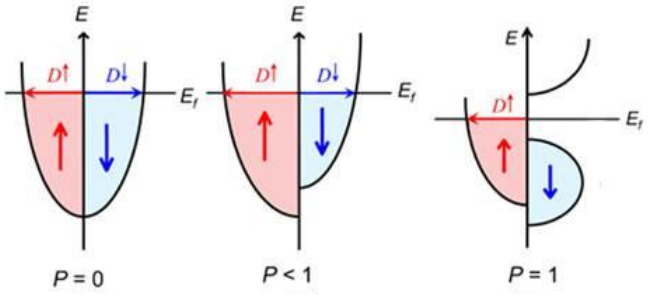

Figure 2.9: Spin density of state (x-axis) as function of energy (y-axis), where E_f indicates the Fermi level, for a paramagnet (left), ferromagnet (middle) and ferromagnetic half-metal (right) with their corresponding polarization as noted under the pictures. The figure is taken from [2].

The electron spin polarization, P, of a magnetic material shown in figure 2.9 is given by the expression:

$$P = \frac{D\uparrow(E_F) - D\downarrow(E_F)}{D\uparrow(E_F) + D\downarrow(E_F)}, \tag{2.1}$$

where $D\uparrow(E_F)$ and $D\downarrow(E_F)$ represent the density of state (DOS) for spin up and down charge carriers components, respectively, at the Fermi energy. The three different systems shown in figure 2.9 give polarization ranging from zero on the left and 100% on the right.

Another important parameter, spin-coherence length, L_s, is the distance over which a spin state persists in a material. Spin-relaxation time is proportional to $1/L_s$. The relaxation occurs as a consequence of two major processes: spin-flip scattering, in which spin-up state can be changed to a spin-down state, and spin dephasing, where the polarization of a current decays in intensity due to varying rate of Larmor precession of the spin.

Spin scattering is a process that does not conserve the spin state and momentum. In ferromagnetic materials, the likelihood of spin scattering is dependent on

the electron spin orientation relative to the magnetic moment of a domain in a material. When the electron spin and orientation of the magnetic domain are parallel, the electron moves more free through the material, compared with the situation when their orientations are antiparallel. This is thought to be because for antiparallel orientation there are more states to scatter in to, increasing the likelihood for scattering [63] and thus increasing the resistivity. This is consistent with Mott's two-currents model [30].

2.2.2 Magnetic proximity effect

Magnetic proximity effect is suppression of the superconducting order parameter due to injection of spin-polarized quasiparticles from a ferromagnetic material into a superconductor. The diffusion length of these quasiparticles is denoted ξ_{FM} and shown experimentally to be about 10 nm [56] [58] .

The spin-polarized quasiparticle injection leads to a non-equlibrium density of spin-polarized charge carriers in vicinity of the interface in the superconductor, which has been shown to be responsible for suppression of the superconducting order parameter, lowering the critical current density, j_c, and breaking Cooper pairs.

2.3 Spintronics

Spintronics is a wide field of research, in which the electrons' spin degree of freedom is employed instead of, or in addition to, its charge. Here spin-polarized currents play a key role. Spintronics-based devices are already in use in memory storage, spin-field effect transistors and spin-valves used for superior current switching. In the future spintronics is expected to play a principal part in the development of quantum computing.

Information processing with spintronic qubits shows a great potential, as it has been shown that spin-dephasing time can be on the order of microseconds in confined nanostructures with dephasing coherence length ranging over micrometers. Superior information processing speed by utilizing spin is another compelling argument.

CHAPTER 3

Experimental Methods

For a student at the University of Oslo a large variety of experimental methods with state of the art equipment are available for scientific study. In the work performed for this thesis a multitude of these have been utilized and will be described in the upcoming sections. The main focus will be on the local equipment at the superconductivity laboratory as this has been the workhorse, building the foundation for the experimental work performed in relation with this thesis. This equipment includes electrical transport measurement and magneto-optical imaging.

3.1 Transport Measurements

Transport measurements have been performed to measure resistance as function of temperature, R(T), and to record current-voltage (IV) characteristics of the sample. The in-house built experimental setup offers a wide range of measuring possibilities. A schematic view of it is shown in figure 3.1. Here the current flow in the circuit is marked with black lines, whereas the information flow during measurements is indicated with red lines. A Matlab script, shown in the appendix D.2, is utilized to register and see the physical quantities during experiments.

The temperature of the sample is measured by a LakeShore 322 Temperature Controller, and both liquid nitrogen and helium provided the cryogenic temperatures needed to perform experiments over a wide range of temperatures. The temperature sensor is in thermal contact with the sample during measurements as seen in figure 3.1. The power supply, Delta Elektronika SM 7020-D, applies a constant voltage set by the operator on the circuit and two multimeters, Keithley 2110 5 1/2, measure the potential drop over both the sample and a variable control resistance. By utilizing Ohm's law, U=RI, both the resistance of the sample and the current in the circuit can be extracted and used for further analysis.

To apply the current and measure the potential drop over the sample, indium contacts are accurately applied to the corners of sample. This gives a range of possibilities on how to measure voltage, and both four and two corner measurements have been performed.

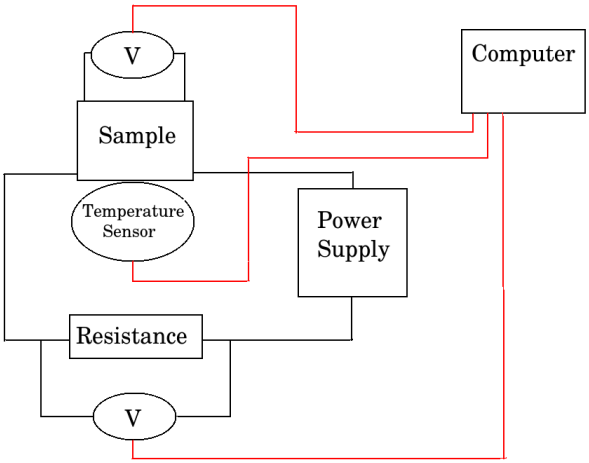

Figure 3.1: The figure shows a schematic overview of the transport measurement setup. The information flow during measurements is shown with red lines.

When only two contacts on the sample corners are used, a technique called two-point measurements, current is passed through and voltage measured on the same contact points. This technique allows for the whole potential drop over the sample to be measured with good accuracy, but the measurements also contain resistance of the contacts, which for our purposes is less desirable.

The four-corner technique is also known as the Montegomery technique [44] and is shown schematically in figure 3.2. Here we use four indium contacts, pass current through two lower contact points and measure the potential drop with two contacts mounted on the opposite side of the sample. This allows to exclude contact resistance from the measurements, but as we will see later some of the potential drop is not captured during the measurements. Steps towards improving this technique have been made by modifying the measurements with a Matlab script included in appendix D.1, which is written by the author. Here measurements are modified by utilizing Kirchoff's circuit laws and assuming no potential drop in the circuit besides over the sample and the constant resistance. A more detailed description will be given towards the end of this section.

We have chosen to use contacts point in the corners and edges of the sample as this allows for a wide range of measuring modes and permits magneto-optical imaging to be performed at a later stage in investigations. This versatility of measurements is of importance for the work performed in the thesis, as will be clear when results are presented in Chapter 4.

As part of the experimental work performed, some improvements have been made for the transport measurement system. Firstly, a small Matlab script have been written which closes all the connections to multimeters and temperature controller allowing for new measurements to be performed without restarting

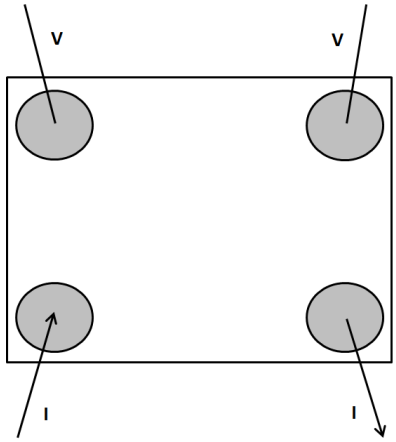

Figure 3.2: A schematic presentation of the Montgomery technique used in four-corner measurements.

Figure 3.3: The figure shows the experimental setup for transport measurements at the superconductivity laboratory at the University of Oslo. The upper picture shows the power supply, the two multimeters and the computer used to process and control the measurements. The lower left picture shows the helium tank utilized, and the lower right picture shows the nitrogen dewar in the background and the sample mounted on the cryogenic rod in the front.

Matlab between subsequent measurements. Secondly, as a consequence of the sample and the temperature sensor not being in direct thermal contact, some hysteresis arises between measurements performed while cooling and heating the sample. To reduce this effect, different wrappings to insulate the sample and sensor were applied. While performing measurements at a slow rate is of importance, a combination of a thin layer of styrofoam and a thick rubber cover yielded satisfactory results, as seen in figure 3.4.

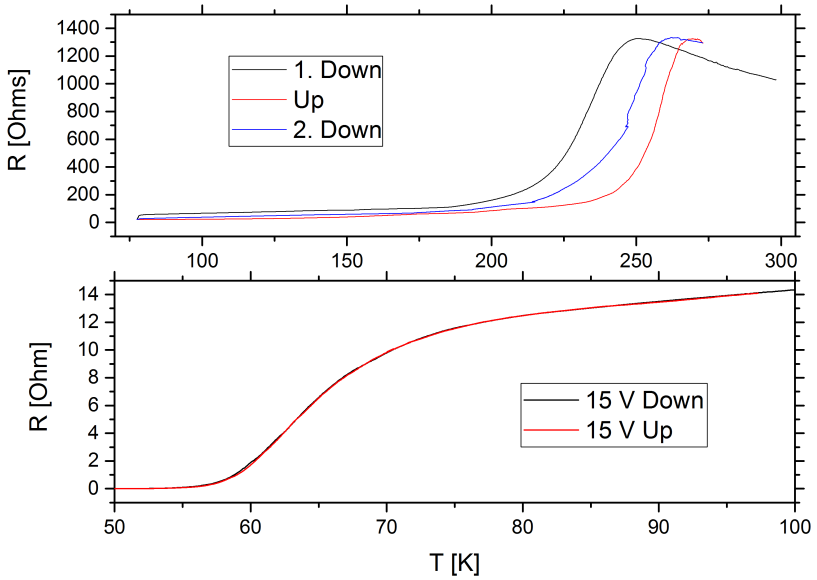

Figure 3.4: Shows the difference in hysteresis when measurements are obtained without (upper) and with insulating layers around the sample and sensor (lower).

When performing transport measurements with the Montgomery technique, a possible unwanted effect may be that not the entire potential drop over the sample is captured because the current may be biased to flow in the lower part of the sample, between the current contact points, as seen in figure 3.5.

To minimize this effect, samples have been investigated over a large range of applied voltages to ensure that similar results are yielded with regards to the shape of the obtained curves. As the applied voltage increases, more and more current is forced to flow in the upper part of the sample and thus giving a larger contribution to the measured potential drop.

To investigate the contribution of this possible effect, a Matlab script have been written and included in appendix D.1. Here the resistance over the whole sample is accounted for, by deploying Kirchoff's current and voltage laws, and by utilizing the potential measured over the constant resistance seen in the circuit diagram in figure 3.1.

During measurements, a fixed voltage is applied to the circuit. By assuming

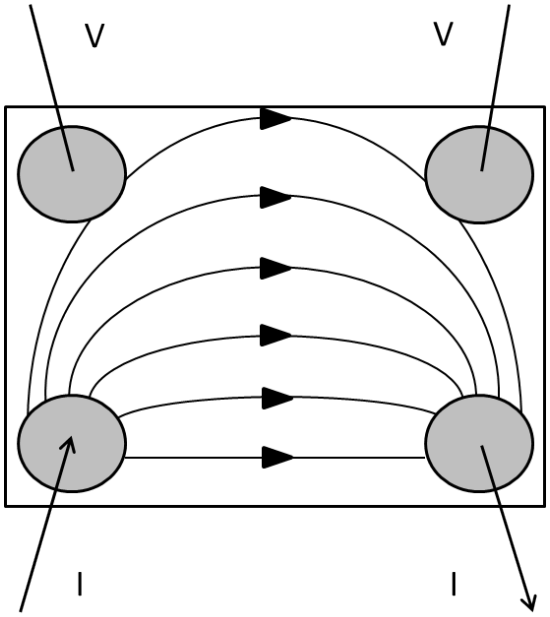

Figure 3.5: A schematic view of the possible current distribution in a plane of thin film. Contact pads are mounted in the corners of the sample, corresponding to the Montegomery four-corner technique.

no voltage drop in the wires, the whole potential drop must occur over the sample and the constant resistance according to Kirchoff's voltage law. Thus the whole idealized potential drop over the sample must be: $V_{Sample} = V_{Battery} - V_{Resistance}$.

As Ohm's law states that the resistance is found as the potential drop divided by the current and Kirchoff's current law states that current through the sample must be the same as the current through the constant resistance, the whole resistance of the sample must be:

$$R_{Sample} = \frac{V_{sample} * R_{Resistance}}{V_{Resistance}}$$

The script based on these equations have been applied to some of the result presented in this thesis and these are included in appendix C.

3.2 Magneto-Optical Imaging

Magneto-optical imaging (MOI) based on the Faraday effect is an excellent tool to visualize magnetic field distribution [33] and have been utilized in the experimental work performed in this thesis. This technique allows to investigate both magnetic and superconducting samples.

The Faraday effect is the rotation of the polarization vector of light as a magnetic field is applied along the axis of its propagation in a transparent medium [33]. A schematic view of the Faraday effect is shown in the left part of figure 3.6. Here one can see that this effect causes the polarization vector of the light to rotate as it travels through the Faraday-active crystal. It is this rotation that defines the contrast in a magneto-optical image. The magnitude of the contrast is linked with the Faraday rotation angle, θ_F, which depends on the material-dependent Verdet constant, V, the distance the light travels in the Faraday-active crystal, d, and the magnetic field component parallel to the axis of the propagation of light through this crystal, H [33] [34].

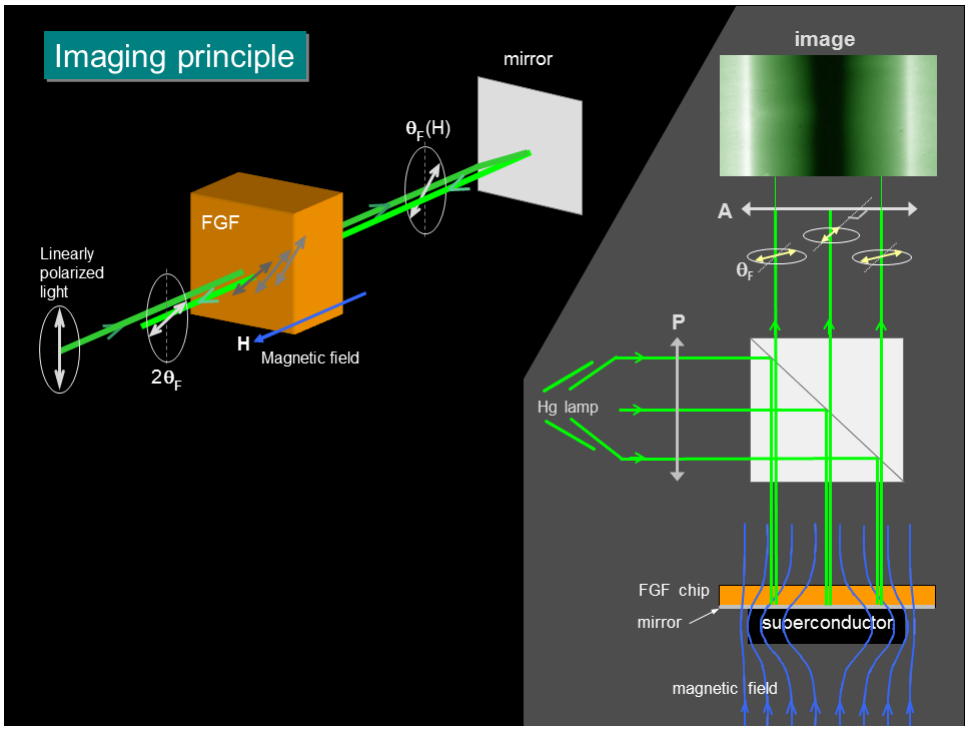

Figure 3.6: A schematic representation of the magneto-optical imaging technique. The Faraday effect is illustrated in the left part and the MOI setup is depicted to the right. This figure is provided by Prof. Tom Henning Johansen.

A schematic overview of the experimental setup utilized for magneto-optical imaging is shown in the right part of figure 3.6. A mercury lamp provides light, i.e. electro-magnetic radiation, that has a multitude of polarization components. The first polarization filter, denoted with P in the right part of figure 3.6, ensures that the light becomes linear polarized, meaning that only light with one specific spatial direction of eletric and magnetic field is let through the polarizer. The linear polarized light beam is then reflected by a beam splitter, shown in the right part of figure 3.6 as a white square, towards the Faraday active crystal that covers the sample subjected to magneto-optical (MO) investigation. The Faraday-active crystal is called a MO indicator film, and denoted with FGF (Ferrite Garnet Film) in figure 3.6. It is responsible for the contrast in the

MO image. To enhance the contrast and reflect the light beam towards the analyzer, a thin metallic film, a mirror, is deposited on the bottom of the MO indicator film. The contrast gets enhanced due to the fact that the light beam passes through the Faraday-active crystal twice as the light beam is reflected back through the MO indicator film, effectively doubling the magnitude of the Faraday rotation angle, θ_F. The light beam is then transmitted through the beam splitter and arrives at the analyzer denoted by A in the right part of figure 3.6, which generates the MO image.

On the right part of figure 3.6 one can see that light beams reflected from the outer edges of the sample experience a larger Faraday rotation than the light beams reflected from the center of the sample. This is due to the fact that the magnetic field component parallel to the propagation path is larger in the edges of the sample then in the central regions, where magnetic field is expelled from the superconductor.

When the polarizer and analyzer are directed perpendicular to each other, the dark area in a MO image corresponds to the region, where light did not undergo Faraday rotation and thus did not experience magnetic field along the axis of propagation. The illuminated area in a MO image contain light that has experienced magnetic field parallel to the axis of its propagation and thus undergone Faraday rotation. Here the contrast is increasing with the magnitude of the rotation.

The MO indicator films used in our experiments are composed of three layers: a substrate of gadolinium gallium garnet, a Bi-substituted ferrite garnet layer responsible for the Faraday rotation [31] [33] and a thin aluminium layer acting as the mirror.

The experimental equipment used in MOI imaging includes a Leica polarization microscope with a Qimaging EXi blue CCD camera mounted on its top. As our experiments require low temperatures, a Dewar liquid helium tank with a liquid helium transfer siphon is connected to an Oxford helium-flow cryostat surrounded by a magnetic coil connected to a Delta Elektronika SM 7020 power supply. The temperature is controlled by an Oxford ITC503 temperature controller, and the vacuum needed in the cryostat is provided by a Hi Cube Pfeiffer vacuum pump.

3.3 Scanning Electron Microscopy

The scanning electron microscopy (SEM) is a widely used and versatile technique to investigate the structure of solid object's surface, in particular its topology and element analysis, with a high resolution. Details that can not be resolved in an optical microscope can be seen in great detail with a SEM microscope. Resolution down to sub nanometer level have been reported [26].

A SEM uses a focused beam of electrons to scan the surface of the sample in a raster pattern to create an image and perform element analysis. The incident electrons interact with atoms inside the sample at various depths

resulting in different signals from the sample. These include signals from secondary electrons (SE), back-scattered electrons (BSE), characteristic x-rays and cathodoluminescence. The different signals result from different interactions in different areas inside the sample and are detected deploying specific sensors sensitive to them [50]. Figure 3.7 give details of emitted x-rays and electrons in SEM.

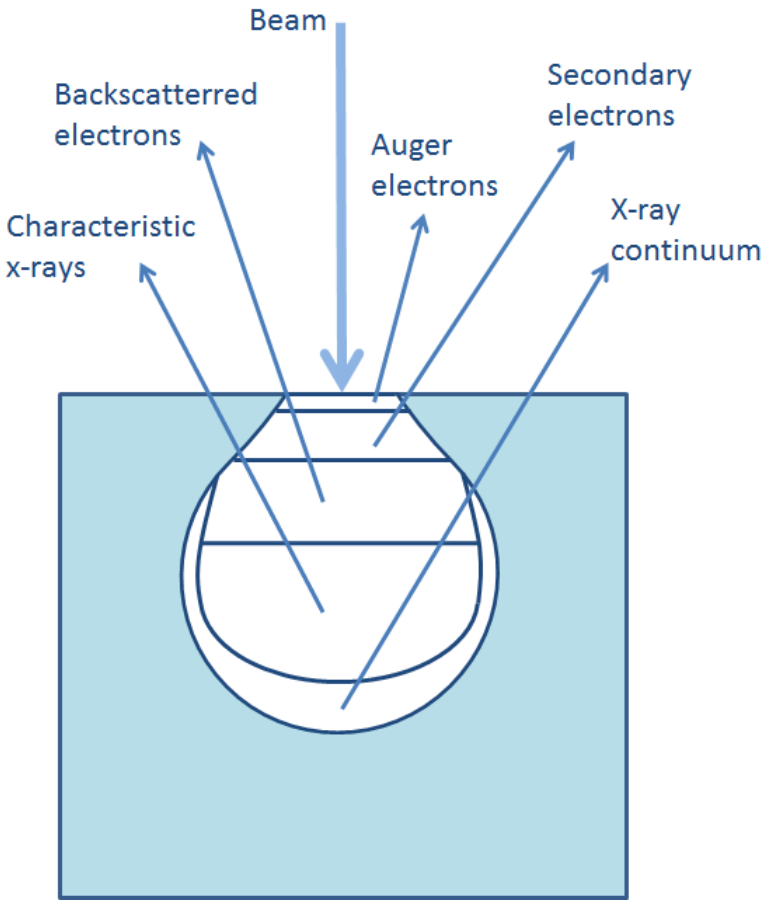

Figure 3.7: A schematic overview of different signals and areas from which they emerge during a SEM scan.

For the purpose of this thesis, the secondary electrons (SE) are of importance as they are generated near the surface and give information about the sample's topology and morphology. Since this signal comes from a small volume close to the surface, images can be generated with a high spatial resolution [50]. The secondary electrons are created by inelastic scattering events, in which incident or backscattered electron knocks out an electron from the outer shell of the atoms in the sample. If the knocked out electron reaches the sample surface and the secondary electron detector, Everhart-Thornley detector, it contributes to the SE image [40]. For SEM imaging, a FEI Quanta 200 FEG-ESEM and a Hitachi TM300 TableTop Microscope have been used.

3.3.1 Energy Dispersive Spectrometer

Energy dispersive spectrometer (EDS) has been used to determine the chemical composition of the samples under investigation and for this a Hitachi TM300 TableTop Microscope have been deployed. Within the EDS method, analysis is based on characteristic x-rays emitted from the sample. These are called characteristic because they are specific to different elements in the sample. By deploying a detector sensitive to these x-rays, element analysis of the sample can be a simple procedure. The characteristic x-rays are produced when an incident electron knocks out an inner shell electron from the sample's atom causing a high-energy electron from an outer shell to take its place and thereby release energy as a characteristic x-ray quantum.

3.4 Atomic Force Microscopy

Surface analysis of thin films have been also done with an atomic force microscope (AFM) to reveal sample's surface roughness. This scanning probe microscopy technique was invented by Binning, Quate and Geber in 1985 [17] and is based on the principle of measuring forces between a sharp tip set on a cantilever and the sample's surface. The forces can be attractive, repulsive, magnetic or electrostatic. The cantilever is placed close to the surface and moved in a raster pattern over a small area while the deflection of the cantilever is recorded. The deflection is measured using an optical laser, which reflects from a mirror on the top of the cantilever and hits a position-sensitive sensor, a photo-diode.

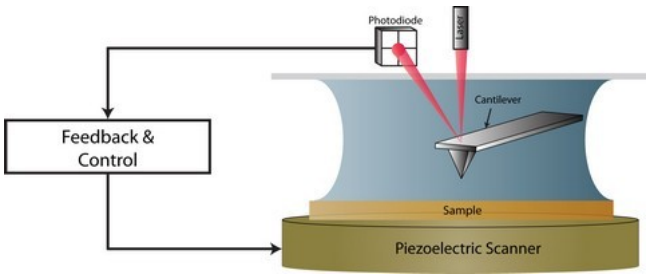

Figure 3.8: The schematic setup for atomic force microscopy. The figure is taken from [3].

The piezoelectric element has the ability to change its form when a voltage is applied and can thus be used to control or monitor the interactions between the tip of the cantilever and the sample surface. The change in piezo-voltage with displacement is usually very small, about 0.1nm/V, providing excellent spatial resolution in the z-direction.

The AFM is a versatile tool that can be used to measure forces, perform imaging and manipulations. In imaging mode, a three-dimensional mapping of the sample surface can be made based on the forces acting on the cantilever. This results in a high-resolution topographic image of the sample surface. The AFM can be operated in imaging with three different modes for the cantilever, namely contact, tapping and non-contact mode. Here we will focus on describing contact mode, as this is the mode used in the studies for this thesis.

In contact mode, the cantilever is, as the name suggests, in contact with sample surface as it scans across an area of the surface in the xy-plane while the height profile (z-direction) is recorded. The hight can be measured either by the deflection of the cantilever or by recording the feedback signal the piezoelectric component requires for the cantilever to be in contact with the surface. To avoid the tip of the cantilever from breaking into the surface of the sample due to the strong attractive forces that may be acting close to it, the cantilever is ensured to only barely touch the sample and therefore also avoids scratching it.

To measure the surface roughness we used Veeco diCaliber AFM known as a tabletop AFM due to its small size and relative ease of use. A picture of this AFM is shown in figure 3.9. The open-source software Gwyddion have been used to process the data from AFM measurements, and the results will be presented in the end of Chapter 4.

Figure 3.9: Figure shows the atomic force microscopy used in experiments.

3.5 X-ray Diffraction

Samples have been investigated with x-ray diffraction (XRD) to determine crystallinity and to study the phases present in them. For this purpose, a PanAlytical Empyrean diffractometer with a 4-bounce Barthels monocromator (asymmetrically cut GE(220)) as a primary optics and a PIXcel3D detector have been utilized and measurements have been performed in collaboration with the Chemistry Institute at the University of Oslo.

The information obtained from XRD measurements is based on the diffraction pattern created as a monochromatic incident x-ray beam interacts with the atoms in the target material and gets scattered. In crystalline structures, the scatted x-rays undergo constructive and destructive interference and a diffraction pattern is created at the detector. The diffraction pattern is based on Bragg's diffraction law and gives information about the structure of the material. By comparing the measured diffraction pattern with known diffraction patterns for basic materials, information about the crystalline phases present in the sample can be obtained.

3.6 Physical Property Measurement System

The physical property measurement system (PPMS) is a flexible and automated system from Quantum Design Ltd. that can be used to measure different material properties, like thermal, electrical transport properties and magnetic susceptibility, in a wide range of cryogenic temperatures and applied magnetic fields. For the purpose of this thesis, magnetization and susceptibility have been measured in a vibrating sample magnetometer of PPMS.

3.6.1 Vibrating Sample Magnetometry

A vibrating sample magnetometer (VMS) is designed to investigate magnetic properties. The technique is based on Faraday's law of induction, which states that a changing magnetic field will induce an electric field. By precisely measuring the induced field, magnetic properties can be resolved with great accuracy.

The sample is placed inside a chamber and subjected to a strong external uniform magnetic field set up by electromagnets surrounding the chamber. This causes the sample to be magnetized and by vibrating the sample up and down (in the z-direction as indicated in figure 3.10) a perturbation of the external field is created and measured by a set of pick-up coils inside the chamber, as indicated in figure 3.10. This is done by measuring the electro-motive force induced in the coils and this force will depend on four factors, namely the external field strength, the frequency and amplitude of the vibration, and the magnetization of the sample. As three of these factors are known in experimental setup and by precisely changing the temperature inside the chamber, magnetic moment as function of temperature can be obtained when a DC magnetic field is applied. By applying an AC external magnetic field, magnetic susceptibility as function of temperature can be measured in a similar manner.

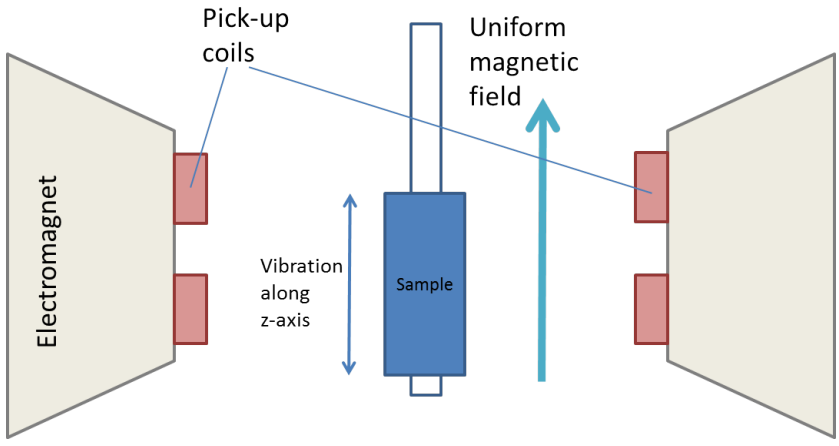

Figure 3.10: The figure shows the schematic setup for the VSM measurements.

3.7 Pulsed Laser Deposition

Pulsed laser deposition (PLD) is a physical vapor deposition technique that allows for epitaxial growth of thin films and offers an elegant alternative to molecular beam epitaxy (MBE). A schematic overview of the technique is sketched in figure 3.11. Here a high-power pulsed laser provides the energy needed to evaporate chemical compounds stored in targets inside a vacuum chamber. As the laser hits the target, a plasma plume forms and condenses on a suitable substrate mounted above the target. By repeatedly hitting the target with the laser, a desired amount of the chemical compound is deposited on the substrate. For deposition of multilayer thin films, the targets can easily be interchanged in-situ.

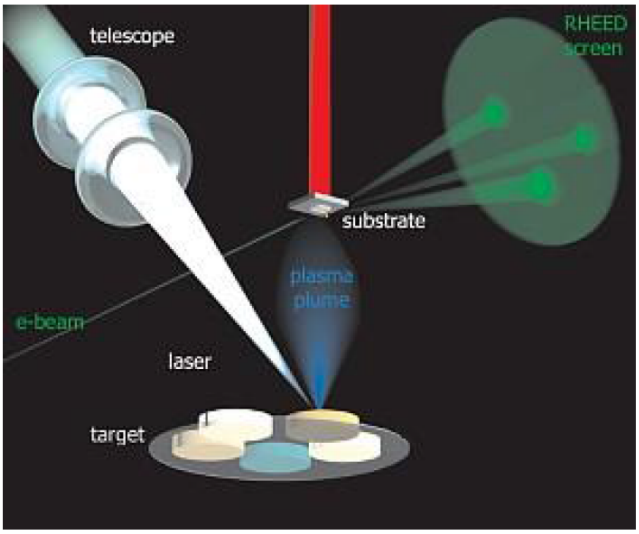

Figure 3.11: Schematic representation of pulsed laser deposition technique for epitaxial growth of high quality thin films. The figure is taken from [8] and modified.

The deposition can be performed in ultra high vacuum to avoid contamination by undesired elements or with background gases present, like oxygen, if deposition of, for example, fully oxygenated materials is the aim.

Reasons for PLDs superiority over MBE is the versatility of chemical compounds that can be deposited and the high speed of deposition. Another advantage is that since the targets are not electrically connected to anything, no care about conductivity needs to be taken, nor heat evacuation of the chamber is needed due to the relatively low average power applied by the pulses.

As a means to control the crystallinity of the deposited surface layer, a reflection high energy electron diffraction (RHEED) method is deployed in parallel with the deposition process [22]. A schematic overview of the RHEED setup is shown in figure 3.12. Here electrons are emitted by an electron gun and hit the sample surface at a shallow angle. The atoms at the sample surface diffract the incident

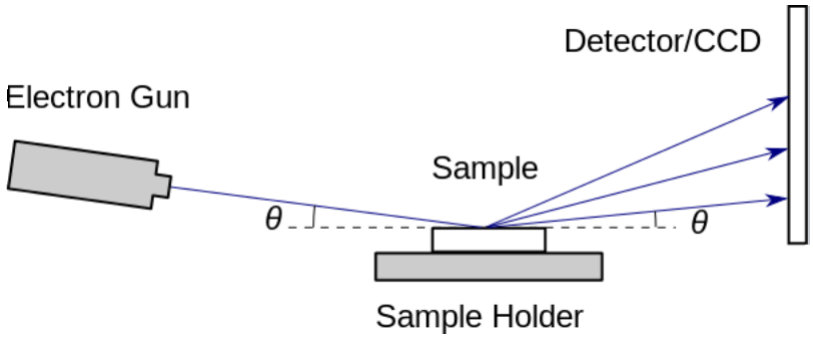

Figure 3.12: Schematic representation of reflection high energy electron diffraction method deployed during PLD to monitor surface crystallinity. The figure is taken from [6]

electrons, and, due to constructive interference, a diffraction pattern is formed at the detector, giving the operator information about the surface roughness.

The growth thickness of the layers can also be found by counting the number of laser pulses utilized provided careful calibration have been performed in advance. The average film growth per laser pulse will depend on multiple factors. These include the separation between the substrate and target, laser energy density and laser spot size. A deposition rate per laser pulse of about 1 Å is frequently reported [22].

3.8 The samples bibliography

This section is meant to give the reader a schematic overview of the main samples investigated in the work related to this thesis. Other samples have also been studied, but their results have been excluded from the results presented in Chapter 4 and will therefore not be presented and described here.

The samples have various origin, but a common factor is that they all are grown with PLD and to a great extent have similar chemical composition. Mainly thin film samples composed of thin layers of the superconducting material $YBa_2Cu_3O_{7-\delta}$ (YBCO) and the colossal magnetoresistive material $La_{2/3}Ca_{1/3}MnO_3$ (LCMO) grown on a substrate of $SrTiO_3$ (STO) have been investigated. These materials have very similar crystal lattice parameters, both having perovskite structure, allowing for successful epitaxial growth of layered structures.

LCMO is a perovskite manganite with a structure $RE_{1-x}AE_xMnO_3$, where RE is La and AE is Ca, exhibiting colossal magnetoresistive behaviour [70]. Throughout this thesis we will see some variations of this manganese perovskite material.

3.8.1 FMS439-PHYS471

This bilayer thin film of $La_{2/3}Ca_{1/3}MnO_3$ (LCMO) and $YBa_2Cu_3O_{7-\delta}$ (YBCO) have been c-oriented grown ex-situ on a STO substrate with the PLD epitaxial technique. For growth with this technique, the typical requirement is to deposit both layers of thin film without removing the sample from the chamber, but here ex-situ indicates that the thin film was removed after the first layer was deposited to perform testing before the sample was returned to the chamber and the top layer was deposited. This may have introduced surface contaminations from the exposure to atmosphere between the two subsequent depositions which can lead to interesting interface effects.

The FMS439-PHYS471 sample was produced in the Physics department at the University of Birmingham and brought to the superconductivity laboratory at the University of Oslo by my supervisor, Pavlo Mikheenko. The sample is square in shape. A schematic view of the sample is presented in figure 3.13. This sample has been investigated by transport measurements, MOI, SEM, EDS, XRD and various PPMS techniques. These investigations resulted in a published article that is included in appendix E.

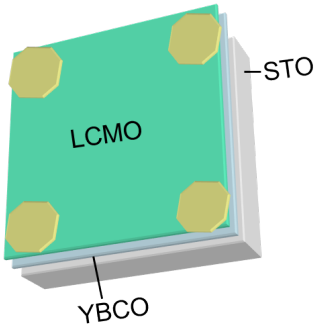

Figure 3.13: A schematic representation of the sample FMS439-PHYS471.

For this sample, there is some uncertainty about how thick the two layer of thin films are. A lot of work have been done trying to find this experimentally, but due to the unconventional ex-situ growth of this sample and the resulting interface layer, no convincing exact data have been obtained. An individual thickness of 200 nm is a good estimation for the two layers.

3.8.2 PHYS63

The sample PHYS63 is a bilayer consisting of $La_{1-x}Sr_xMnO_3$ (LSMO) and YBCO grown in-situ with PLD on a STO substrate. The top layer is YBCO and both layers have a thickness of 200 nm. A schematic view of the sample is presented in 3.14. This sample was also produced in the Physics department at the University of Birmingham. Both transport measurements and MOI have been performed on this sample.

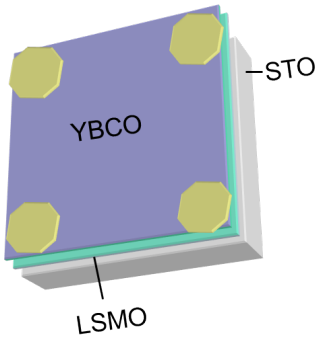

Figure 3.14: A schematic representation of the sandwich structure of sample Phys63.

3.8.3 LCMO100nm-YBCO200nm and YBCO200nm-LCMO100nm

Two other bilayer thin films have been grown in-situ with PLD on a substrate of STO and both are rectangular in shape. A schematic view of these two samples is shown in figure 3.15.

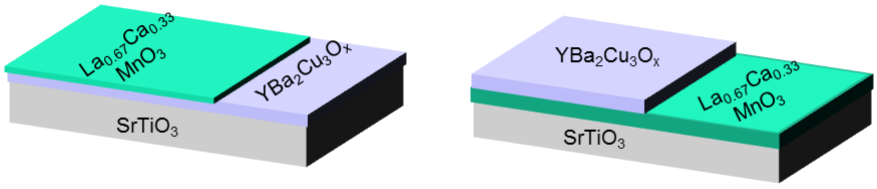

Figure 3.15: The figure shows a schematic representation of samples LCMO100nm-YBCO200nm (left) and YBCO200nm-LCMO100nm (right).

For LCMO100nm-YBCO200nm, a 200 nm thick layer of YBCO was first deposited before a layer of LCMO of the thickness of 100 nm was deposited to cover 2/3 of the sample surface. For YBCO200nm-LCMO100nm a 100-nm layer of LCMO was first deposited before a 200-nm YBCO layer was grown to cover half of the sample surface. This results in areas of different chemical composition exposed at both of the sample surfaces allowing for multiple configurations of transport measurements to be performed. This gave us a possibility to extract exciting transport property results in a new way for these bilayer structures.

Both samples have been investigated with MOI to determine their magnetic and superconducting properties, and EDS was performed to accurately verify their chemical composition and position of the layers.

CHAPTER 4

Results and Discussion

In this chapter, the experimental results will be presented. First, the sample FMS439-PHYS471 will be introduced. This sample and the novel phenomena it displayed formed the motivation for the further experimental work performed in this thesis as this was the main sample under investigation when joining the research group. Not all results for this sample were obtained as part of this project and these will be clearly marked thereafter. The experimental work accumulated to a published conference article, included is appendix E.1, where I, the author of this thesis, have taken part in both writing, proposing ideas and analysing transport measurement results. As the results are somewhat inconclusive for this sample, investigations of similar systems have been undertaken and form the foundation for the experimental work performed in this thesis.

As work progressed, it became clear that the focus in this thesis would be on the competing order parameters that exist in superconductors and ferromagnetic materials, and the effects of spin injection.

First, a section about spin injection into the normal state of a superconductor will be presented for sample YBCO200nm-LCMO100nm, where a clear anomaly emerges as the injection comes into play. As spin injection into the normal state of a superconductor is an area of research that eludes to be found in published works, the results obtained within this section are both surprising and innovative.

Then, spin injection into the superconducting state is investigated and presented for the samples YBCO200nm-LCMO100nm, LCMO100nm-YBCO200nm and PHYS63. Before, a review of the experimental results for the sample FMS439-PHYS471 is given in the light of the newly obtained results.

4.1 Review of the experimental results for sample FMS439-PHYS471

As the first sample investigated and largely the motivation for this thesis, the bilayer thin film of YBCO and LCMO grown ex-situ on a STO substrate show novel experimental results that, to a large extent, have been investigated in the attempt to clarify their origin. A schematic view of the sample is presented in figure 4.1.

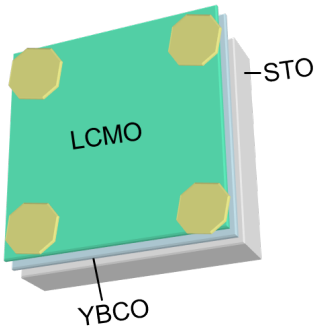

Figure 4.1: Schematic representation of the sample FMS439-PHYS471, an ex-situ grown bilayer thin film of YBCO and LCMO. For more information about the sample the reader is referred to section 3.8.

In transport measurements of the temperature dependence of resistance R(T), seen in figure 4.2, three unconventional features emerge. First, no evidence of the expected magnetic transition in LCMO from paramagnetic to ferromagnetic phase at the Curie temperature, T_{Curie}, of about 250 K is seen. The typical evidence of this magnetic transition is usually seen in temperature dependence of resistance as an increase in the resistance above T_{Curie} as the temperature is lowered from room-temperature towards 250 K, and drastic decrease in resistance as the temperature is lowered further. This is not what one sees in figure 4.2. Instead, one can see an increase in the resistance all the way towards the superconducting transition, which is the second unexpected feature. Usually, due to the presence of superconducting film, the resistance decreases in a quasi-linear manner as the temperature is lowered towards the critical temperature, T_c, marking the onset of the superconducting transition. The third and most surprising feature seen in figure 4.2 is a sharp increase in the resistance, emerging below the superconducting transition.

The latter resistance anomaly seems to have some dependence on the voltage applied, i.e. the value of the probing current, with regards to both the height and width of the resistive peak. This relationship is better resolved in the inset in figure 4.2.

The relatively large difference in the critical temperature, T_c, observed for different measuring currents might be explained, in addition to the important effect of the decrease of T_c with current, by the speed, at which measurements were done, and the fact that the sample and thermometer are not in direct

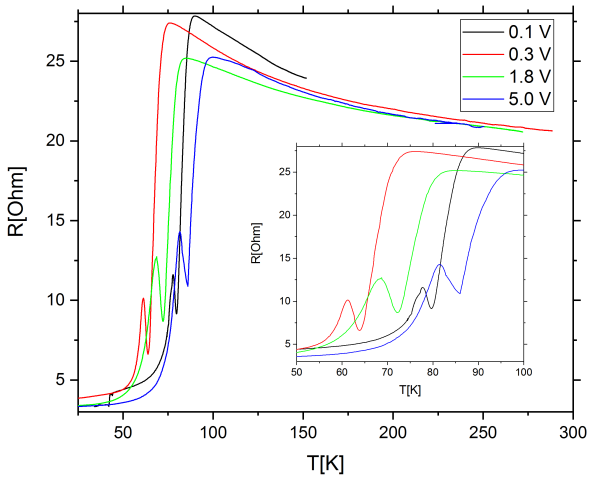

Figure 4.2: In-plane transport measurements for the bilayer sandwich structure of LCMO on top of YBCO, grown on STO. The inset is meant to resolve the relationship between the measuring current and the resistive state emerging below the superconducting transition.

thermal contact as the sample is subjected to some Joule heating during the experiments. Typical evidence of these effects is seen as some hysteresis between measurements obtained while cooling and heating the sample, which is presented in figures 2 and 3 in the article attached in appendix E.1 and found in ref. [24].

As evident from the transport measurements shown in figure 4.2, below the superconducting transition the resistance stays at a finite level, i.e. not reaching zero. This is to be expected as contacts are mounted to the LCMO top layer, a material that will contribute to the overall resistance with a finite value over the whole temperature range.

Investigation of the superconducting properties of the YBCO layer by MOI appeared to be difficult, as a result of the magnetic properties of the LCMO top layer mainly contributing to the obtained MO-image. Differential imaging yielded the result shown in figure 4.3, where a stripy structure emerged. This suggests a magnetic domain structure of LCMO with regions of alternating spin orientation.

Transport measurements both perpendicular and parallel to this structure were performed. The measurements shown in figure 4.2 are obtained when current was injected parallel to the stripy structure. As transport measurements were repeated with current injection perpendicular to the stripy feature, large in-plane anisotropy was revealed.

Resistance as function of temperature for the two configurations of current injection is compared in figure 4.4, where the large anisotropy clearly can be

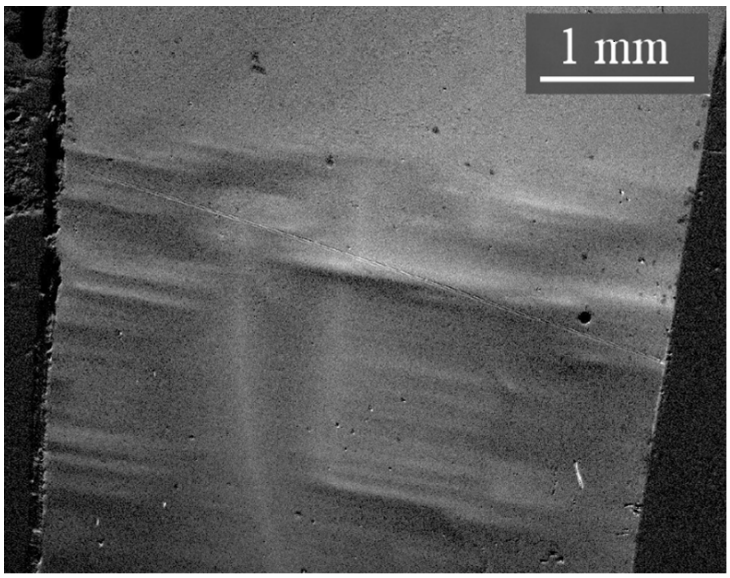

Figure 4.3: Differential MOI image of the sample obtained at 3.8 K when a magnet was rotated outside the sample chamber. Picture is taken and processed by Pavlo Mikheenko and Hans Mollatt. The lighter and darker areas suggest the presence of domains in LCMO of alternating spin orientation.

seen. The resistance is about two orders of magnitude larger when current is injected perpendicular, as compared to parallel to the stripy feature. Also, no enhanced resistance below the superconducting transition is present for perpendicular current injection. Common for the two measurements is the increase in resistance as the sample is cooled towards the superconducting transition and the absence of the signature of the magnetic transition at the expected T_{Curie} of about 250 K.

As no clear evidence of T_{Curie} is found in the transport measurements and to further explore the stripy domain structure of LCMO, the sample was investigated with PPMS and vibrating sample magnetometry in collaboration with the Chemistry department at the University of Oslo and Asbjørn Fjellvåg. The result is shown in figure 4.5, where the sample is measured while cooling (green) and heating (blue) in a DC magnetic field of 1 T. The curve with red dots is obtained when the sample is heated in a filed of 1 T after cooling with no applied magnetic field.

From figure 4.5, one can see that the sample's response is as expected for a common colossal magnetoresistive material. The large green arrow indicates the location of the Curie temperature and the spin polarization is established below this point. In the temperature interval from 50 to 70 K, a large peak in the magnetic response is observed for measurements performed while heating the sample. Its absence in measurement performed while cooling the sample indicates that if the peak is a result of a magnetic phase, the phase needs low temperatures and perhaps time to be established. The increase in magnetic

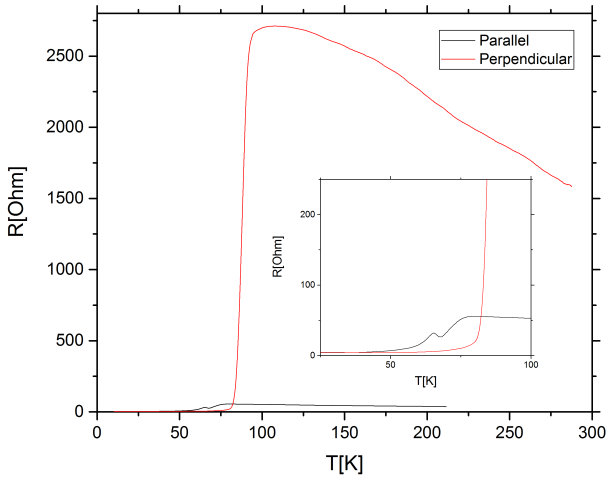

Figure 4.4: Temperature dependence of resistance for current injection parallel (black) and perpendicular (red) to the stripy feature seen in figure 4.3. Both measurements were obtained when a voltage of 0.3 V was applied to the circuit. Inset zooms in to resolve parallel current injection.

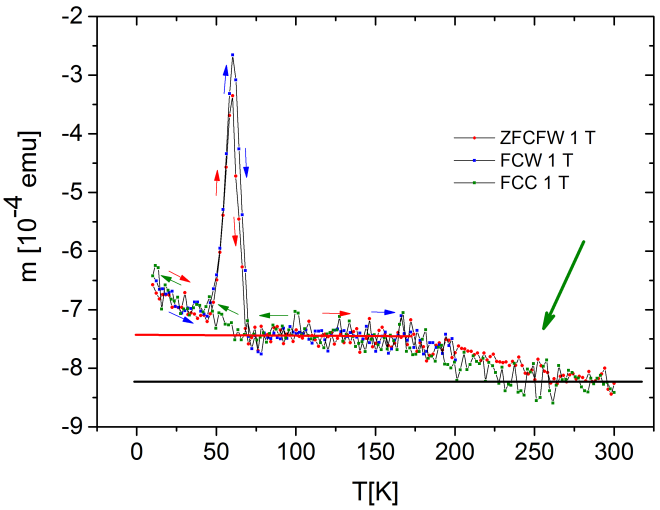

Figure 4.5: Magnetic response obtained with vibrating sample magnetometry when a 1 T DC magnetic field was applied. ZFCFW marks the response when sample is cooled with no applied field and then heated in a field of 1 T. FC denotes that the sample is cooled in a magnetic field, where FCC is response obtained while cooling and FCW when heating the sample. The large green arrow points at a magnetic transition taking place at the Curie temperature.

response with decreasing temperature is seen below 70 K and can be attributed to another ferromagnetic transition.

To further investigate the possibility that the large peak in magnetic response seen between 50 and 70 K is due to a magnetic phase, X-ray diffraction was performed in collaboration with the Chemistry department at the University of Oslo and Asbjørn Fjellvåg and Øystein Fjellvåg. The resulting XRD pattern is shown in figure 4.6, where the inset is intended to resolve the peak observed in the interval from about 110 to 120 degrees. The large peak corresponds to the signal from the STO substrate. On the right-hand side of this peak, the signal from LCMO and or YBCO can be seen. In addition, two unknown phases with low intensity emerge at 30 and 45 degrees giving indication of inter-diffusion at the interface between YBCO and LCMO. This inter-diffusion is likely to result in a layer close to the interface having properties that are not intrinsic to the pure compounds. It is thus possible that the magnetic phase thought to be responsible for the large peak in the magnetic measurement between 50 and 70 K is located at the interface layer. As the sample was grown ex-situ, meaning that it was removed from the chamber for testing between deposition of YBCO and LCMO, some contamination of the interface may have been introduced by the exposure to atmosphere.

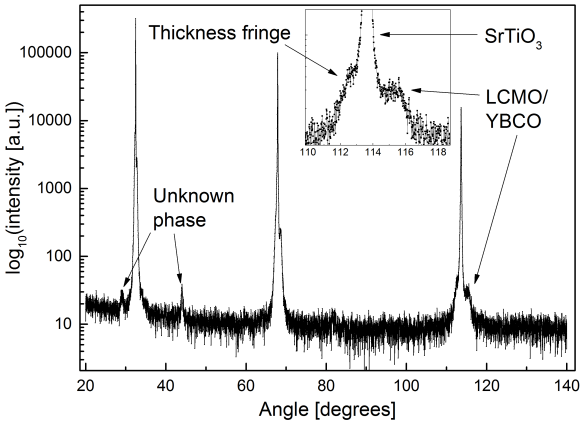

Figure 4.6: X-ray diffraction pattern obtained for the sample FMS439-PHYS471 by Asbjørn and Øystein Fjellvåg.

The experimental results for this ex-situ bilayer thin film are somewhat contradicting. On one hand, no evidence of the magnetic transition at T_{Curie} is seen in transport measurements at zero magnetic field around 250 K, while indication that T_{Curie} is located at its expected value is found in the magnetic measurements.

As shown in earlier experimental works like [53] performed on similar colossal magnetoresistive materials, the Curie temperature moves to higher temperatures as large external magnetic fields are applied. Thus, the possibility that the large

magnetic field applied during the magnetic measurements may have moved T_{Curie} from a lower temperature to the expected 250 K cannot be excluded.

Based on the transport measurements alone, it is tempting to propose that the Curie temperature have moved to a much lower temperature, which is known to occur due to oxygen deficiency [28] [51] [55], and resides close to the superconducting transition when no external magnetic field is applied. Thus, the onset of spin injection could be responsible for the resistive state seen in transport measurements when current is injected parallel to the stripy feature seen in MOI. This suggestion is supported by the increasing resistance seen when we move from higher temperatures towards T_c, but fails to find support by the fact that the enhanced resistive state is absent for transport measurements performed with perpendicular current injection.

The magnetic peak seen in figure 4.5 coincides well with the temperature interval, in which the resistive state is seen below the superconducting transition in measurements of the temperature dependence of resistance with current injection parallel to the stripy features observed in MOI. This leads to the conclusion that the two features are correlated, but as the magnetic peak only appears for measurements performed while heating the sample and the resistive state is found both while heating and cooling the sample in transport measurement, a conclusive correlation between them cannot be drawn.

As no satisfactory explanation for the intriguing and novel features seen for this bilayer sandwich structure was found, further investigation of similar thin films have been performed and form both the motivation and background for the experimental work performed in this theses.

4.2 Effect of spin injection into the normal state of a superconductor

The sample YBCO200nm-LCMO100nm is a bilayer thin-film structure epitaxially grown with PLD on a substrate of STO, where one layer of 100-nm thick LCMO was deposited first to cover the whole substrate, before a 200-nm thick YBCO layer was deposited to cover one half of the LCMO surface. For more information on the sample, the reader is referred to section 3.8.

To allow the sample to be measured in a multitude of configurations, four and three indium contacts have been attached to the bottom and top sides of the sample, respectively, as shown in figure 4.7. To investigate the effect of polarized spin injection we suggest a simple, but very effective approach. It is linked to two important measurement configurations. In both, the potential is measured over YBCO only, while current pads are either one on YBCO and another on LCMO or both are on YBCO injecting current through the whole sample and through the YBCO top layer, respectively. In the latter configuration, the current is only weakly allowed to overflow into the LCMO layer situated underneath YBCO, while in the prior configuration the current must flow through both YBCO and LCMO, which is the case of spin injection.

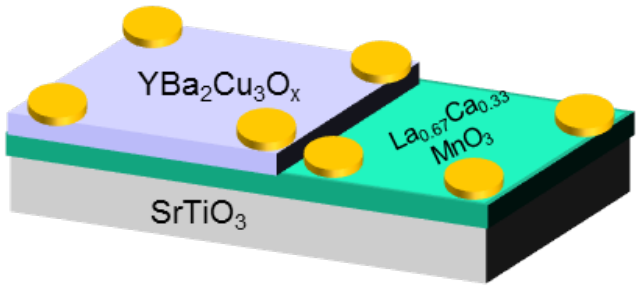

Figure 4.7: Schematic presentation of the sample YBCO200nm-LCMO100nm with seven contact pads mounted on the sample surface to allow for measuring over a wide range of configurations.

To investigate the effects of spin-polarized quasiparticle injection, it is of importance to insure that LCMO have T_{Curie} located at the expected temperature of 250 K for $La_{0.67}Ca_{0.33}MnO_3$, as seen from the phase-diagram in figure 2.7. EDX results obtained from the side of the thin film with exposed LCMO, included in appendix B.2, confirm the above mentioned chemical composition.

Transport measurements with four contacts at the corners of the sample giving spin injection measurement over the whole sample were performed to verify the value of T_{Curie}. The results shown in figure 4.8 indeed validate that T_{Curie} is in the vicinity of 250 K as evidenced by both the resistance and current measurements. Here one can see that the measured resistance changes from exponentially increasing in value to sharply decreasing over an interval of about 10 K (from 250 to 240 K), which is typical for the transition from paramagnetic to ferromagnetic ordering found at T_{Curie} for this material.

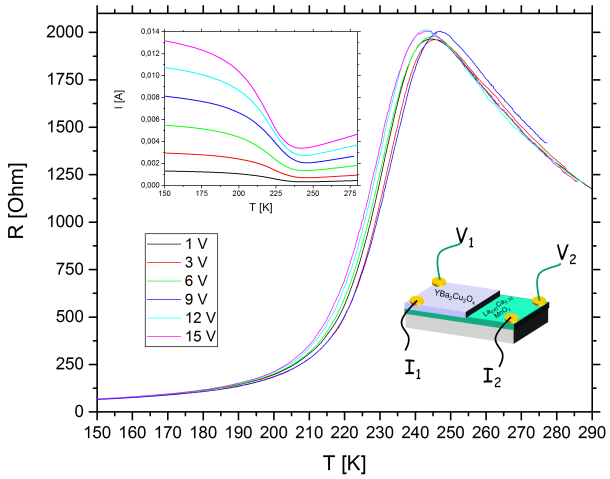

Figure 4.8: Resistance versus temperature R(T) transport measurements performed with applied voltages in the range from 1 to 15 V when both current and potential leads are mounted in the corners of the whole sample (see lower inset). The upper inset shows the corresponding measuring currents as function of temperature.

We can thus move forward assuming fully spin polarized current injection from the half-metallic LCMO below a temperature of about 250 K. The level of spin polarization could, however not be 100 %. For example, experimental evidence of spin polarization of about 80 % was reported in [57].

Figure 4.9 shows the results obtained from transport measurements when potential is measured over and current is injected into YBCO for the temperature interval from 50 to 300 K. If only the YBCO where to be measured, one would expect the resistance to decrease towards the superconducting transition in an approximately linear manner, but as the layer of YBCO is epitaxially grown on the top of LCMO layer, one might expect that the resistance should deviate from the linear behaviour by increasing the rate of decrease below 240 K. This should happen because the resistance in the LCMO layer shows rapid decrease at this point, as seen in figure 4.8, and with this measurement configuration the two layers can be seen as two resistors in parallel. Thus, an overall decrease in resistance is to be expected.

From figure 4.9 and 4.10 it is clear that the expected decrease in resistance is not seen. Instead, one can see an increase. This can be explained as an effect of spin polarized quasiparticles coming from the LCMO layer and creating a resistive interface between the two layers increasing the overall resistance of the sample. For a superconductor in its normal state, an equal number of spin up and spin down electrons is assumed on the Fermi level, whereas in the half-metallic LCMO, only conducting electrons with one spin orientation are present.

The conducting electrons crossing the interface are thus likely to experience an increase in the resistance at the interface since only about half of them are allowed to freely cross it due to restricted amount of available states for them at the Fermi surface. The other part must either flip spin to cross or avoid crossing the interface.

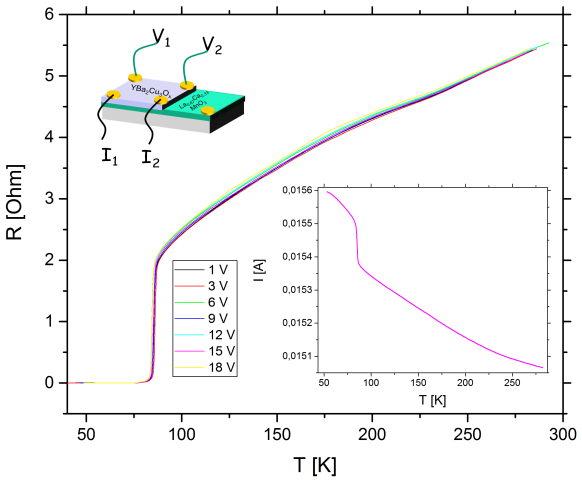

Figure 4.9: Resistance as function of temperature for the YBCO200nm-LCMO100nm sample at applied voltages ranging from 1 to 18 V when both potential and current leads are mounted on YBCO only. The inset shows the corresponding temperature dependence of current for the curve recorded at 15 V.

To further investigate the effect of spin injection into the normal state of the superconductor, transport measurements were performed with current injection through the whole sample while potential was measured over YBCO for a range of voltages applied to the circuit. The results are shown in figure 4.11 and 4.12. Again an increase in resistance is seen around 240 K, contradicting to what one would expect as the result of the sharp decrease in LCMO's resistance seen in figure 4.8.

If the anomaly at about 240-250 K observed in both configurations is to be explained by polarized spin injection, a confirming observation would be to find that higher applied voltages result in larger anomaly. As higher voltages correspond to larger currents, a larger effect of polarized spin injection would be expected. In both figure 4.10 and 4.12, one can see that indeed the highest voltage corresponds to the largest resistance, but so does the lowest one in the figure 4.12. So this result is somewhat inconclusive.

Comparing the resistance for the two measurement configurations, one can see that the overall resistance is larger in the case when current flows through the whole sample. This could be expected as the two layers of YBCO and LCMO can be seen as two resistors in series in the latter configuration as compared to

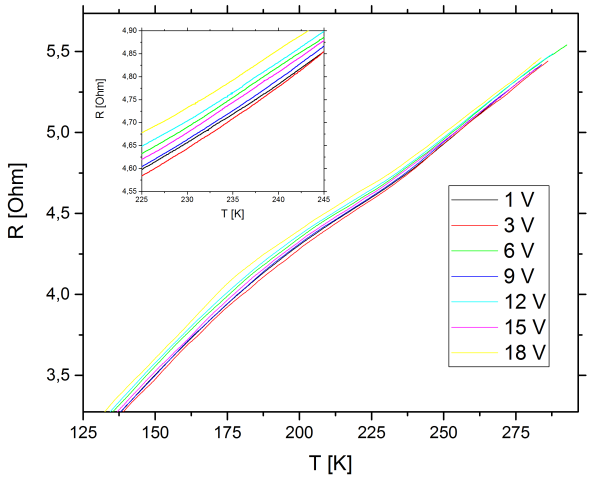

Figure 4.10: Temperature dependence of resistance from figure 4.9 zoomed-in on the temperature interval close to the magnetic transition. The inset is further zoomed-in to see the difference in resistance at different applied voltages.

in parallel in the prior, which results in different pattern of current flow close to the potential leads.

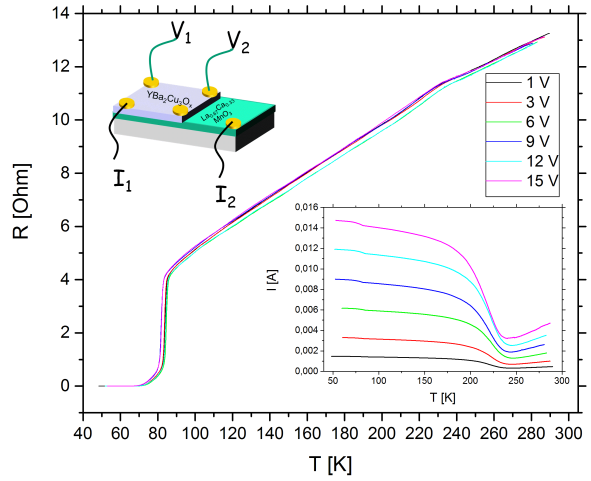

Figure 4.11: Transport measurements of resistance dependence on temperature performed with current leads mounted in the corners of the whole sample and potential leads mounted on the corners of the YBCO top layer. The inset shows the currents flowing through the sample at different applied voltages.

It is of interest to compare the shape of the resistance measured for the two

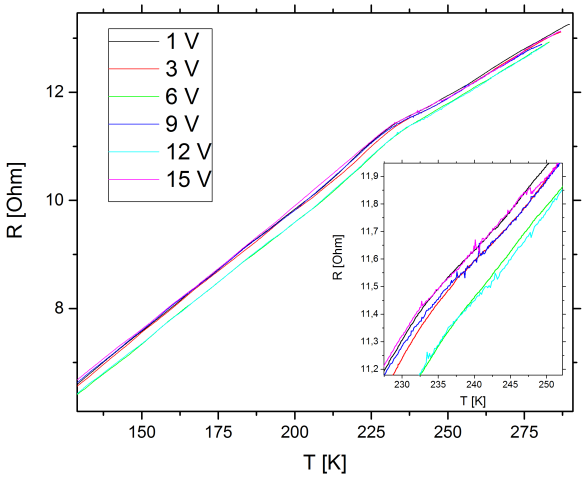

Figure 4.12: R(T) plot from figure 4.11, zoomed-in on the region of interest. To resolve the difference between the curves recorded at different applied voltages, a further in-zoom is displayed in the insert.

configurations described above. From figure 4.9, one can see that for the measurements performed with contacts mounted only on the YBCO layer, the anomaly persists over a wide temperature range, from about 240 K down to the onset of the superconducting transition. This is in contrast to the observed anomaly when current is injected through the whole sample, figure 4.11, where a much sharper cusp is observed in the resistance measurements around 240 K.

One way to better visualize the anomaly is by normalizing the resistance for the two configurations, as it is shown in figure 4.13. Here one can see that the shapes of the resistance curves are indeed different for the two configurations. To further investigate the difference in shapes, a straight line has been subtracted from the curves and shown in the temperature interval between 90 and 290 K in figure 4.14.

From both figure 4.13 and 4.14 one can see significant difference in the shapes of the curves. As potential is measured over YBCO in both configurations, but the current is injected to LCMO, a sharp anomaly around 240 K is observed, and a wide anomaly is observed when current is injected through YBCO. In the latter configuration, the current only partially overflows into LCMO and back again effectively crossing the interface twice. Here the conducting electrons both leaving and entering YBCO can be assumed to have the same spin state. For the prior configuration, the current must flow through the LCMO layer crossing the interface between YBCO and LCMO forcefully, but only once. One can assume that the reason for the difference in the shape of the anomaly likely resides in this specific flow.

At the time of writing, to our knowledge, no scientific publications on the

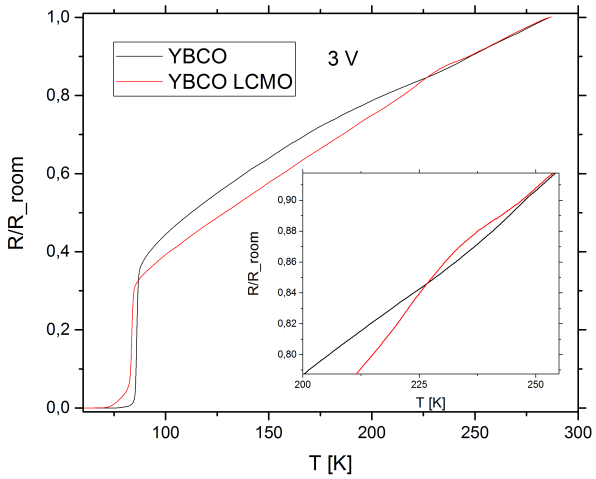

Figure 4.13: Temperature dependence of normalized resistance for the configurations where current is altered between injection into YBCO (black) and the whole sample (red), while potential is measured over YBCO. Both curves are for applied voltage of 3 V.

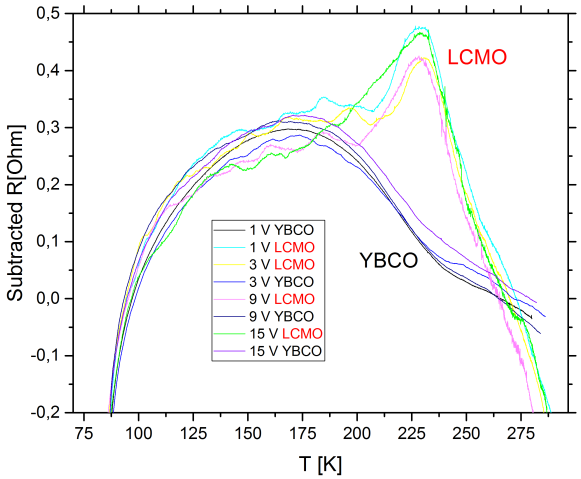

Figure 4.14: A modified temperature dependence of resistance with a straight line subtracted from the R(T) curves and shown in the temperature interval between 90 and 290 K for the two measurement configurations, where current is injected into YBCO (black) and LCMO (red), while potential is measured over YBCO.

topic of spin injection into the normal state of a superconductor were available

making the experimental work both innovative and of significance. As polarized spin injection into the normal state of a superconductor is an unexplored area, a complete understanding of how this phenomenon affects the shape of the anomaly requires more detailed research that will be left to future researchers or students.

4.3 Effect of spin injection on the superconducting transition

Polarized spin injection into the superconducting state have been an area of research the last three decades. In the earlier decades, investigation of competing order parameters existing in superconducting and ferromagnetic materials was mainly considering the ferromagnetic exchange field tendency to suppress the superconducting ordering. In the last decade, the field of research have undergone a renaissance, as a wealth of novel phenomena have been found linked to the area close to the interface between the two materials when they are epitaxially grown on each other. Such thin-film structures lead to new possible applications, especially in the emerging field of superconducting spintronics [38].

The following sections will describe experimental investigation of spin injection into the superconducting state for three similar samples, each contained within its own section, YBCO200nm LCMO100nm, LCMO100nm YBCO200nm and PHYS63. At the end, the experimental results obtained for the sample FMS439-PHYS471 will be revisited in light of the results obtained within the three following sections.

4.3.0.1 YBCO200nm-LCMO100nm

The effects of spin injection into the superconducting state of YBCO have been investigated in sample YBCO200nm-LCMO100nm. This sample is a bilayer structure grown on a substrate of STO. First, a layer of 100-nm thick LCMO was deposited, then half of the LCMOs surface was covered by a 200-nm thick YBCO layer. To allow the sample to be measured in a multitude of configurations, seven contacts pads have been mounted as shown in figure 4.15. It is worth mentioning that this is the same sample as investigated in previous section 4.2.

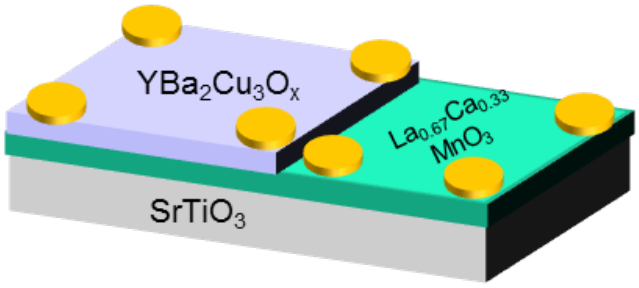

Figure 4.15: Schematic view on how seven contact pads are mounted on the surface of sample YBCO200nm-LCMO100nm to allow for measuring over a wide range of configurations.

To investigate the effect of polarized spin injection, determining the superconducting properties of the YBCO top layer, as well as the half-metallic properties of the LCMO layer is of importance. The latter have been performed and presented in the previous section 4.2 and shown in figure 4.8.

For the right part of the sample, EDX confirmed the half metallic composition of $La_{0.67}Ca_{0.33}MnO_3$. Also, at the expected Curie temperature of about 250 K, the magnetic phase transition is clearly visible in measurements of the temperature dependence of resistance, as shown in figure 4.8, for configuration where both potential and current are connected to the corners of the whole sample.

The superconducting properties of the YBCO layer have been investigated with MOI, and one of the resulting images is shown in figure 4.16. Here one can see that the superconductivity is strong, but the superconducting YBCO layer is by no means perfect, as flux is allowed to penetrate the interior in a non-uniform manner.

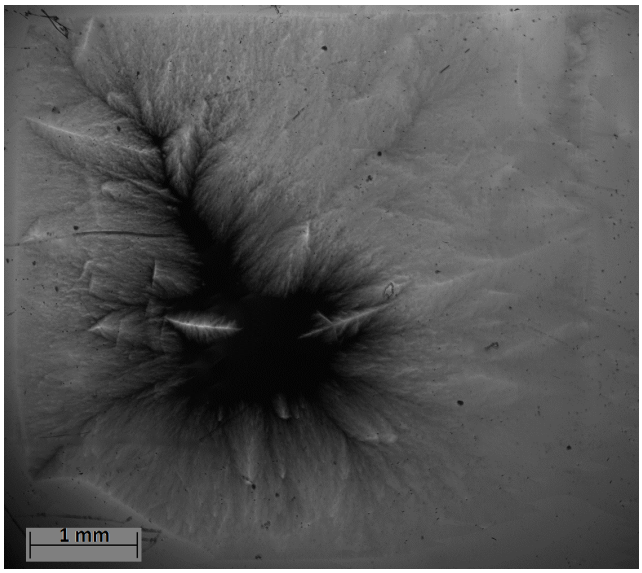

Figure 4.16: MOI image obtained when the sample is cooled to 3.7 K with no externally applied magnetic field, before the magnetic field is increased to 15.0 mT and flux penetrates the superconductor in a non-uniform manner, as seen by the lighter areas inside the sample.

A good indication of the presence of superconductivity in this thin film is also seen in figure 4.17. Here one can clearly see the superconducting transition and that the resistance drops to zero at lower temperatures when both current is injected and potential measured over the YBCO top layer. In this configuration, the layers of YBCO and LCMO can be seen as resistors in parallel, where the current is allowed to partially overflow into the LCMO layer.

Figure 4.18 shows the transport measurements for a range of voltages when current is injected and potential measured over the whole sample, i.e. the leads are mounted to the contact pads in the corners of the whole sample. These are the same measurements as presented in figure 4.8, but here a zoom-in have been made to resolve the superconducting transition.

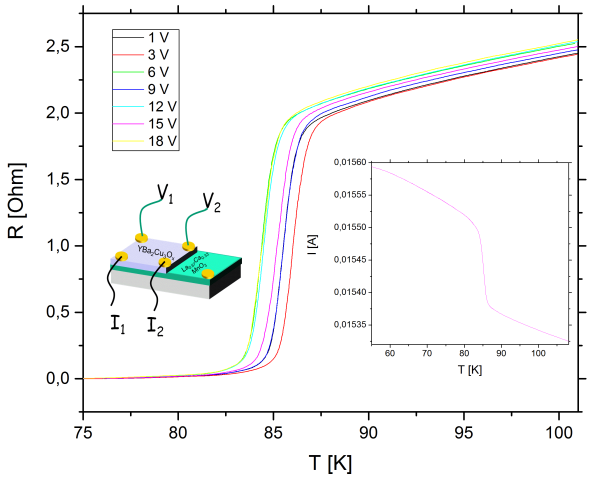

Figure 4.17: Temperature dependence of resistance around the superconducting transition when both current and potential leads are mounted on the YBCO layer only. Inset shows the corresponding measuring current for applied voltage of 15 V.

In figure 4.18, a wide superconducting transition emerges spanning over a large temperature interval, and one can see that the resistance does not reach zero for lower temperatures. The latter observation is an expected feature, since in this configuration there will always be a finite contribution to the measured resistance from LCMO over the entire temperature range.

In the configuration described above, the two layers of YBCO and LCMO can be treated as two resistors in series, and the current have to flow over the interface once. Thus, a forceful spin injection may be responsible for the wide superconducting transition.

Spin lifetime was shown experimentally to be many orders of magnitudes longer in a superconductor compared to in a ferromagnet [38] [66] [69] [48], especially when the energy of the injected particle, at the Fermi surface, is close to the energy of the superconducting gap. This leads to charge-spin separation [65] [49] and lower velocities, increasing the time between subsequent scattering events and thus increasing the spin lifetime [38] in the superconductor. The half-metallic nature of LCMO is known to be responsible for suppressing both the proximity effect and Andreev reflections [59] [18] weakening the superconducting properties near the interface. The exchange energy of the injected quasiparticles is also responsible for braking the Cooper pairs, further weakening the superconducting properties [59].

Figure 4.19 shows resistance as function of temperature for a configuration when the potential is measured over YBCO, while the current is injected through the whole sample. Here the superconducting transition is sharp down to a

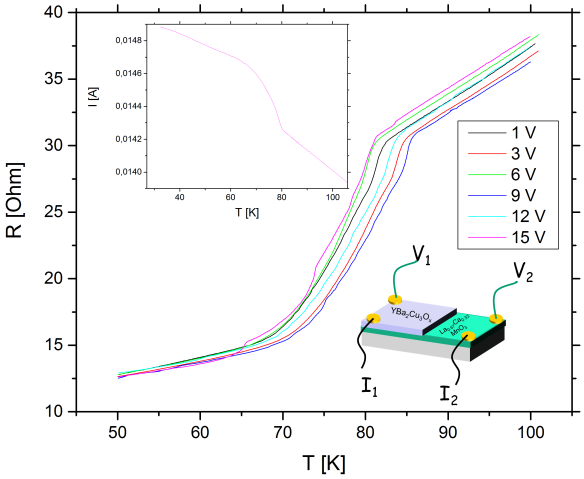

Figure 4.18: Temperature dependence of resistance in transport measurements for the superconducting transition region when both current and potential leads are mounted in the corners of the whole sample (lower inset). Upper inset shows the corresponding probing current when voltage of 15 V is applied.

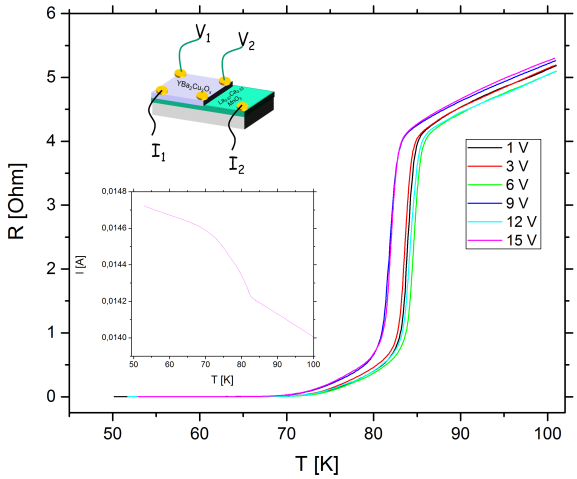

Figure 4.19: Resistance as function of temperature for the superconducting transition region when current is injected through the whole sample while potential is measured over YBCO (upper inset). Lower inset shows the corresponding measuring current when 15 V is applied.

resistance level of about 1 Ohm, after which a shoulder emerges before the resistance reaches zero. In this configuration, the spin-polarized current must flow over the interface once, as the two layers can be seen as two resistors in series thus explaining why the resistance below the superconducting transition is higher in this configuration compared to the resistance in figure 4.17 when the two layers can be seen as two resistors in parallel and current is allowed to partially overflow into the LCMO layer.

A suppression of the critical temperature, T_c, to a lower temperature is also seen in the configuration when current is injected through the whole sample but potential is measured over the YBCO layer, figure 4.19, as compared to figure 4.17, where both current and potential are measured over YBCO only. Suppression of T_c by spin injection is a known feature of SC-FM heterostructures [25].

To further explore the suppression of T_c induced by spin injection, IV-characteristics for the two configurations are shown in figure 4.20. From this figure, one can see that T_c is found between 80 and 85 K when there is no forceful spin injection. For the case with spin injection, T_c is found to be just above 70 K. Verifying that spin injection lowers T_c.

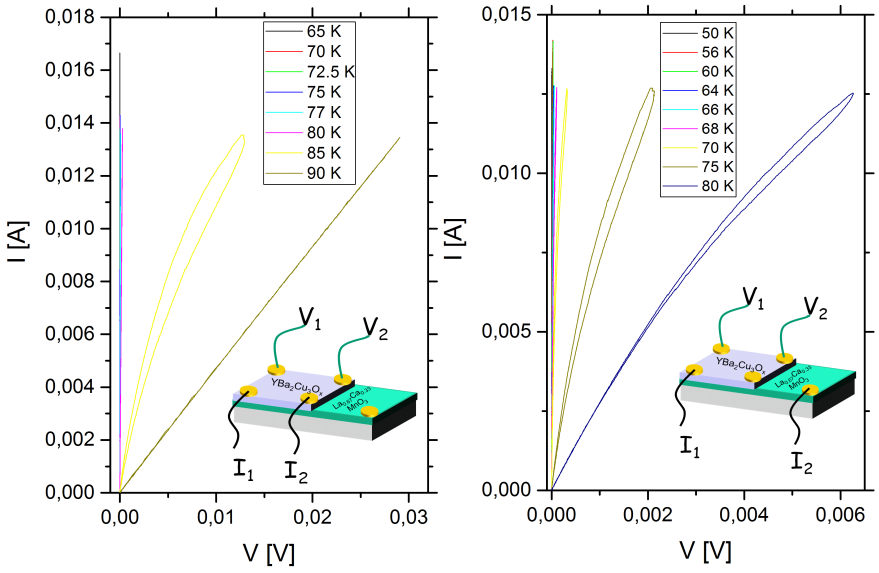

Figure 4.20: Current dependence on voltage obtained at different temperatures for the case with (right) and without (left) spin injection. When the current dependence on voltage becomes linear, the system is outside the superconducting state.

It is of interest to further compare the measurements shown in figures 4.19 and 4.17. In both cases, the potential is measured over YBCO, but the current is varied between injection through the whole sample and through YBCO in the

two figures respectively. One can then see that when current is injected through the whole sample, the resistance is higher before the superconducting transition, a shoulder emerges at the end of the transition, and the critical temperature is slightly shifted to a lower value.

To compare the two configurations, their resistance have been normalized and plotted in figure 4.21. Here the red curve represents the normalized resistance as function of temperature for the configuration when both potential and current leads are connected to the YBCO layer, and thus there is no forceful spin injection. The black curve represents the normalized resistance as function of temperature when potential is measured again over YBCO, while current is injected through the whole sample, and, thus, this represents the case when there is forceful spin injection as labelled thereafter. Comparing the black and red curves in figure 4.21, the differences mentioned above are clearly seen. In the case with spin injection, T_c is suppressed to a lower temperature and a shoulder emerges at the end of the superconducting transition, as compared to the case when the current is allowed to only partially overflow into LCMO, i.e. there is no spin injection. To further visualize the difference, a subtraction of the two curves have been performed and plotted in the same plot, labelled as difference (blue curve).

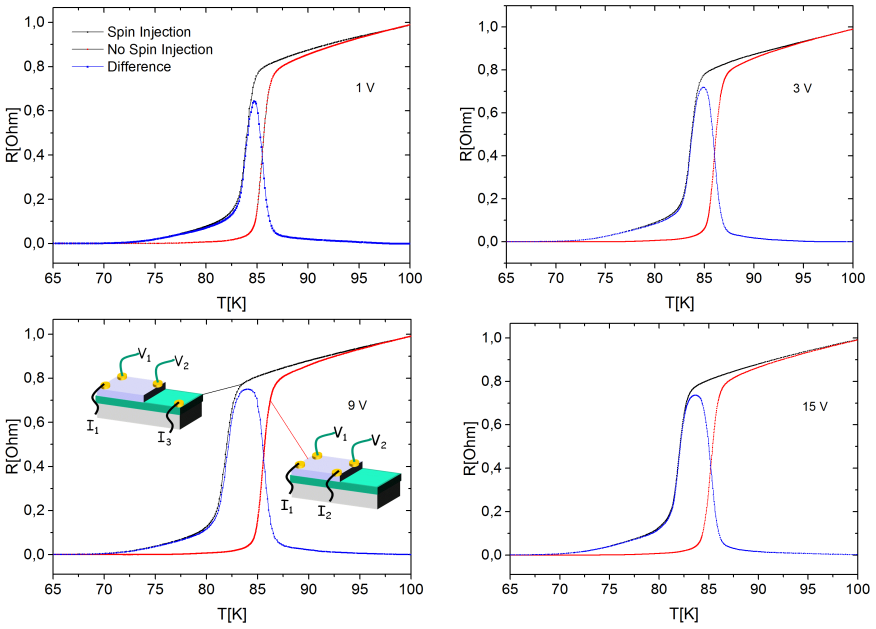

Figure 4.21: Normalized resistance as function of temperature for potential measured over YBCO while current is varied between spin injection into LCMO (black curves), and flow into YBCO, no spin injection, (red curves), for the applied voltages 1 V (upper left), 3 V (upper right), 9 V (lower left) and 15 V (lower right). The difference between the resistances for the two configurations is plotted in blue.

The four different graphs shown in figure 4.21 are representative for measure-

ments obtained with four different probing currents. In the upper left part voltage of 1 V, upper right 3 V, lower left 9 V and lower right 15 V was applied to the circuit. As the measuring current increases, the difference seems to increase both in height and width (the blue peak), though there is some inconsistency when one compares the curves for 9 and 15 V. The increased suppression of T_c by larger current density is consistent with results obtained in ref. [57].

The difference curves have a tail with finite resistance extending into the lower temperatures. Here one can see a correlation between the applied voltage and the spread of the curve into lower temperatures with finite resistance. Increasing voltage gives slight increase in the resistance at the tail, which is consistent for the whole voltage range. From figure 4.21, one can also see that the difference between no spin injection and spin injection is largest close to the superconducting transition.

4.3.1 LCMO100nm-YBCO200nm

Further investigation of the effect of polarized spin injection in the superconducting state of YBCO have been carried out on the sample LCMO100nm-YBCO200nm. Here a 200-nm YBCO layer was epitaxially grown on top of a STO substrate before a 100-nm thick LCMO layer was deposited to cover two thirds of the sample surface, as seen in figure 4.22. Further information about this sample have been given in section 3.8.

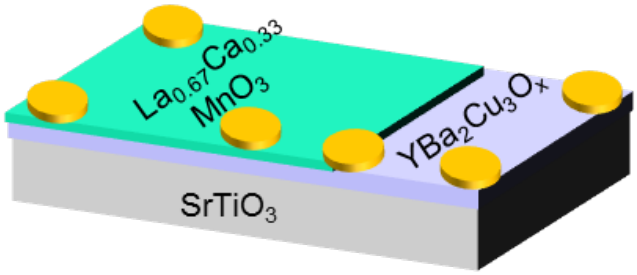

Figure 4.22: Schematic view of the sample LCMO100nm YBCO200nm with six indium contact pads mounted to its surface allowing for a range of transport measurement configurations to be explored.

To accurately determine the position of the two layers and their composition, EDX was performed, as the sample was not grown locally. Two EDX quantifying measurements, one from each side, were made and their results are included in appendix B.1. In the first EDX experiment, only small traces of elements from the LCMO layer were found, verifying that the first layer grown is YBCO. As the accelerating voltage of the beam is 15 kV, a strong signal from the thick substrate was also found making it difficult to accurately determine the oxygen content in the YBCO layer. In the second EDX experiment, both signal from the LCMO and YBCO were found, together with a strong signal from the substrate, verifying the layer structure described and showing correct chemical

composition relation between lanthanum and calcium, i.e. two thirds and one third, respectively.

To investigate the effect of polarized spin injection in the superconducting state of YBCO in this sample, both superconducting and magnetic properties of the layers need to be determined.

Firstly, the superconducting properties of the exposed YBCO layer was investigated with MOI. One of the images obtained with this technique is shown in figure 4.23. Before taking this image, the sample was cooled to 67.5 K while a magnetic field of 8.7 mT was applied the sample. The magnetic field is then gradually decreased by lowering the applied field to 6.3 mT. From figure 4.23, one can see that the superconducting response of the YBCO layer in this thin film is very weak. Only a small region of reasonably strong superconductivity in the upper middle part of the picture and very faint response area in the lower right corner can be seen. The contrast and brightness in this image is enhanced to better resolve the superconducting response. Some scratch removal have been performed as the MO-indicator film was scratched during earlier measurements.

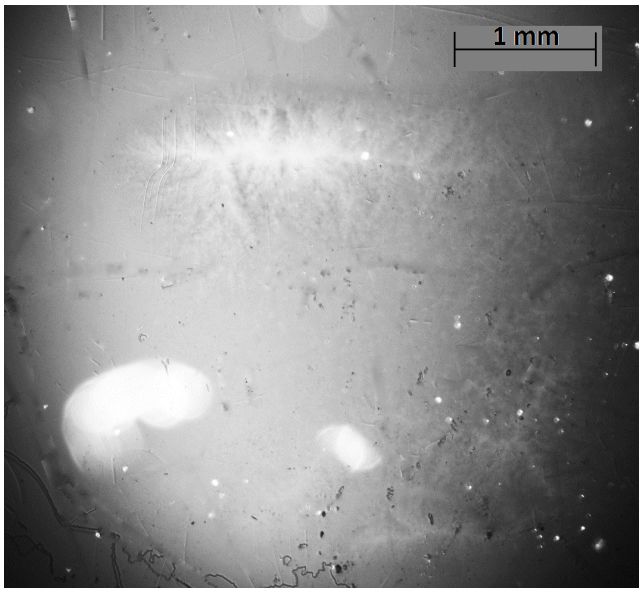

Figure 4.23: MOI image obtained when the LCMO100nm-YBCO200nm sample was cooled to 67.5 K with an applied magnetic field of 8.7 mT, which was reduced to 6.3 mT for this image. The two white dots in the lower left background is likely from dust particles trapped between the camera and MO-indicator film.

To further investigate the superconducting properties, one can look at the results of the transport measurements. Figure 4.22 shows a schematic view of the indium contacts attached to the sample. Throughout the experimental investigation of this sample, the current leads were mounted on the two upper-corner contacts, while the potential leads positions were varied among the four lower contact pads. Main results are presented in figure 4.24 to 4.26 and will

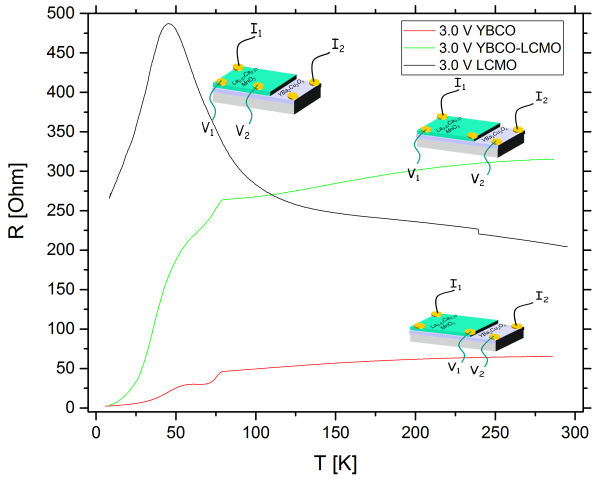

Figure 4.24: Temperature dependence of resistance for three different measurement configurations with voltage of 3 V applied to the circuit. The current is always injected in the corners of the whole sample, while for LCMO (black curve) potential is measured over LCMO only, for YBCO (red curve) one potential lead is mounted to the contact partially covering both YBCO and LCMO and the other is attached to the corner of YBCO, and for the YBCO-LCMO (green curve) potential is measured over the whole sample.

be described in greater detail in the upcoming paragraphs.

Figure 4.26 shows that the resistance becomes zero at low temperatures, confirming that the weak superconducting properties seen in the small areas of the sample with MOI are sufficient to decrease the system's resistance to zero.

To investigate the magnetic phase transition of the LCMO layer expected to take place at the Curie temperature close to 250 K, potential leads were attached to the two contacts on the LCMO layer only. The result is shown as the LCMO curve (black) in figure 4.24. Here indication that T_{Curie} have moved to a much lower temperature than expected 250 K is given by the resistance peak seen around 45 K. The small step observed at about 240 K is likely due to poor contacts.

As the oxygen content of colossal magnetoresistive material is known to be linked to changes in T_{Curie} [55] [28] [51], where the presence of oxygen vacancies tends to lower T_{Curie} compared to that of optimally-doped compound, an oxygen-deficient LCMO may explain the low T_{Curie} observed in figure 4.24. As both YBCO and the substrate (STO) contain oxygen, accurate determination of the oxygen content of the LCMO layer from the obtained EDX results appeared to be difficult.

The oxygen deficiency may have been introduced during growth and annealing

or occurred later as a result of diffusion. Since YBCO is also sensitive to its oxygen content, the weak superconductivity seen in the MOI (figure 4.23) could also be due to reduced oxygen content.

It is worth noting that in figure 4.24, the resistance at high temperatures is lower when the potential is measured over LCMO only as compared to the configuration when potential is measured over the whole sample. As the current is injected through the whole sample in both cases, the inconsistency in the measured resistance for LCMO is likely due to the fact that in this spread-resistance case not the whole potential drop over the sample is captured.

Figure 4.25 shows transport measurements obtained with potential leads in the same configuration as for the green curve in figure 4.24, where both the potential and current leads are connected to the corners of the whole sample. Here the applied voltage takes values of 1, 3 and 5 V. To further resolve the red curve in figure 4.24, a separate plot corresponding to different applied voltages ranging from 0.1 to 5 V is shown in figure 4.26.

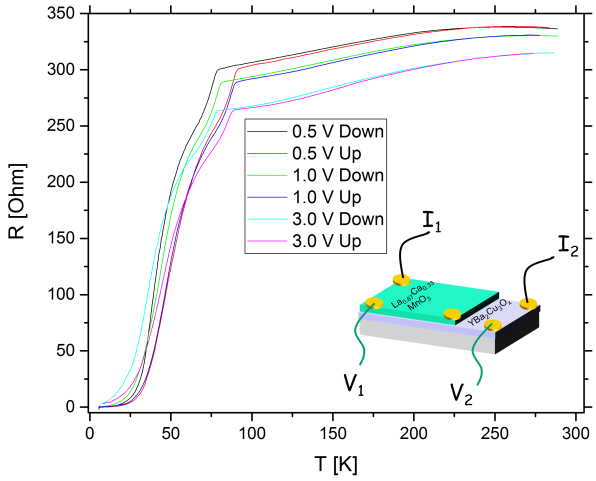

Figure 4.25: Temperature dependence of resistance obtained while current is injected and potential is measured over the whole sample at different applied voltages. The figure shows some hysteresis between measurements performed while heating ('Up' in figure legend) and cooling ('Down' in figure legend) the sample.

For both figure 4.25 and 4.26, measurements obtained while cooling and heating the sample are shown with different curves denoted by down and up (on temperature) accordingly. One can see that some hysteresis is present, most likely because the measurements were obtained at a finite speed, thus not able to eliminate this effect completely. It is safe to assume that the true value is found somewhere in-between these curves.

The superconducting transition shown in figures 4.25 and 4.26 is not what

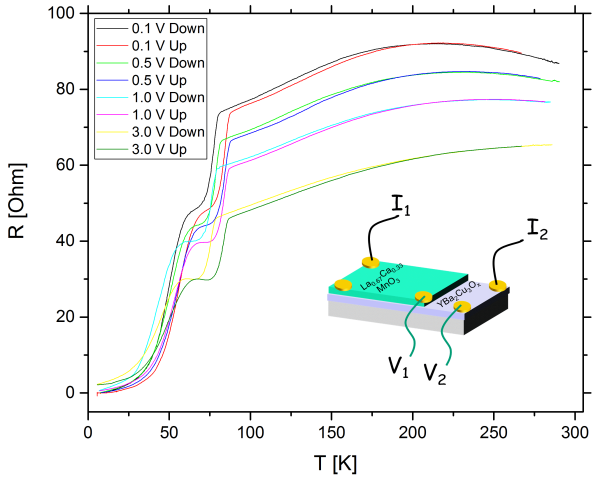

Figure 4.26: Resistance dependence on temperature for transport measurements obtained with heating and cooling the bilayer when current is passed through the whole sample and potential is measured over YBCO only.

one would expect to find if YBCO were to be measured on its own. Both configurations show a wide transition with what appears to be like a step, where in figure 4.26 the step is sharper.

The position of this anomaly observed in both configurations coincides well with the point, where LCMOs resistance stops increasing in an exponential manner, as seen in the black curve in figure 4.24, and the magnetic transition in the material is found. This leads one to assume that polarized spin injection may explain existence of this feature in figures 4.25 and 4.26.

Further support for the link between the onset of spin injection and the appearance of a step-like feature is found if one compares the superconducting transition seen in figure 4.18, where the Curie temperature is found to be at 240 K and that which is shown in figure 4.26. In figure 4.18 a wide transition is observed, but without the step-like feature as in 4.26.

As current is flowing through the whole sample, forceful spin injection (below T_{Curie}) is present in all the obtained transport measurements presented here for the sample LCMO100nm-YBCO200nm. The charge carriers must thus cross the interface between YBCO and LCMO once. Due to the half-metallic properties of LCMO, it is likely that an interface resistance emerges as only one spin channel is present at the Fermi level in LCMO while an even distribution of available states, for spin up and down, is available in YBCO.

As mentioned earlier, injection of polarized quasiparticles is known to lower the critical temperature [25], as seen in both figure 4.25 and 4.26 with T_c of about 80 K, giving support for the proposed explanation.

Also mentioned earlier, is the fact that both proximity effect and Andreev reflections are suppressed when the superconductor is in electrical contact with a half-metallic compound [18] [59]. This may be responsible for the unusually wide superconducting transition seen in both figure 4.25 and 4.26 together with the fact that the spin lifetime is shown experimentally to be many orders of magnitude larger in superconductors than in ferromagnetic materials [38].

As current is flowing through the whole sample for the measurements shown in figures 4.25 and 4.26, the difference in them is likely to come from the way we measure the potential in the two configurations.

When potential is measured over YBCO, it is important to note that the contact pad in the right corner of YBCO, as seen in figure 4.22, partially covers both the YBCO and LCMO layers. It opens for the possibility that a contribution to the measured resistance comes from the much more resistive LCMO layer. This should, though, not be a dominant effect when resistance of YBCO reaches zero for temperatures below 25 K.

4.3.2 PHYS63

The sample PHYS63 is a bilayer thin film with a 200-nm thick YBCO layer on top of a 200-nm thick LSMO layer grown on a substrate of STO, as seen in figure 4.27. Here calcium is substituted with strontium, slightly altering the thin-film properties compared to those of LCMO. A higher T_{Curie} is to be expected and half-metallic properties in transport measurements are reported to be present in ref. [45].

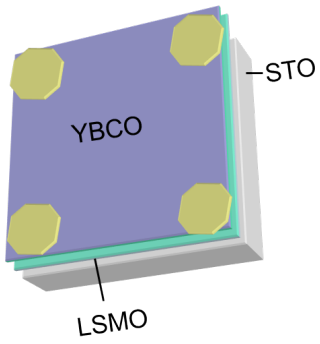

Figure 4.27: Schematic view of the sample PHYS63 with four contact pads mounted in the corners of the sample, which corresponds to the Montegomery measuring technique.

MOI measurements show good superconducting properties in the top layer, as seen in figure 4.28. The white rim around the sample is evidence of expulsion of magnetic flux from the interior of the superconductor, which is forced to accumulate around the sample. Brighter areas inside the sample show that this is not a perfect superconductor, as flux is allowed to penetrate large areas of its interior in a non-uniform manner.

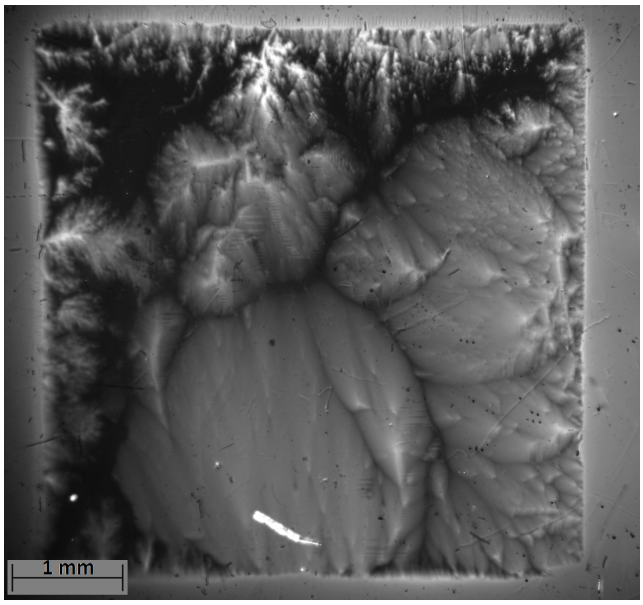

Figure 4.28: MOI image obtained when the Phys63 sample is cooled to 6 K in zero magnetic field and then subjected to increasing field. Here 9.18 mT is applied by the magnetic coil. In-plane size of the sample is 5mm x 5mm. Picture is taken by Thomas Håbu Qureishy.

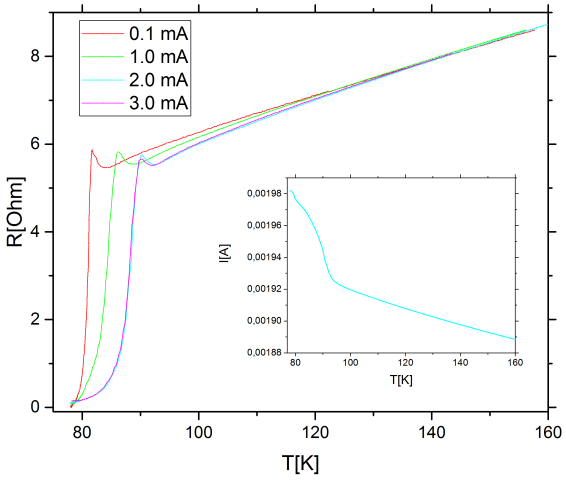

Figure 4.29: Resistance as function of temperature obtained in transport measurements of PHYS63 for four different probing currents. The inset shows the current dependence on temperature.

From figure 4.29, no clear evidence for the Curie temperature was observed. This is expected, since T_{Curie} for LSMO is usually found at a temperature much higher then room temperature and thus outside the temperature interval investigated here. T_{Curie} even in the range of 400 to 450 K is reported for this compound in [60], where lower lattice strain produces higher T_{Curie}.

The overall resistance seen in the transport measurements presented in figure 4.29 is low, likely due to the fact that both the current and potential leads are mounted on the YBCO layer. An unanticipated observation revealed here is the higher-resistance state emerging just as the superconducting transition is about to begin.

As the origin of this resistive peak is unknown, some possible explanations will be discussed in the following paragraphs.

Following the outline of this thesis, such observation might be explained through polarized-spin injection. As more and more current is overflowing into the LSMO layer, the interface resistance may emerge due to the half-metallic nature of LSMO, in which only one spin channel is available at the Fermi level. As the value of the current is sharply increasing when the superconducting transition occurs, so should the effect of spin injection increase accordingly.

Support for the claim of spin injection as the origin of the resistive state emerging at the onset of the superconducting transition due to higher measuring currents is not found if we look at the temperature dependence of resistance as function of load voltage in figure 4.29. Here one would expect that higher voltage would give both a larger resistive peak and a larger suppression of T_c compared to the predicted T_c for optimally doped YBCO bulk of about 92 K. From figure 4.29, the opposite is actually observed. Further, one can see that lower current injection gives higher resistance also in the normal state, which is typical for semiconductors. This may thus be an indication that T_{Curie} have moved to a much lower temperature, as discussed in earlier sections, and is found around the superconducting transition. This would then explain the increase of resistance seen just before the superconducting transition in figure 4.29.

Epitaxial growth of YBCO in multilayer thin films is a difficult procedure. Strain due to lattice mismatch can lower the critical temperature, and this could explain the reduced T_c observed in transport measurements shown in figure 4.29. Strain would also be a possible explanation to the far-from-optimal superconducting properties observed in MOI.

As the transport measurements presented for sample PHYS63 are made in liquid nitrogen, the speed of measurement is hard to control and this might contribute to the observations made just before the superconducting transition, both with regards to the resistive peaks and the difference between different measuring currents. As the temperature sensor and sample are not in perfect thermal contact, some difference between the actual and measured temperature of the sample may occur, especially when the measurements are not performed at a slow enough speed, which might be the case here.

As the sample is subjected to Joule heating during the measurements, some additional explanation may be found here too. It has been shown in experimental work performed on a similar system, like in ref. [71], that if measures are not taken to reduce the effect of Joule heating, resistive states before the superconducting transition emerge for currents larger than 3 mA. The observations made in ref. [71] are similar to the observations made for the sample PHYS63, but as the resistive state emerges in the observations made here for measuring currents much smaller than 3 mA, this argument remains inconclusive. Though for a absolute comparison one must compare current densities, not absolute values.

The origin of the resistive state seen in figure 4.29 eludes to be explained in full, but its likely origin is in Joule heating combined with a delay in registering temperatures.

4.4 FMS439-PHYS471 - A revisit

As the sample FMS439-PHYS471 and its novel experimental results were the main motivation for the experimental work performed for this thesis, it is important to revisit them in the light of recent observations on samples YBCO200nm-LCMO100nm and YBCO200nm-LCMO100nm.

As the experimental evidence for an interface layer resulting in an unknown magnetic phase is strong, no attempt to disprove this conclusion will be made. But in the light of the recently obtained results concerning the effects of spin injection, the existence of a magnetic phase at the interface does not exclude the possibility that the Curie temperature has been reduced significantly to a value suggestively very close to T_c. Thus, spin injection can be the cause of the resistive state observed below the superconducting transition. This is supported in threefold: by the fact that the Curie temperature could be moved to higher temperatures by applying strong magnetic fields, which may be the case in our magnetic measurement; by the increase in resistance observed as the temperature is lowered towards T_c in transport measurements, a behaviour typical for LCMO above Curie temperature, and the dependence of the resistive peak on probing current density. Comparing the results for the sample FMS439-PHYS471 and the resistivity peaks seen in figure 4.2 with the results obtained for sample YBCO200nm-LCMO100nm in figure 4.21, one can note a striking resemblance of the resistance peak and the difference resistance curve, giving support to the proposed effect of spin injection.

A possibility that a magnetic phase close to the interface with a Curie temperature approximately equal to T_c is the cause of resistive state anomaly is an interesting result on its own. If this is the case, carefully prepared thin films with oxygen deficient LCMO in combination with properly modified interfaces could lead to applications that may benefit from such non-linear change in resistance in a narrow interval of temperature.

As noted in [24], the sample FMS439-PHYS471 shows in SEM a rough surface. As a step in the experimental work performed in this thesis, SEM imaging of samples YBCO200nm-LCMO100nm and YBCO200nm-LCMO100nm have been done and reveal an interesting feature common to all three samples. In the article above describing sample FMS439-PHYS471, figure 8 shows, a LCMO surface, which appears to be filled with holes. Indeed, if LCMO is on the surface, the SEM images clearly show arrays of holes as seen in the lower image in figure 4.30. When YBCO is on the surface, the surface has small crystalline precipitates seen in the upper image in figure 4.30. SEM images taken from the central regions of the samples, show a combination of areas with both holes and precipitates. It is interesting to note that the presence of holes on the surface can enhance anisotropy in the electronic transport. As it is generally difficult to be absolutely certain that the features one sees in SEM images are exclusively due to topology and not from element content contrast, AFM measurements in contact mode where performed on the sample YBCO200nm-LCMO100nm. The result is presented in figure 4.31 and confirms the surface structure described above.

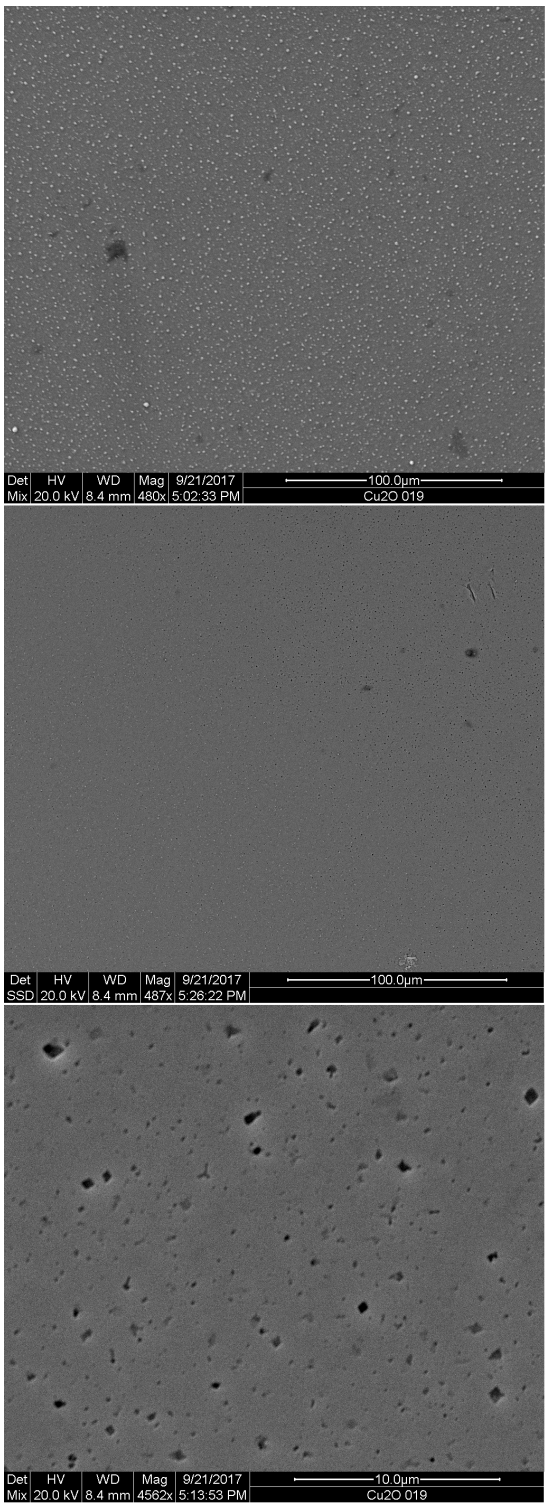

Figure 4.30: SEM images obtained on sample YBCO200nm-LCMO100nm. In the upper and lower image, YBCO and LCMO are seen at the surface, respectively. The middle image shows the region with both YBCO and LCMO exposed. Both precipitates and holes are visible in this image.

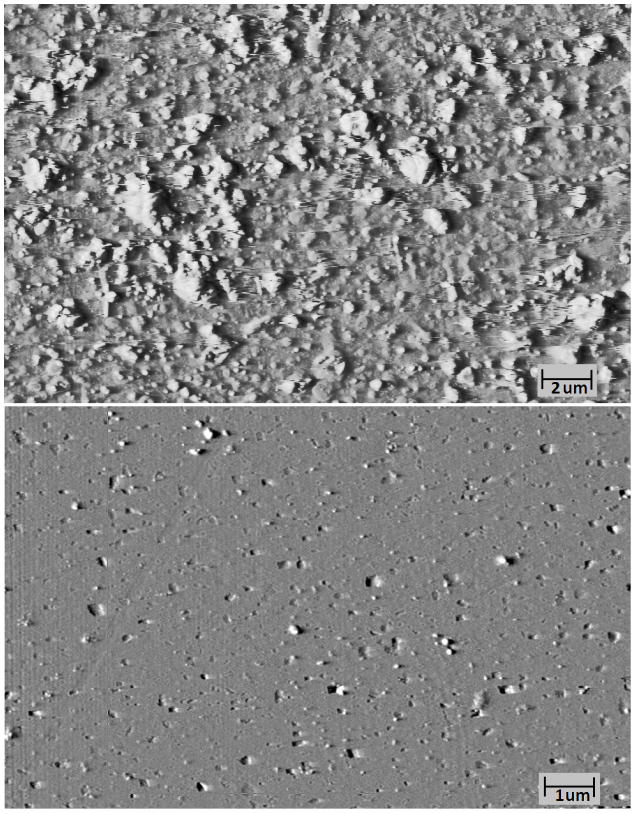

Figure 4.31: AFM images of sample YBCO200nm-LCMO100nm. The upper and lower image are obtained on exposed YBCO and LCMO layers, respectively.

CHAPTER 5

Conclusion and Future Outlook

In this study, one has seen that epitaxially growing thin films with the desired properties is an art for the skilled and experienced, and that small variations in growth conditions can lead to large variations in the material properties. One has seen that varying the oxygen content of LCMO has strong effects on its properties, where T_{Curie} could be found at much lower temperatures then the expected 250 K. Especially exciting were the effects on the interplay between superconductivity and ferromagnetism in the case when T_{Curie} was found to reside close to T_c.

The study performed in this thesis has been focused on the counteracting order parameters existing in superconductors and ferromagnetic materials, where singlet Cooper pairs, with anti-parallel spins, and the exchange energy compete with each other. Polarized-spin injection has been seen to suppress superconductivity, as evidenced by lowering T_c. Recent studies, on the other hand, have presented compelling evidence for the existence of triplet Cooper pairs with parallel spin orientation and showed how they can carry enhanced spin currents in superconductors without dissipation, giving great promise for the field of superconducting spintronics [32].

The need to further study the effects of spin injection into the normal state of the superconductor is clear, as this is a field of research not currently or previously explored and surprising results in resistance were obtained in the work performed for this thesis.

A question that needs to be answered is why the resistive anomaly found can emerge with different shapes based on how one injects the current over the interface: partial overflow gives an anomaly that stretched over a large temperature interval, whereas forceful injection gives a sharp cusp around 240 K. Is this related to the density of states available in the two materials close to the interface? Or is it merely an artefact brought forth by the Montegomery measuring technique?

As superconducting spintronics is a promising candidate for quantum computing [38], it will be of importance to also have extensive knowledge about how a superconductor interacts with ferromagnetism when the superconductor is in its normal phase.

Appendices

APPENDIX A

Historical Overview of Superconductivity

The eighteenth and nineteenth centuries were the era of discovery and development of the basic understanding of electrical conduction in metals. One of the first pioneers in this research was Benjamin Franklin, who based on observations done in his experiments with lightning, proposed that electrical charge could move along a metallic rod. The concept of electrical potential was later formulated by the Italian scientist Alessandro Volta, based on studies of static electricity and paving the way for the invention of the battery. This discovery allowed currents to be produced in metallic wires by putting them in contact with batteries. This gave the possibility to scientists to study the nature of electrical conduction. Among them was the German scientist Georg Simon Ohm, who found proportionality between the voltage applied to a conductor and the electrical current it produced. This proportionality law, published in [46], became a measure of how well a conductor could conduct electricity. Today we know this quantity as resistance and the relationship as Ohm's law. Ohm's law applies to most materials and is valid over a large range of resistances of the order of 10^{24} [54].

Paul Drude proposed that the conducting electrons in metals were restricted in their free movement by scattering from positively charged lattice ions vibrating at quantized frequencies called phonons [54]. Since the amplitude of the lattice vibrations is highly temperature dependent, a quest for investigating conduction at ever lower temperatures emerged.

At the turn of last century, three predictions about the resistive behaviour of metals just above absolute zero existed. These are outlined in figure A.1. William Kelvin proposed an increase in resistance as the temperature moved close to absolute zero to be caused by the electrons motion freezing. James Dewar, on the other hand, believed that as the temperature decreases, the phonon scattering would vanish and along with it the resistance. Augustus Matthiessen agreed with Dewar's prediction, but proposed that scattering by impurities would be independent of the temperature and cause the resistance to saturate at a finite value at absolute zero.

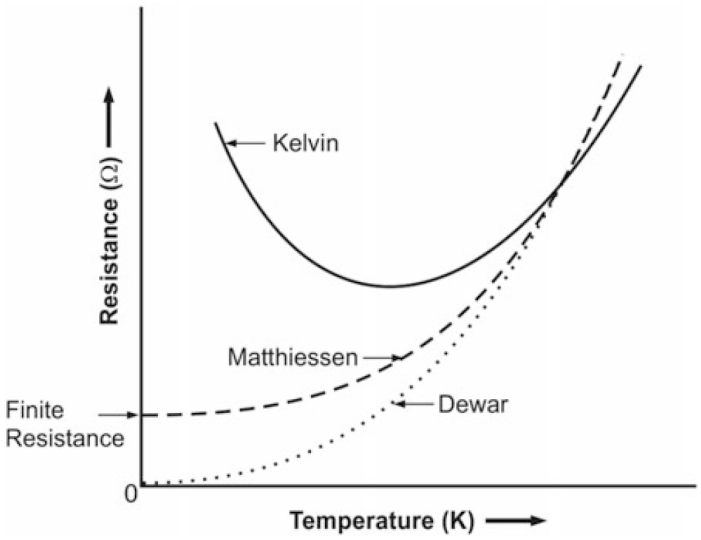

Figure A.1: The figure presents the three prevailing theories for resistance at low temperatures at the start of the twentieth century [54].

As ever more gases where liquefied, the low temperatures needed to investigate these hypothesis became available. Dewar moved towards confirming Matthiessen prediction as he measured finite resistance for gold and silver in liquefied hydrogen down to 16 K [15] [54].

As the finite resistance likely was caused by impurity scattering, the Dutch scientist Heinke Kamerlingh Onnes measured on the 8th of April in 1911 ultra-pure mercury, obtained through multiple distillations, in liquid helium. Liquefying helium was a feat he had managed three years earlier. To his surprise, the resistance of mercury suddenly dropped to zero at the boiling point of helium (4.2 K). The graph drawn in his notebook [47], shown in figure A.2, marked the discovery of a new state of matter: superconductivity [15] [36] [47] [54].

With similar experiments performed in liquid helium for other metals, it was soon realized that many of them behaved as Matthiessen had predicted. This substantiated the fact that superconductivity was an intrinsic property of mercury and the search for other superconducting materials started.

Kamerlingh Onnes was not convinced that the resistance really was zero, as it might just have dropped to an unmeasurable value. It was not before he was able to construct a circuit, where a perpetual current was shown to flow without dissipation for as long as the material was cooled below its critical temperature, that he concluded that the resistance really was zero [15]. For his research, Kamerlingh Onnes received in 1913 the Nobel Prize in Physics [4].

In the years that followed, more superconducting elements were found and experimental facts about the phenomena were collected. Not only did supercon-

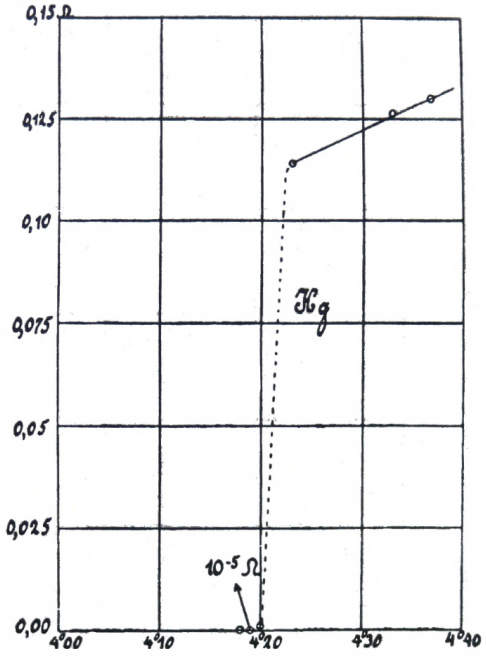

Figure A.2: The original graph showing resistance as function of temperature for mercury from Kamerlingh Onnes's personal laboratory journal [47] marking the discovery of superconductivity.

ductivity disappear above the critical temperature, T_c, but also when applying a current or magnetic field higher than the material specific critical parameters j_c and H_c, respectively. Figure A.3 shows the relationship between the critical parameters T_c, H_c and j_c as a critical surface [54]. Here one can see that as the temperature becomes close to T_c, both H_c and j_c move towards zero. The same is true about the other parameters. Their values are thus inter-dependent.

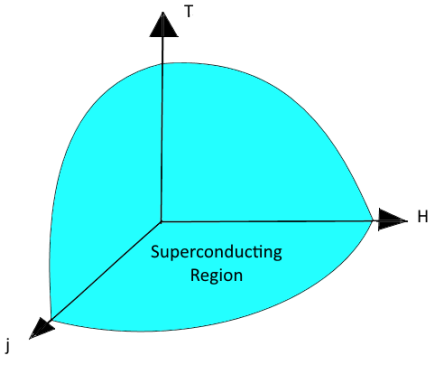

Figure A.3: The figure shows the relationship between the critical parameters T_c, H_c and j_c by which superconductivity can be suppressed when exceeded.

In Berlin, in 1933, by measuring the magnetic field distribution around a

superconductor, Walther Meissner and Robert Ochsenfeld found that as a superconducting sample was cooled below T_c, the magnetic flux was expelled from its interior [42], as shown in figure A.4. This came as a big surprise, as James Clerk Maxwell's laws predicted that the magnetic flux would freeze and remain constant in a perfect conductor [54]. This proved that a superconductor is also a perfect diamagnet. Screening currents close to the surface of the superconductor create a field opposite and equal to the applied external field, allowing for the incredible ability of superconductors to levitate magnets above or below them [15] [54] [67]. This effect of expelling magnetic field is now known as the Meissner effect.

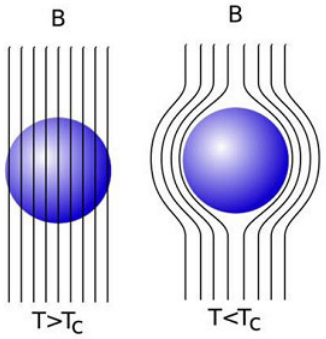

Figure A.4: Illustration of the Meissner effect: magnetic flux is expelled from the interior of a superconductor when the temperature is below T_c. The figure is taken from [7]

Fritz and Heinze London successfully explained the Meissner effect in 1935 when they derived the two London equations. Through their equations, it became clear that magnetic field is exponentially expelled from a superconductor and the depth, at which magnetic field can penetrate into a superconductor became known as the London penetration depth, λ_L [39].

As experimental investigations of superconductors continued, it became clear that two types of superconductors exist, type I and type II. The division is based on their behaviour in an external magnetic field. For type I superconductors, only one critical magnetic field exists: H_c. As long as the external magnetic field does not exceed the critical value, magnetic flux is expelled from the interior of the superconductor. For type II superconductor, two critical magnetic fields exist: H_{c1} and H_{c2}. Below H_{c1}, type II superconductors behave as type I superconductors. When H_{c1} is exceeded, magnetic flux is allowed to penetrate the superconductor in the form of magnetic vortices. As the external magnetic field moves towards H_{c2}, more and more vortices are allowed to enter the superconductor. When the critical value H_{c2} is exceeded, superconductivity is destroyed [14] [41] [54]. Figure A.5 shows the relationship between magnetization and applied external magnetic field for the two types of superconductors.

At the superconductor-normal metal (SC-N) interface, two important length scales are at play: the penetration depth λ and the coherence length ξ. λ represents the depth at which magnetic flux can penetrate a superconductor

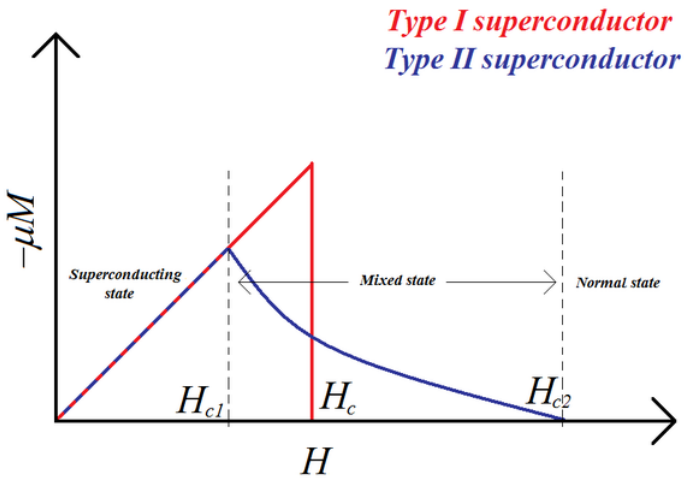

Figure A.5: The difference between type I and type II superconductors based on their behaviour in an external magnetic field. The figure is taken from [1].

and ξ represents the distance over which spatial variation in the density of superconducting electrons occurs. Figure A.6 shows the boundary between superconducting and normal regions for type I (left) and II (right) superconductors. Inside the superconductor there are two contributions to the free energy. A positive contribution comes from magnetization as this is the energy needed to expel the magnetic flux from the interior of the superconductor. A negative contribution comes from the superconducting ordering of the electrons in Cooper pairs. Deep in the superconductor, the two contributions cancel each other for both type I and II [54].

Since for a type I superconductor $\lambda << \xi$, as seen in a) in figure A.6, there is a larger positive contribution to the free energy close to the boundary, as seen in b), and a positive surface energy appears, as seen in c). For a type II superconductor the situation is reversed, as seen in d) and e), resulting in a negative surface energy [54], as seen in f). The result for type II superconductors is to favour partial magnetic field penetration, which is characteristic for the mixed state of this type of superconductor. The flux lines enter the superconductor carrying magnetic flux equal to one flux quantum of $\Phi_0 = \frac{h}{2e}$, where h is Planck's constant and e is the electron charge. They usually form a triangular lattice known as a Abrikosov vortex lattice [14] [41] [54]. Pinning of these vortices with suitable impurities have shown to be important for high magnetic field applications.

Through experiments with infrared radiation applied to superconductors, Glover and Tinkham found strong indications of the presence of an energy gap in superconductors. If the energy of the radiation is below a certain threshold value, the superconductor is reflective, i.e. no radiation is absorbed. For radiation with energy higher than the threshold value, the superconductor

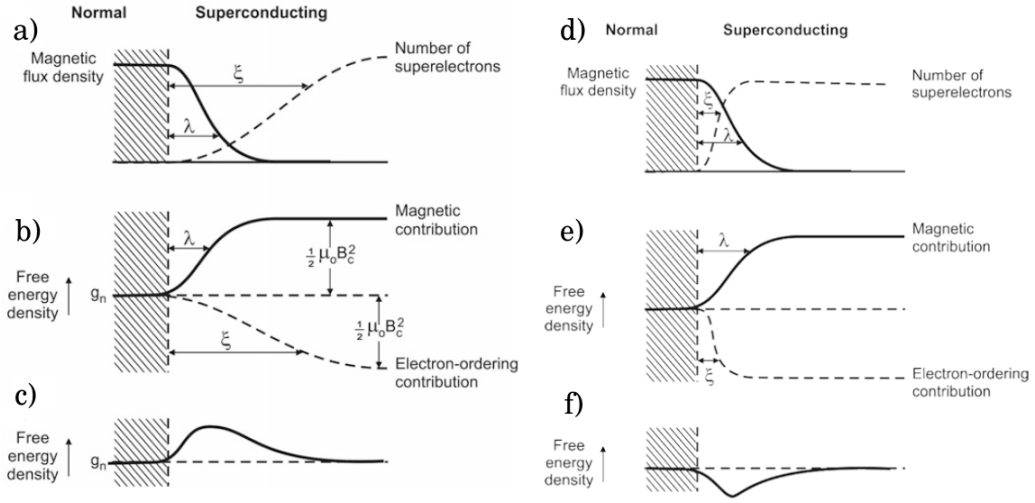

Figure A.6: The figure outlines the difference between type I (left) and type II (right) superconductors with respect to the two parameters λ and ξ and the resulting surface energy in a SC-N interface. The figure is adopted from [54] and modified.

absorbs the radiation with high efficiency [15].

This energy gap resembles that one finds in semiconductors, between the valance and conduction band, but its value has been found to be about three orders of magnitude lower than that in semiconductors, about 10^{-4} eV [54]. It is usually denoted Δ. The values of the energy gap have been shown to have strong temperature dependence, with their maximum found at absolute zero. As the temperature moves towards T_c, the value of the energy gap drops to zero [15] [54].

Another indication of the energy gap comes from the thermodynamical properties of the superconducting phase transition. At $T > T_c$ the heat capacity varies with temperature in a linear manner, but at $T = T_c$ a discontinuity jump takes place before exponential behaviour is seen for $T < T_c$ [41] indicating the presence of an energy gap.

A phenomenological explanation for the energy gap can be found from considering the formation of Cooper pairs [15]. As the electrons save energy by forming Copper pairs, a certain amount of energy is needed to break the pairs up, which is a binding energy.

As seen in figure A.8, a normal metal shows a linear dependence between the current and voltage. In a SC-N interface the current changes abruptly at a characteristic voltage, V_c, which represents the voltage needed to overcome the energy gap, centred at the Fermi level in the superconductor (as seen in figure A.7), for the normal electrons to flow into the superconductor. The small

current shown at low voltages represents electrons that are thermally excited over the gap [36].

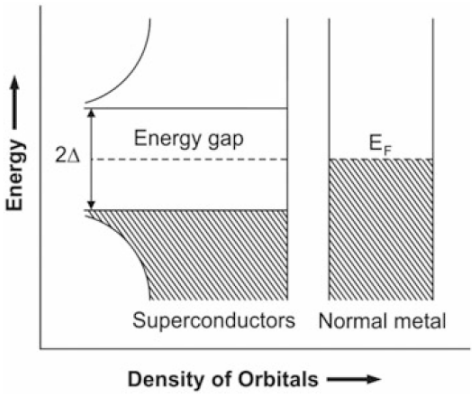

Figure A.7: The figure shows the difference between the density of orbitals as function of energy for a superconductor and a normal metal. The figure is adopted from [54].

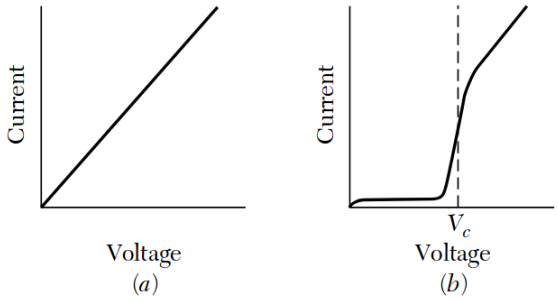

Figure A.8: IV characteristics for a normal metal (left) and a SC-N interface (right). The figure is adopted from [36].

In the years that followed Kamerlingh Onnes's discovery many prominent scientists tried to develop a compelling theory explaining superconductivity. Fritz London proposed superconductivity to be a macroscopic quantum phenomenon [15]. Vitaly Ginzburg and Lev Landau, in 1950, derived a phenomenological theory, in which superconducting ordering below the transition temperature could be expressed in terms of a complex order parameter Ψ [14] [54]. This theory was based on Landau's earlier work with phase transitions.

A breakthrough in explaining superconductivity came in 1957, when the three American physicists John Bardeen, Leon Cooper and John Schrieffer published a theoretical explanation for superconductivity in Physical Review [11]. Their theory was based on works performed by, among other, Emanuel Maxwell, who discovered the isotope effect in superconductors [14], Hebert Fröhlich, who pro-

posed phonons (lattice vibrations) to play a dominant role in superconductivity [41], Brian Pippard, with his non-local coherence length, ξ, over which the superconducting electron density changes from zero to its bulk value [41], and Rolfe Glover and Michael Tinkham, who showed the appearance of an energy gap in superconductors [15]. Leon Copper showed for a two-electron model that it could cost two electrons with opposite wavevector and spin at the Fermi surface less energy to pair up if an attractive potential is present [41]. The electron pairs would then form boson quasiparticles, obeying Bose-Einstein statistics [54], allowing them all to condense on the ground state.

With this, Cooper established the theoretical framework for the formation of Cooper pairs as a phonon-electron mediated process. Here electrons slightly distort the crystal lattice by attractive interactions between the conducting electrons and the ions forming the lattice. The relatively heavy ions remain distorted for a short time after the electrons have left, due to inertia, and this creates a local positive potential, which can attract another electron [15] [54].

To generalize this idea for a large number of Cooper pairs, Schrieffer realized that one single wavefunction would be needed to describe the behaviour of all the Cooper pairs as a collective. As the Cooper pairs are bosons, they are allowed to condense into one coherent state [41] [54]. Together Bardeen, Cooper and Schrieffer derived the BCS wavefunction, which was shown to explain most of the experimental observations done for superconductors [15] [41]. Their theory is today known as BCS theory and earned them the Nobel Prize in Physics in 1972. The BCS theory is the only widely accepted theory for superconductivity and it is successful in explaining superconductivity in elements and simple alloys with critical temperatures close to absolute zero.

APPENDIX B

EDS Results

B.1 LCMO100nm-YBCO200nm

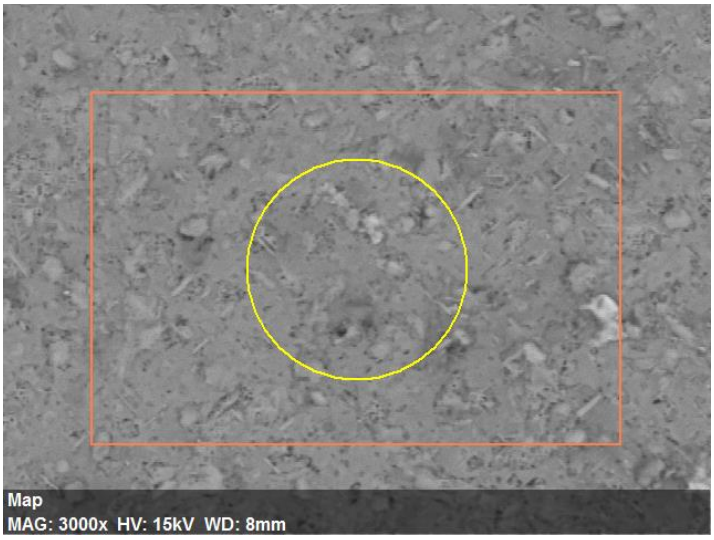

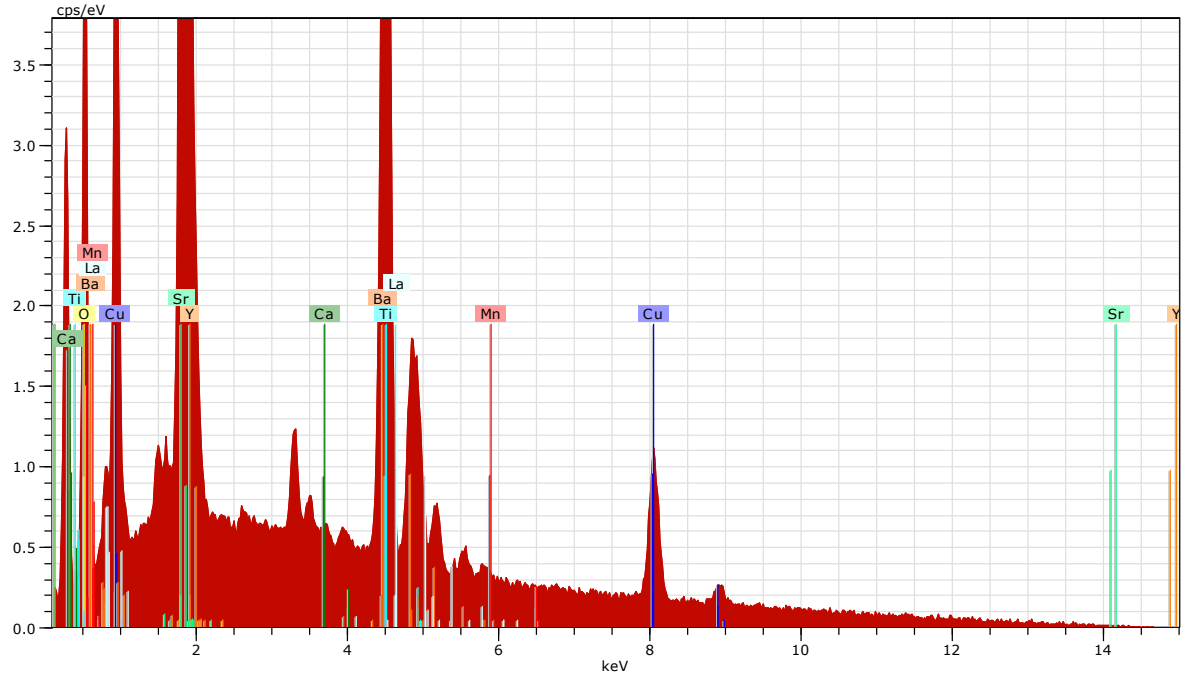

Spectrum: Point

Element	AN	Series	Net unn. C [wt.%]	norm. C [wt.%]	Atom. C [at.%]	Error [%]
Oxygen	8	K-series	14240	17.89	20.48	54.61	2.1
Titanium	22	K-series	33739	15.23	17.43	15.53	0.5
Strontium	38	L-series	49725	20.23	23.15	11.27	0.8
Copper	29	K-series	7295	12.28	14.05	9.43	0.4
Barium	56	L-series	24705	14.98	17.15	5.33	0.5
Yttrium	39	L-series	16747	6.27	7.18	3.45	0.3
Calcium	20	K-series	616	0.20	0.23	0.24	0.0
Manganese	25	K-series	118	0.08	0.10	0.07	0.0
Lanthanum	57	L-series	300	0.19	0.22	0.07	0.0
		Total:		87.35	100.00	100.00	

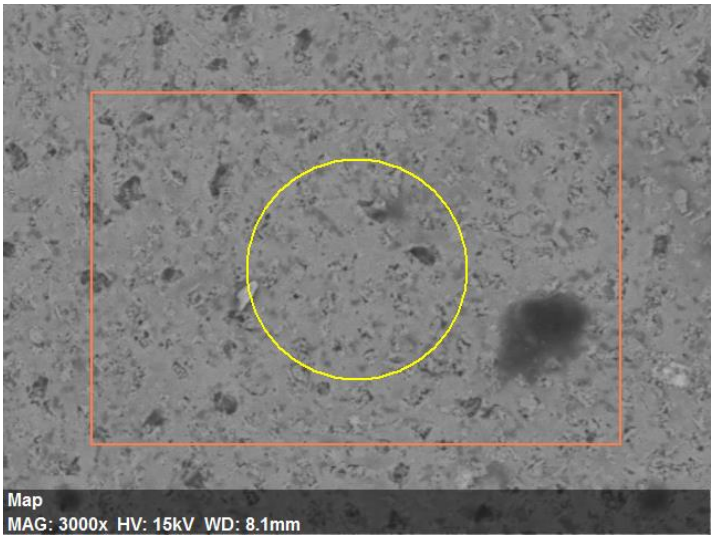

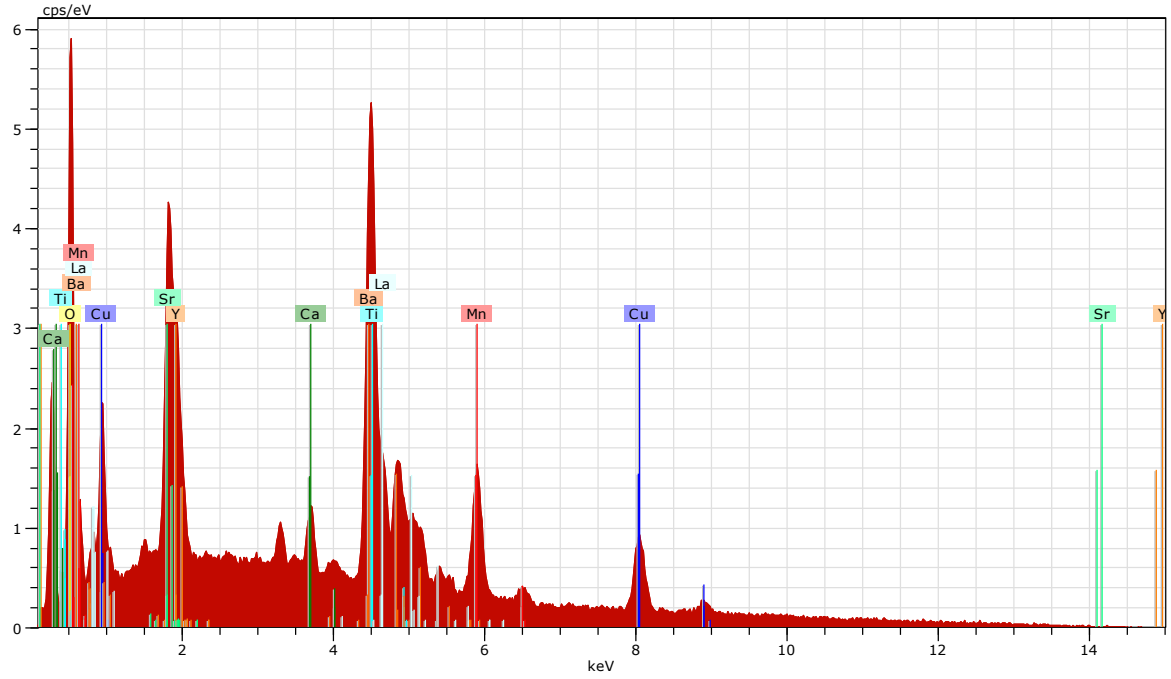

Spectrum: Point

Element	AN	Series	Net unn. C [wt.%]	norm. C [wt.%]	Atom. C [at.%]	Error [%]
Oxygen	8	K-series	18132	17.07	20.03	55.14	2.0
Copper	29	K-series	6327	11.53	13.53	9.38	0.4
Titanium	22	K-series	18798	8.55	10.04	9.23	0.3
Manganese	25	K-series	9276	7.15	8.39	6.72	0.2
Barium	56	L-series	26141	16.08	18.87	6.05	0.5
Strontium	38	L-series	19868	9.63	11.30	5.68	0.4
Lanthanum	57	L-series	13941	9.07	10.64	3.37	0.3
Yttrium	39	L-series	11040	4.92	5.77	2.86	0.2
Calcium	20	K-series	3836	1.22	1.43	1.57	0.1
		Total:		85.22	100.00	100.00	

B.2 YBCO200nm-LCMO100nm

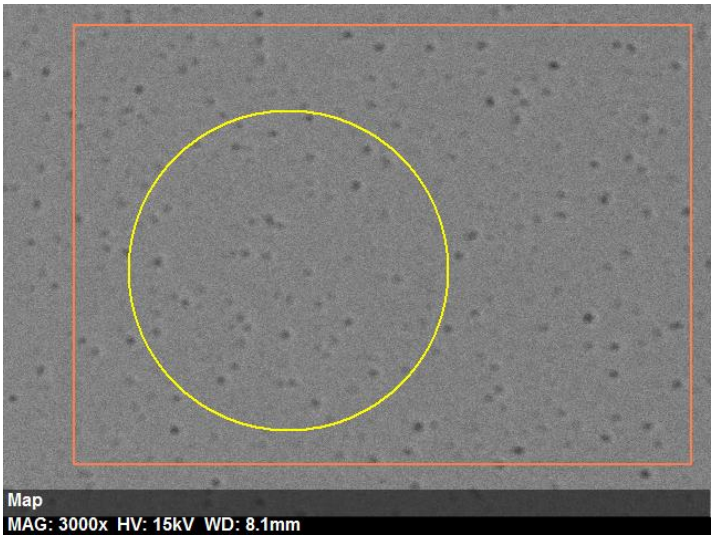

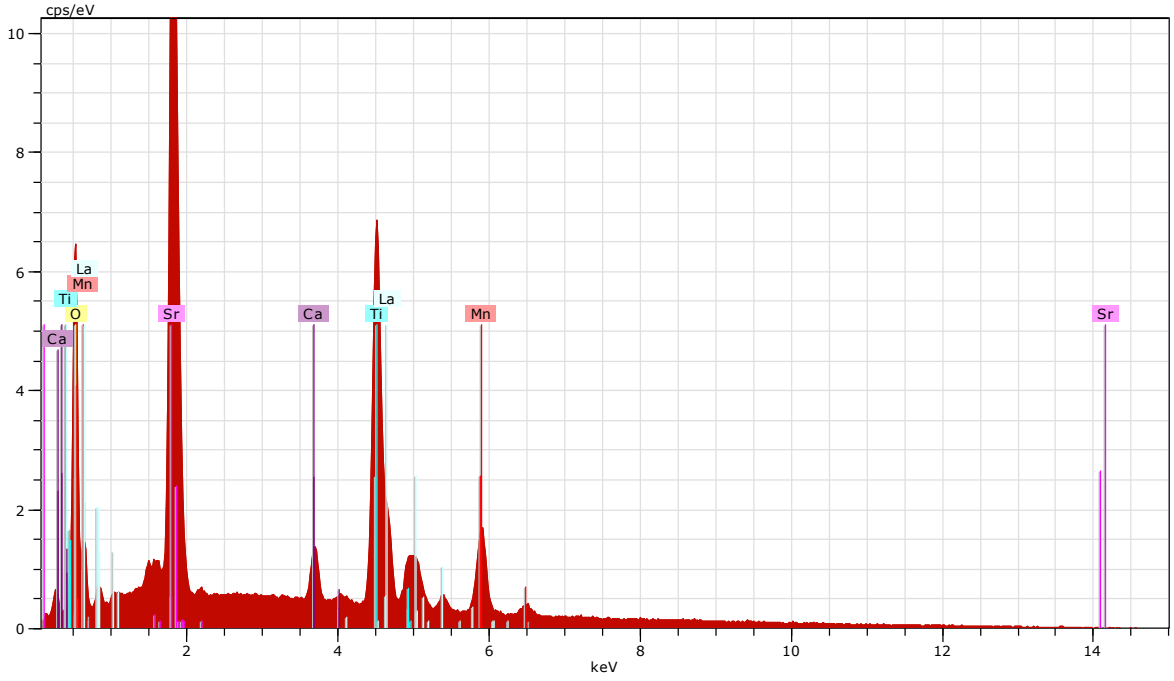

Spectrum: Point

Element	AN	Series	Net	unn. C [wt.%]	norm. C [wt.%]	Atom. C [at.%]	Error [%]
Oxygen	8	K-series	31878	29.71	29.03	64.06	3.3
Titanium	22	K-series	66069	19.43	18.99	14.00	0.6
Strontium	38	L-series	125570	31.80	31.07	12.52	1.3
Manganese	25	K-series	16630	7.94	7.76	4.98	0.3
Lanthanum	57	L-series	28128	11.67	11.40	2.90	0.4
Calcium	20	K-series	8638	1.79	1.74	1.54	0.1
		Total:		102.33	100.00	100.00	

APPENDIX C

Global and Local Properties

As was mentioned previously in this thesis, the Montegomery technique, i.e. four-corner measurement, has an advantage of probing local properties of the sample, like potential and resistance, without the disturbance created by highly-resistive contacts.

As a critical reflection over the measurements obtained, a Matlab script has been written, in which the resistance over the whole sample is extracted by assuming an idealized circuit and applying Hirchoff's circuit laws. The script is included in appendix D.1 and described in section 3.1.

When applied to the measurements obtained for samples YBCO200nm-LCMO100nm, LCMO100nm-YBCO200nm, FMS439-PHYS471 and PHYS63, the two latter show resistance that deviates in a peculiar manner from that obtained with the local Montegomery technique.

In the upcoming sections, all the above mentioned samples will be discussed in the light of the result obtained when we not only include the local properties, those obtained with the Montegomery technique, but also take into account the global properties, as calculated by the Matlab script in appendix D.1.

C.1 PHYS63

The resistance as function of temperature for the sample PHYS63 is shown in figure C.1, where the upper graph represents the global resistance as calculated with the Matlab script and the lower graph represents the local resistance as obtained with the Montegomery measuring technique.

In figure C.1, one can see that the anomalous resistive state just before the superconducting transition fails to come forth in the figure in the upper part, representing the global resistance of the thin-film sandwich sample PHYS63. Instead, a wide superconducting transition emerges, which is consistent with prior results for spin injection.

The superconducting transition seems to start at a temperature of about 92 K, consistent with the highest superconducting transition temperature for optimally doped YBCO. A possible explanation for the appearance of this optimal quality is that the measurements were obtained at not a slow enough rate of temperature change and that the temperature of the sample was slightly lower than that registered by the thermometer.

As a consequence of taking all the resistance contributions into considerations, contributions from both layers in the thin film and the contacts, the resistance is much higher after the superconducting transition than when the local resistance was evaluated.

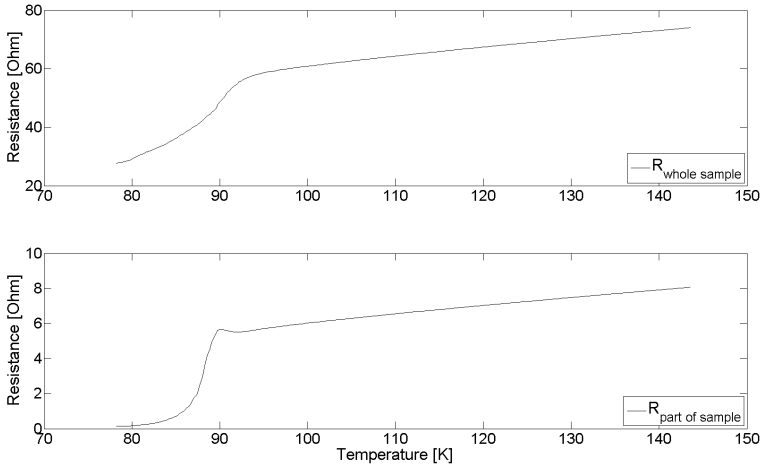

Figure C.1: Resistance as function of temperature for the sample PHYS63, when a probing current of 3 mA was passed through it. The lower graph shows one of the curves in figure 4.29, obtained with the Montegomery technique, while the upper graph shows resistance of the whole sample based on the applied voltage and potential measured over the constant resistance for the same flowing current, reflecting the global property of the sample.

C.2 FMS439-PHYS471

The striking resistive state emerging below the superconducting transition when current was injected parallel to the stripy features seen in MOI for the sample FMS439-PHYS471, presented in the lower part of figure C.2 obtained with the Montegomery four-corner technique, cannot be seen when the Matlab script calculates the global resistance, which is presented in the upper part of the figure C.2. Instead, a much higher overall resistance without anomaly appears.

It is important to note that although the resistive peak fails to come forth when the global properties are examined in this configuration, it is by no means saying that it does no exist. Figure C.3 shows the potential drop measured over the sample with the Montegomery technique. Here the resistive state is clearly present and thus a local property of the ex-situ thin film sandwich.

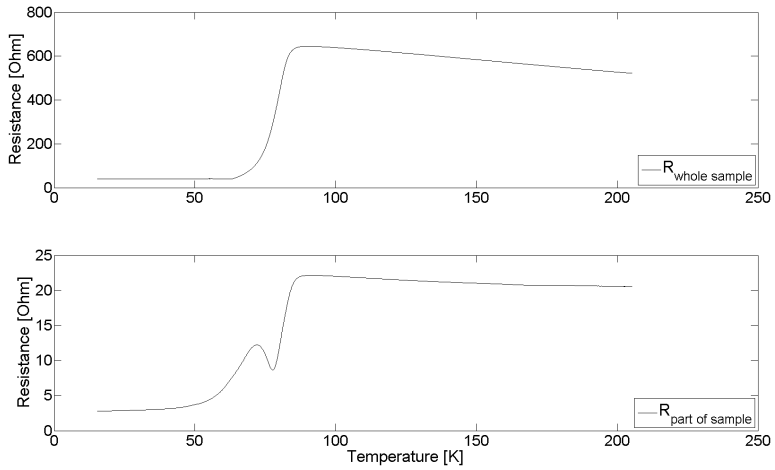

Figure C.2: Global- (upper) and local (lower) resistance as function of temperature for configuration, in which current was injected parallel to the stripy features seen in MOI.

When applying the Matlab script to the measurements obtained with current injected perpendicular to the stripy feature seen in MOI, the difference between local to global resistances is considerably smaller. As seen in figure C.4, the resistance increases by a fraction of that obtained for the local measurement.

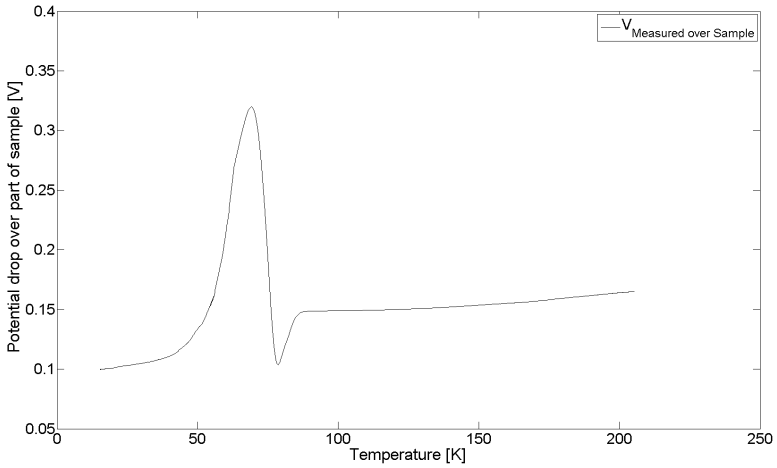

Figure C.3: The potential drop measured over the sample FMS439-PHYS471 with the Montegomery technique representing the local resistance captured over part of the sample.

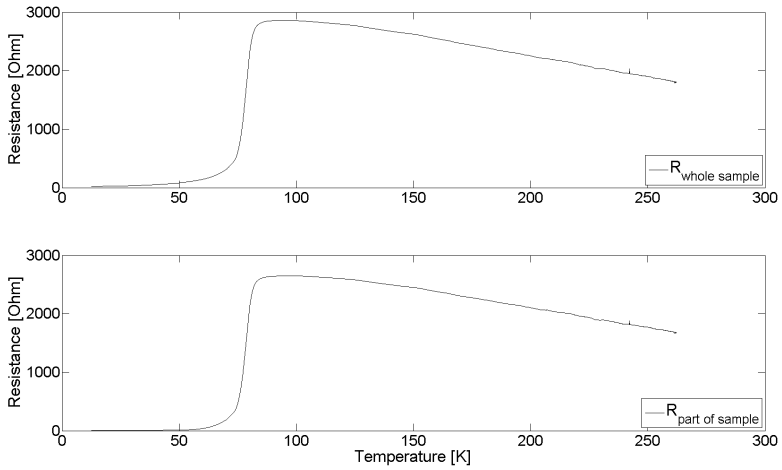

Figure C.4: Global (upper panel) and local (lower panel) resistance as function of temperature for the sample FMS439-PHYS471, when current is injected perpendicular to the stripy features seen in MOI.

C.3 LCMO100nm-YBCO200nm

The differences between the local and global properties obtained for the sample LCMO100nm-YBCO200nm are quite moderate and show an interesting pattern. As current contacts were attached to the corners of the whole sample for all the obtained measurements, similar global resistance was found by the Matlab script in all cases and presented in the upper graphs of figures C.5 to C.7 for the configurations when measuring potential over LCMO, YBCO and the whole sample respectively.

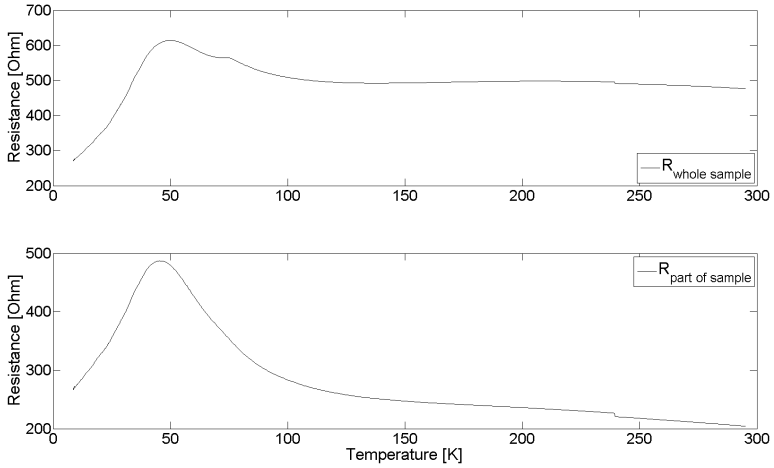

Figure C.5: Local and global resistance for the sample LCMO100nm-YBCO200nm as function of temperature, when potential is measured over the LCMO top layer only, shown in the lower and upper parts, respectively.

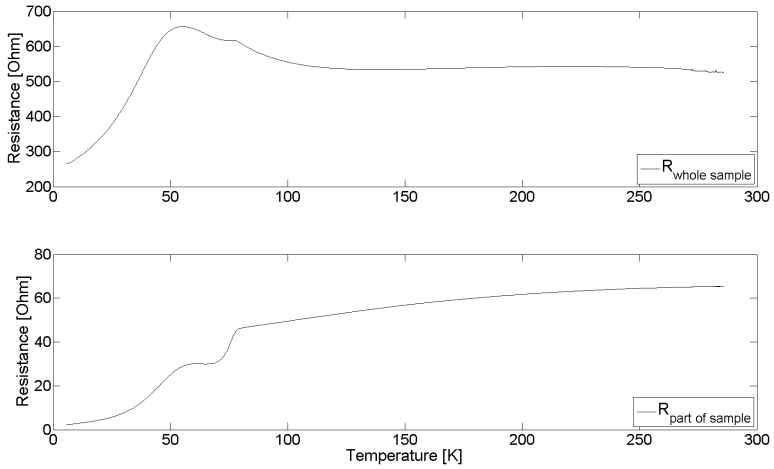

Figure C.6: Local (lower plot) and global (upper plot) properties of the sample LCMO100nm-YBCO200nm, when potential is measured over YBCO.

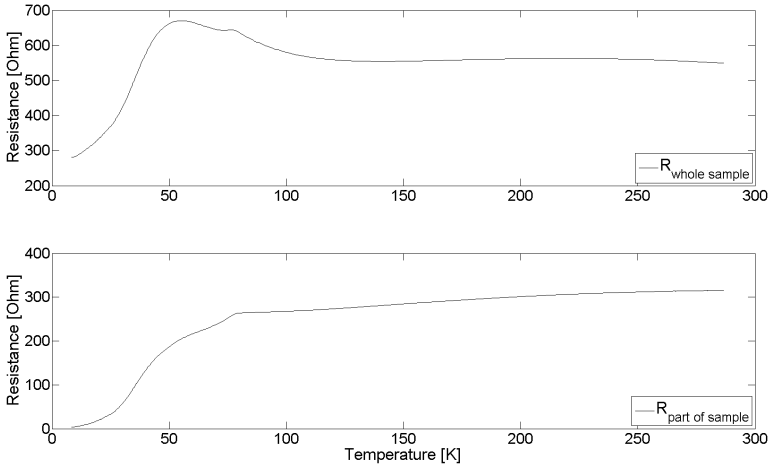

Figure C.7: Global and local resistance as function of temperature for configuration when potential is measured over the whole sample, shown in the upper and lower graphs, respectively.

In figure C.5, one can see the close resemblance between the global and local resistances of this sample. It is thus clear that the resistance of the LCMO layer dominates the resistance of the whole sample. Further support is found when all the other measuring configurations for the potential yield nearly the same global resistance. This is in line with expectation as the current was passed through the whole sample in all measuring configurations.

It is interesting to note that a cusp emerges in the resistance as the temperature is lowered towards the shifted Curie temperature. It coincides well with the onset of the superconducting transition seen in both figures C.6 and C.7

C.4 YBCO200nm-LCMO100nm

When comparing the global and local properties of the sample YBCO200nm-LCMO100nm, one can again see the evidence that the resistance of LCMO layer dominates the overall resistance of the sample, as shown in figures C.8 and C.9, for configuration where the current was passed through the whole sample.

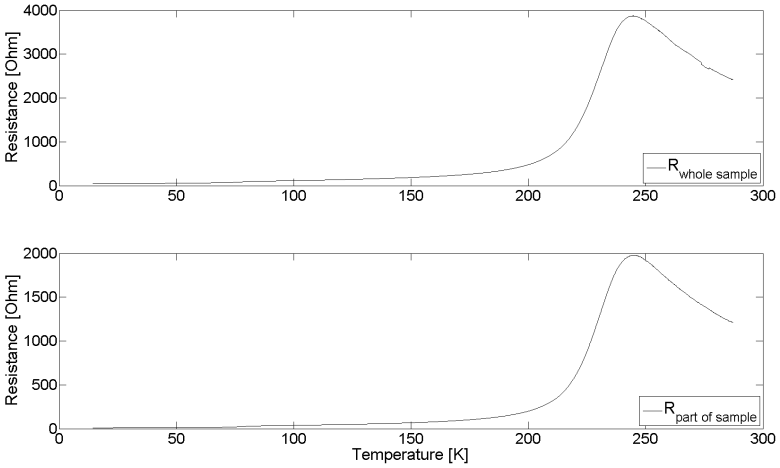

Figure C.8: Global and local resistance as function of temperature shown in the upper and lower graphs, respectively, for the sample YBCO200nm-LCMO100nm in configuration when both the current and potential wires were attached to the corners of the whole sample.

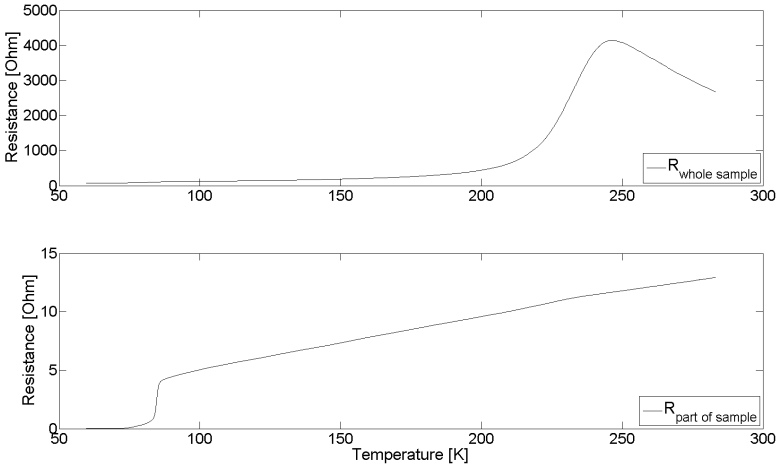

Figure C.9: Global (upper graph) and local (lower graph) resistance as function of temperature in the configuration when current is injected through the whole sample, while the potential was measured over YBCO only.

When the current is passed through the YBCO top layer, a contribution from the LCMO comes forth in the global resistance as compared to the local one, which can be seen in figure C.10. Here the resistance increases from varying in the range from zero to 6 Ohms locally to between 4 and 40 Ohms globally as function of changing temperature.

From the upper part of figure C.10, one can see that a long tail emerges globally for the superconducting transition, consistent with the evidence of spin injection as seen earlier in this thesis.

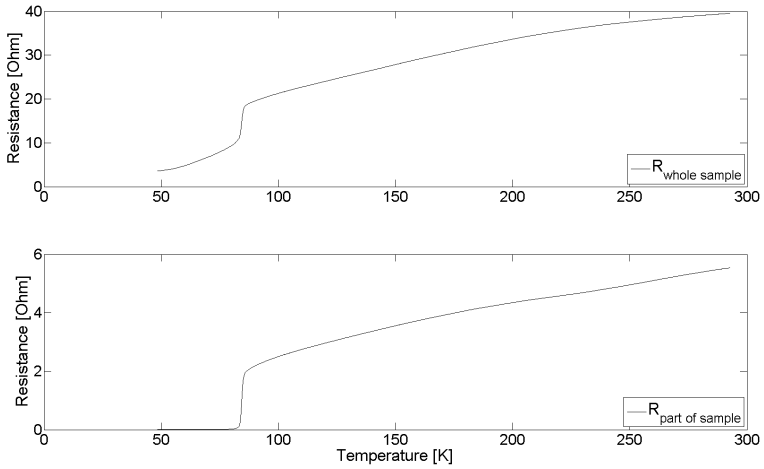

Figure C.10: Global and local resistance shown in the upper and lower parts of the figure, respectively, when both the current is injected through and potential measured over the YBCO top layer only.

APPENDIX D

Matlab Code

D.1 Global Properties

```
"""
%   New way to calculate I in circuit and R over sample.
%   Written by Trude BH 2018
%   Script is based on Kirchoff's circiut laws
%        and an idalized circuit
%   V_batt needs to be adjusted according to the
%    voltage set up by the power supply used
%    for the measurements at hand.
"""

V_batt=0.6;     %Volt
V_sample=V_batt-value8;
V_relation=V_sample./value8;
R_sample=V_relation.*constantR;
R_tot=constantR+R_sample;
I_tot=V_batt./R_tot;

figure(1)
subplot(2,1,1)
plot(Temperature, R_sample)
ylabel('Resistance [Ohm]', 'FontSize',22)
hold on
l1= legend('R_{whole sample}', 'location','southeast')
set(l1, 'FontSize',24)
legend('show')
set(gca, 'FontSize', 20)

subplot(2,1,2)
plot(Temperature, R )
l2 = legend('R_{part of sample}', 'location','southeast')
set(l2, 'FontSize',24)
legend('show')
xlabel('Temperature [K]', 'FontSize',22)
ylabel('Resistance [Ohm]', 'FontSize',22)
set(gca, 'FontSize', 20)

figure(2)
plot(Temperature, value6, 'DisplayName', 'V_{Measured over Sample}')
```

```
xlabel('Temperature [K]', 'FontSize',22)
ylabel('Potential drop over part of sample [V]', 'FontSize',22)
legend('show')
set(gca, 'FontSize', 20)
```

D.2 Obtaining Measurements

```
%LAKESHORE 332 Temperature controller


t=serial('COM3','flowcontrol','none','baudrate',9600,'DataBits', ...
      7,'Parity','odd','StopBits',1,'terminator','CR/LF');
fopen(t);

constantR=10;

% connect to Keithley  instrument#1
g=gpib('ni',0,16);
set(g,'EOSMode','read&write');
set(g,'EOSCharCode','LF');
fopen(g)

% connect to Keithley  instrument #2
g2=gpib('ni',1,14);
set(g2,'EOSMode','read&write');
set(g2,'EOSCharCode','LF');
fopen(g2)


% initilalize multimeter #1
fprintf(g,'*RST');
%fprintf(g,':DISP:ENAB OFF');
fprintf(g,':SYST:BEEP:STAT OFF');
fprintf(g,':CONF:VOLT:DC'); % measure typeRESET_test2multi

% initilalize multimeter #2
fprintf(g2,'*RST');
%fprintf(g2,':DISP:ENAB OFF');
%fprintf(g2,':SYST:BEEP:STAT OFF');
fprintf(g2,':CONF:VOLT:DC'); % measure type


last=50000;
for jj=1:last
hold on
%connecting to Lakeshore
fprintf(t,'CRDG? b');
measureC = fscanf(t);
readingsC(jj)=str2num(measureC);
%ticcc
%scanning chanel 8 on multimeter #1
%fprintf(g,':ROUT:CLOS (@8)'); % set chanel
fprintf(g,':INIT');
```

```
    fprintf(g,':FETCH?');
    measure8 = fscanf(g);
    value8(jj) = str2num(measure8);
    voltage8=value8(jj);
%TCh8(jj)=toc

%scanning multimeter #2
%fprintf(g2,':ROUT:CLOS (@4)'); % set chanel
fprintf(g2,':INIT');
    fprintf(g2,':FETCH?');
    measure6 = fscanf(g2);
    value6(jj) = str2num(measure6);
    voltage6=value6(jj);


I=value8/constantR; % works
R=value6./I;
Temperature= readingsC + 273.15;

% subplot(1,2,1)
%
% plot(value6(jj),I(jj),'r.')
% if(jj>1)
% plot(value6(jj-1),I(jj-1),'b.')
% end
% title('I V curve' )
% xlabel('V [Volts]')
% ylabel('I [Ampere]')
% % % % % %

%
% % % % subplot(1,2,2)
plot(Temperature(jj),R(jj),'r.')
if(jj>1)
plot(Temperature(jj-1),R(jj-1),'b.')
end

title('R(T)' )
xlabel('T [Kelvin]')
ylabel('Resistance [Ohm]')
% % % % %



% plot(Temperature(jj),R(jj),'b.') % Plot R against temperature
%
%
% live plot
%  plot(voltage6,voltage8,':k.');cl
%  title('I V curve' )
% xlabel('V [Volts]')
% ylabel('I [Ampere]')
hold on;
 drawnow;
% TCh6(jj)=toc
```

```
end
voltage6=mean(value6);
voltage8=mean(value8);

%plot(value6,value8,'r.-')
fclose(g)
fclose(g2)
fclose(t)
```

APPENDIX E

Article

E.1 Interplay Between Spin Polarization and Superconductivity in an ex-situ Bilayer of $La_{0.67}Ca_{0.33}MnO_3 - YBa_2Cu_3O_{7-\delta}$

Conference paper published in proceedings for the 2017 international conference: "Nanomaterials: Applications and Properties" and in the digital archive IEEE Xplore Digital Library. Article is found as ref. [24] in this thesis and through https://ieeexplore.ieee.org/document/8190363/. For this article the author of this thesis have contributed with some small written sections, proposed ideas and analysing transport measurements.

Interplay Between Spin Polarization and Superconductivity in an ex-situ Bilayer $La_{0.67}Ca_{0.33}MnO_3$ - $YBa_2Cu_3O_{7-\delta}$

A. S. Fjellvåg
Department of Chemistry,
University of Oslo,
Oslo, Norway
a.s.fjellvag@smn.uio.no

T. B. Hjelmeland, H. J. Mollatt, T. Qureishy, P. Mikheenko
Department of Physics,
University of Oslo,
Oslo, Norway
pavlo.mikheenko@fys.uio.no

***Abstract*—An anomalous magnetism is observed in an ex-situ bilayer of high-temperature superconductor $YBa_2Cu_3O_{7-\delta}$ and colossal magnetoresistive material $La_{0.67}Ca_{0.33}MnO_3$. The magnetism results in strong in-plane anisotropy of the resistance and surprising peak in the temperature dependence of resistance below superconducting transition associated with the interplay between superconductivity and establishment of the magnetic order. Magneto-optical-imaging reveals a stripy magnetic structure in the bilayer linked with unusual behavior of the resistance. The magnetization measurements demonstrate strong and irreversible magnetism, which is likely associated with re-orientation of the magnetic moment of interface. The observed non-linear resistance could find practical use exploring further link between superconductivity and magnetism of the interface.**

Keywords—high-temperature superconductor; colossal magnetoresistance material; bilayer; interface; nano-magnetism.

I. INTRODUCTION

A lot of effort has been put forward during the last forty years to develop the field of spintronics [1]. Spintronics applications have become widespread. One of the examples is its use in magnetoresistive random-access memory (MRAM) [1]. A special attention in the area is attracted to spin-based nano-systems that use high-temperature superconductors [2], as they may in the future be vital to quantum computing [3].

It is important to identify material combinations to properly merge spintronics and superconductivity enhancing the functionality and performance of nano-devices [2]. Systems like $YBa_2Cu_3O_{7-\delta}/La_{0.67}Ca_{0.33}MnO_3$ (YBCO/LCMO) generate a lot of interest due to interplay between full spin polarization in LCMO and superconductivity in YBCO. As these are competing states, it appears to be possible to control, for example, superconductivity in YBCO by spin injection from LCMO [4,5]. An advantage of working with these specific materials is that both have perovskite structure and similar crystal lattice parameters, and can therefore be grown epitaxially on top of each other.

In the present work, an ex-situ grown thin-film bilayer of LCMO and YBCO is investigated. It is unusual to grow these layers ex-situ, i.e. removing YBCO layer from the chamber and depositing LCMO layer after investigating YBCO layer. It was found, however, that the system shows new and attractive electronic properties different from those found in literature. The unusual magnetic state was found that establishes below the critical temperature (T_c) of the superconductor and strongly influences its behaviour. The magnetic state was directly visualized by magneto-optical imaging (MOI) and investigated by vibrating sample magnetometry (VSM). The interaction between this state and superconductivity leads to specific temperature dependence of resistance that could be used in practical applications.

II. EXPERIMENTAL METHODS

A thin-film bilayer of LCMO on YBCO has been epitaxially grown by pulsed laser deposition (PLD) on a $SrTiO_3$ substrate. The deposited YBCO layer of the thickness of about 100 nm was removed from the evacuated chamber before the deposition of LCMO. The YBCO film was exposed to air over a long period of time of few months with its surface modified due to interaction with oxygen in the atmosphere. A layer of LCMO of a similar thickness was deposited afterwards in the stoichiometric composition of the perovskite.

Temperature dependent resistance of the bilayer has been investigated with four-probe transport measurements with the temperature being cryogenically controlled using liquid helium. The electrical contacts to the sample were made with pressed indium in direct contact with the LCMO layer. Measurements were done with keeping a constant voltage of on the current leads.

Magnetic measurements have been performed with a Quantum Design Physical Properties Measurement System (PPMS) in the temperature interval 10 – 300 K in a DC magnetic field of 0.05 and 1 T. The sample was mounted with the plane of the film oriented at an angle of 20° with respect to the applied magnetic field to monitor both superconducting and magnetic states.

978-1-5386-2810-2/17/$31.00 ©2017 IEEE

X-ray diffraction (XRD) measurements were performed on a PanAlytical Empyrean diffractometer with a 4-bounce Barthels monochromator (asymmetrically cut Ge(220)) as primary optics and a PIXcel3D detector to check crystal structure of the bilayer. The scanning electron microscope (SEM) images were taken with a Hitachi SU8230 SEM to reveal the cross-sectional state of the layer.

In recent years, magneto-optical imaging (MOI) has been extensively used to visualize magnetic flux penetration in type-II superconductors [6-8]. It is especially efficient for thin superconducting and magnetic films and, therefore, was used in this work too. MOI was performed by sending polarized light through a magneto optical indicator film, which is a Faraday active crystal of Bi-substituted ferrite garnet deposited on a gadolinium gallium garnet substrate [9,10], mounted on top of the sample. A mirror deposited onto the indicator film and facing the sample reflects the light into another polarizer (named analyzer) oriented at 90° to the first, so only the light that changes its polarization angle contributes to the image. The polarization angle is changed depending on the distribution of magnetic field in the sample, and so light intensity in MOI images represents the strength of local magnetic field. The experiment was performed at a temperature of T = 3.8 K. A rotating magnetic field was applied with a permanent magnet to move the magnetic moment of LCMO out of plane of the film. Several images were taken while the magnet was rotated, and the differential images were obtained by a standard software procedure.

III. Results and Discussion

Fig.1 shows resistance of LCMO/YBCO sample as a function of temperature during the cooling, measured while keeping constant voltage between current leads of 0.1 (black), 0.3 (red), 1.8 (green) and 5.0 V (blue).

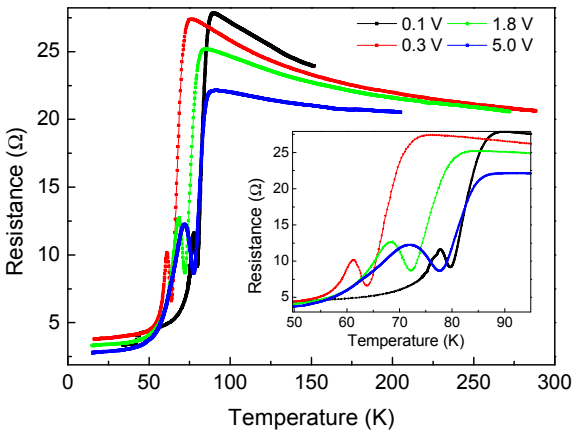

Fig. 1. Resistance of LCMO/YBCO as a function of temperature, measured during the cooling. The inset zooms on the high-resistivity peak

The expected drop in resistance, which is also two-dimensional resistivity of this square sample, observed below the critical temperature of YBCO (≈ 90 K). At higher temperatures there is semiconducting behavior all the way up to the room temperature. This is different from the expected metallic behaviour for YBCO and LCMO below 250 K [11].

Below T_c one would expect the superconducting state to dominate the resistance with its steady decrease at lower temperatures, but instead a voltage dependent peak in resistivity appears between T = 60 and 80 K (Fig. 1). The resistance peak width increases with applied voltage, and the peak position depends on voltage too. This peak has, for all voltages, an extended tail towards lower temperature, and the saturation resistance converges to approximately the same value.

A thermal hysteresis is observed when decreasing and increasing temperature at the same voltage, but in the measurements in which the sample was heated, the peaks at different voltages are close to each other (Figs. 2 and 3). Thermal difference between the sample and temperature sensor seems to be larger in the cooling-measurements. In agreement with this, the resistance tail is also less pronounced in the heating experiments. This suggests that superconducting state is suppressed below T_c in quite narrow temperature interval and quickly recovers just below the peak of resistance.

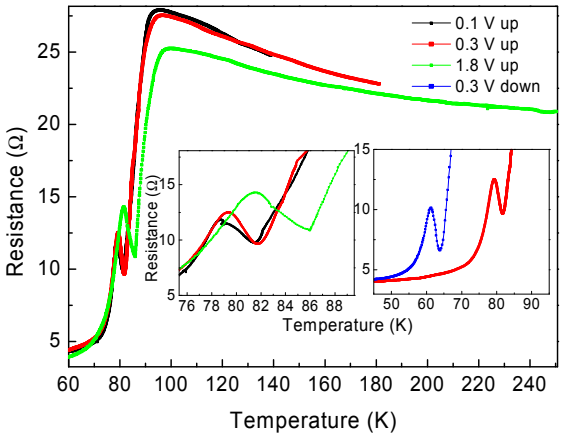

Fig. 2. Resistivity as function of temperature, measured during heating for constant voltages of 0.1 (black), 0.3 (red) and 1.8 V (green). It is also measured during cooling for 0.3 V (blue). The left inset zooms in on the resistance peaks, while the right inset compares heating and cooling measurement for 0.3 V

During transport measurements, the bilayer is also subjected to heating from the current flowing in the sample. Since the sample and temperature sensor are not in direct

contact with each other, a small difference exists between real and measured temperatures. The heating level is increasing with increased voltage, and can explain the larger width of resistance peak at higher voltages. Also, the 5.0 V measurement during heating was not possible to perform due to thermal damage of the sample inflicted by applying such a large voltage below the superconducting transition. The derivative of the resistivity flattens out much slower for the measurement at 5.0 V, either caused by additional heating or an extension of transition by current itself (Fig. 3).

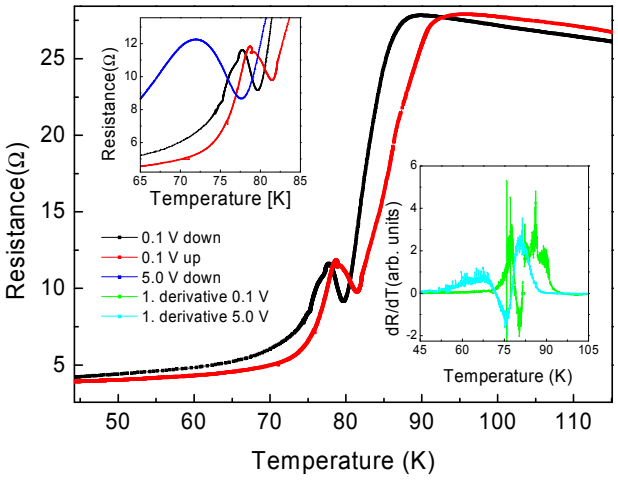

Fig. 3. Resistivity as a function of temperature for the 0.1 V measurements during heating (red) and cooling (black). The left inset compares these resistance curves with the measurement at 5.0 V, while the right inset shows the derivatives of the curves on temperature at 0.1 V (green) and 5.0 V (blue) obtained during the cooling

Further investigation of the magnetic state of bilayer was performed with MOI. The stripy features are observed on the surface of the film (Fig. 4), indicating a magnetic domain structure with narrow regions of suggestively alternating spin states.

This magnetic structure causes strong in-plane anisotropy of the resistance. Although LCMO is supposed to be in a uniform spin-polarized state, it forms periodical magnetic domains at low temperatures. This image was taken at 3.8 K, but it disappears at higher temperatures, roughly above the temperatures of the peak in resistance. It is then logical to clarify whether magnetic structure is the origin of the peak.

Even if the link between resistance peak and domain structure is unclear, the magnetic anisotropy strongly affects resistance of bilayer over a large temperature range. While in resistivity measurements performed parallel to the stripy domains overall resistance is not very high and one can see the resistance peak around 70 – 80 K (Figs. 1-3), this is not the case for measurements perpendicular to the stripy domains (Fig. 5). Charge carriers flow here is strongly impeded by the domains erasing peak and increasing total resistance to values much higher than in the parallel configuration.

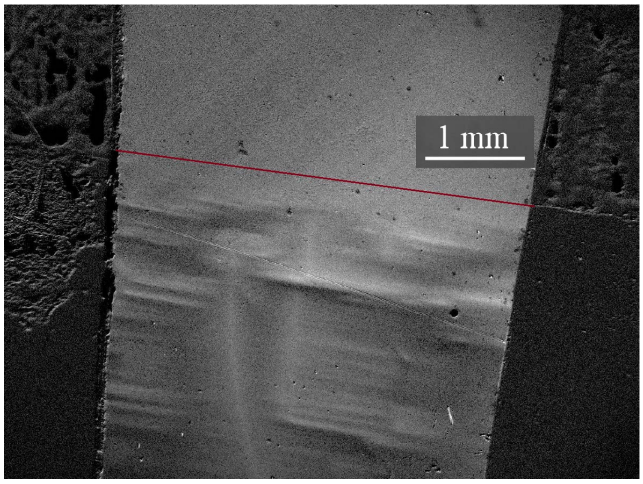

Fig. 4. A differential MOI image showing the in- plane magnetization of the LCMO thin film surface. The sample is covered with an MO-indicator film and the red line indicates where the sample ends. The contrast in the image represents areas of strong and weak magnetic fields periodically alternating in the plane of the film and seen as bright and dark areas, respectively

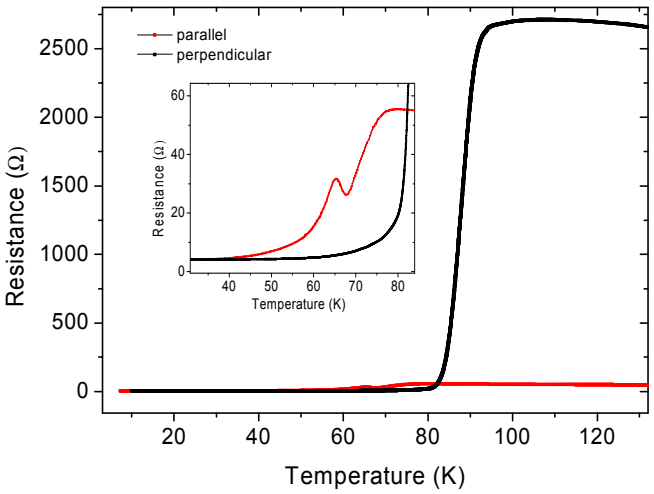

Fig. 5. Temperature dependence of resistance perpendicular and parallel to the stripy domains in the LCMO/YBCO bilayer measured at 0.3 V

These measurements, however, have a common feature of the increase of resistance with decrease of temperature above superconducting transition and the absence of the resistance drop at Curie temperature of LCMO, which is about 250 K. An explanation could be that Curie temperature of LCMO moved to low temperatures due to oxygen non-stoichiometry inferred by the ex-situ deposition, and is now located at the position of the high-resistance peak, where one also start seeing stripy magnetic features in MOI.

Independent magnetization measurements shown in Fig.6 indicate, on the other hand, that the Curie temperature is located approximately at its expected value, about 250 K. More intriguing, in these measurements two different regions are observed. From room temperature and down to

approximately 70 K the magnetization behaves as in a common colossal magnetoresistance material showing establishment of spin polarization below 250 K. The latter temperature is too far from the temperature at which the resistance peak is seen, so common spin polarization could not be the origin of it. Below ≈70 K, susceptibility start, however, increasing again with decrease of temperature.

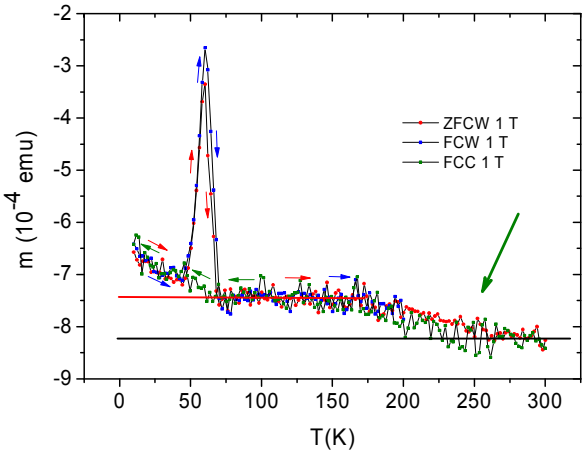

Fig. 6. Magnetic measurements carried out with a DC field of 1 T. Here ZFCW is for zero field cooled sample measured during heating, FCC is for field cooled sample measured during cooling, and FCW is for field cooled measured during heating. The heating/cooling directions are indicated by small arrows. The large green arrow indicates the approximate Curie temperature of LCMO

This paramagnetic increase is due to uncompensated Mn or Cu magnetic moments, as these are the only paramagnetic ions in the compound. The most interesting feature here is, however, very strong peak in magnetization observed between 50 and 70 K. The magnetic phase responsible for this peak, which is seen in a small temperature interval, is likely to be a phase located in or close to the interfaces. This peak is, however, not present when measuring during cooling, indicating that the phase needs low temperatures to be formed, but its behaviour between 50 and 70 K may vary, for example due to change in the direction of magnetic moment. In any case, appearance of this magnetic phase and its evolution coincide in temperature with the position of resistance peak described earlier.

As discussed in [12], a competing process of self-injection of Cooper pairs into LCMO and external injection of spin polarized electrons from LCMO into YBCO takes place when the current is flowing in LCMO/YBCO bilayer with current leads attached to LCMO. The spin polarized electrons suppress the formation of Cooper pairs near the interface with LCMO [5], which may contribute to the voltage dependent resistivity peak that is seen below the superconducting transition.

The overall behaviour may find support in the fact that magnetic ordering is generally more robust in the LCMO, where the exchange energy is typically 1 eV, than in the superconductor, where the exchange energy is typically much lower, 0.01 eV [13]. Due to the half-metallic properties of LCMO, the applied voltage is proportional to the relative shift in density of states for one spin polarization in reference to the Fermi energy. This will allow more spin polarized electrons to enter YBCO as the voltage is increased. One could support this explanation by the increased height of the high-resistivity peak with increasing voltage, best seen in the heating experiments of Fig. 3. All this is relevant to the phase that is in direct contact with superconductor. In our case it is not the common LCMO material with Curie temperature of 250 K, but an interface phase with anomalous magnetism at 50-70 K.

To support this point of view, the x-ray diffraction study was carried out on the bilayer. The collected XRD-pattern is shown in Fig. 7. The film shows quite poor crystallinity compared to other films deposited with PLD, and has a rough surface. The top layers are visible as a shoulder on the right hand side of the main peak from the $SrTiO_3$-substrate. In addition, some unknown peaks with low intensity appear at approximately 30 and 45 degrees. This indicates significant inter-diffusion between the LCMO and YBCO layers forming interface layer with different properties than those of the pure compounds.

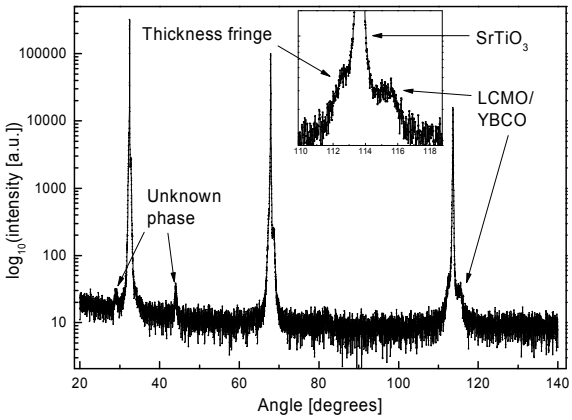

Fig. 7. XRD pattern of the sample. The inset zooms in on the rightmost peak. The different phases are indicated with arrows

Returning to magnetic properties, since the magnetization peak was not observed when measuring with a 0.05 T field, indication is that the magnetic phase layer is very thin, which is also in ideal agreement that it is an interface layer. This may on the other hand just be that the film is very thin compared to the substrate that gives a low magnetic signal.

Further studies of the surface were done with SEM (Fig. 8). Although we see a film on the surface, results from energy dispersive X-ray spectrometry (EDX) measurements do not indicate two separate layers of LCMO and YBCO. A united, approximately 200 nm thick layer enriched with copper is seen near the surface, but no other elements are clearly expressed in the top layer. The background dominance of all other elements and the peak overlapping in the EDX-signal make quantizing

rather difficult. Also, electron beam mainly goes through thin top layers generating very small signal from them. Reducing the energy of the beam increases EDX counts expected from the deposited layers. This study is again in agreement with possible formation of interface layer.

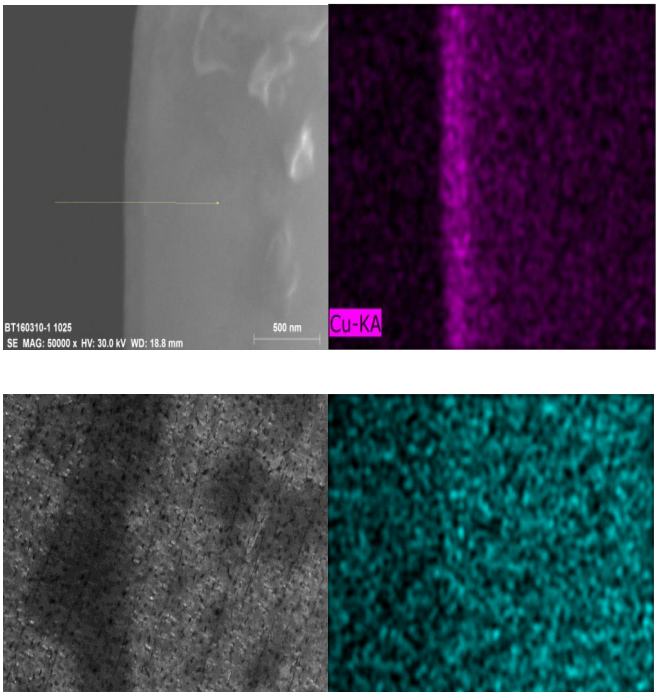

Fig. 8. SEM images (left) and EDX map (right) of a cross section of the film. The lower left image is the surface of the film seen from above

It is necessary to emphasize that the effects observed in this paper are not seen in other experiments on similar systems [14,15]. The main difference between this and other films is the exposure to air between deposition of LCMO and YBCO. Some surface species may have been adsorbed on YBCO when LCMO was deposited, causing interface to equilibrate over time by inter-diffusion of elements, like Cu and Mn. For practical applications, the effect could be reproduced by in-situ deposition of very thin layer of suitable material between YBCO and LCMO. Further investigation of this system is recommended.

IV. Conclusions

An ex-situ LCMO/YBCO bilayer shows anisotropic resistance caused by the appearance of the stripy magnetic domains in LCMO/YBCO interface, which is formed by inter-diffusion of the elements from YBCO and LCMO. An unusual resistance peak appears just below the critical temperature of YBCO and is caused by the interplay between spin polarization and superconductivity at the interface. The magnetism of the interface is strong enough to be seen in both magnetization and magneto-optical experiments.

Acknowledgment

We acknowledge and thank Øystein Slagtern Fjellvåg for help with performing and analyzing XRD experiments, the help from Kristian Blindheim Lausund with performing SEM-analysis on our sample, and Tom Henning Johansen for magneto-optical indicator film.

References

[1] F. Pulizzi, “Spintronics”, Nat. Mater., vol. 11, pp. 367-367, May 2012.

[2] J. Linder, and J.W.A. Robinson, “Superconducting spintronics”, Nat. Phys., vol. 11, pp. 307-315, April 2015.

[3] Y.-P. Shim, and C. Tahan, “Semiconductor-inspired design principles for superconducting quantum computing”, Nat. Commun., vol. 7, pp. 11059, March 2016.

[4] A.M. Goldman, V. Vas’ko, P. Kraus, K. Nikolaev, and V.A. Larkin, “Cuprate/manganite heterostructures”, J. Magn. Magn. Mater., vol. 200, pp. 69-82, December 1999.

[5] P. Mikheenko, M.S. Colclough, C. Severac, R. Chakalov, F. Welhoffer, and C.M. Muirhead, “Effect of spin-polarized injection on the mixed state of YBa2Cu3O7−δ”, Appl. Phys. Lett., vol. 78, pp. 356-358, January 2001.

[6] P. Mikheenko, V.V. Yurchenko, D.A. Cardwell, Y.H. Shi, and T.H. Johansen, “Magneto-optical imaging of superconductors for liquid hydrogen applications”, J. Supercond. Nov. Magn., vol. 26, pp. 1499-1502, December 2012.

[7] Ch. Jooss, J. Albrecht, H. Kuhn, S. Leonhardt, and H. Kronmüller, “Magneto-optical studies of current distributions in high-Tc superconductors”, Rep. Prog. Phys., vol. 65, pp. 651–788, April 2002.

[8] T.H. Johansen, and D.V. Shantsev, “Magneto-optical imaging”, 1st ed., Dordrecht: Kluwer Academic Publishers, 2004.

[9] L.E. Helseth, R.W. Hansen, E.I. Il’yashenko, M. Baziljevich, and T.H. Johansen, “Faraday rotation spectra of bismuth-substituted ferrite garnet films with in-plane magnetization”, Phys. Rev. B, vol. 64, pp. 174406, October 2001.

[10] L.E. Helseth, A.G. Solovyev, R.W. Hansen, E.I. Il’yashenko, M. Baziljevich, and T.H. Johansen, “Faraday rotation and sensitivity of (100) bismuth-substituted ferrite garnet films”, Phys. Rev. B, vol. 66, pp. 064405, August 2002.

[11] S. Soltan, J. Albrecht, and H.-U. Habermeier, “Transport properties of LCMO/YBCO hybrid structures,” Mater. Sci. Eng. B, vol. 144, pp. 15-18, August 2007.

[12] N.-C. Yeh, R.P. Vasquez, C.C. Fu, A.V. Samoilov, Y. Li, and K. Vakili, “Nonequilibrium superconductivity under spin-polarized quasiparticle currents in perovskite ferromagnet-insulator-superconductor heterostructures”, Phys. Rev. B, vol. 60, pp. 10522-10526, October 1999.

[13] R. Werner, C. Raisch, A. Ruosi, B.A. Davidson, P. Nagel, M. Merz, S. Schuppler, M. Glaser, J. Fujii, T. Chassé, R. Kleiner, and D. Koelle, “$YBa_2Cu_3O_7/La_{0.7}Ca_{0.3}MnO_3$ bilayers: Interface coupling and electric transport properties,” Phys. Rev. B, vol. 82, pp. 224509, December 2010.

[14] V. Peña, Z. Sefrioui, D. Arias, C. Leon, J. Santamaria, M. Varela, S. J. Pennycook, and J.L. Martinez, “Coupling of superconductors through a half-metallic ferromagnet: Evidence for a long-range proximity effect”, Phys. Rev. B, vol. 69, pp. 224502, June 2004.

[1] P. Prieto, P. Vivas, G. Campillo, E. Baca, L.F. Castro, M. Varela, C. Ballesteros, J.E. Villegas, D. Arias, C. León, and J. Santamaria, “Magnetism and superconductivity in $La_{0.7}Ca_{0.3}MnO_3/YBa_2Cu_3O_{7-\delta}$ superlattices”, J. Appl. Phys., vol. 89, pp. 8026-8029, June 2001.

E.2 Effect of spin injection from colossal magnetoresistance material into superconducting thin film of $YBa_2Cu_3O_{7-\delta}$

Conference paper sent for peer review for the 2018 international conference: "Nanomaterials: Applications and Properties". Here the author have contributed with obtaining and or analysing transport measurements, MOI, SEM, AFM and EDS of the sample YBCO200nm-LCMO100nm.

Effect of spin injection from colossal magnetoresistance material into superconducting thin film of $YBa_2Cu_3O_{7-\delta}$

T.B. Hjelmeland
Department of Physics,
University of Oslo, P.O.Box 1048, Blindern, 0316
Oslo, Norway
t.b.hjelmeland@fys.uio.no

Y. Volkov
Kiev-Pechersk Lyceum 171
Leipzig street 11A, 01015
Kiev, Ukraine
veg2001@gmail.com

P. Mikheenko*
Department of Physics,
University of Oslo, P.O.Box 1048, Blindern, 0316
Oslo, Norway
*pavlo.mikheenko@fys.uio.no

***Abstract*— By specific design of the sample, in which $SrTiO_3$ substrate is fully covered by a thin film of the colossal magnetoresistive material $La_{0.67}Ca_{0.33}MnO_3$ (LCMO) and the latter is partially covered by high-temperature superconductor $YBa_2Cu_3O_{7-\delta}$ (YBCO), and by using multiple current and voltage contacts, direct evidence of spin injection from LCMO to YBCO is obtained. It is found that spin-polarized electrons injected from LCMO strongly influence not only superconducting, but also normal state of YBCO. The effect of deposition conditions of LCMO and YBCO and the quality of the interface on the spin injection efficiency is clarified. A surprising peak in the temperature dependence of resistance seen on ex-situ sample is explained as combination of two effects: strong influence of spin-polarized electrons on superconductor just below its critical temperature and the interface-controlled shift of Curie temperature of LCMO to low temperatures. Considering expected use of LCMO and YBCO in composite quantum computation circuits, a possibility of their combination with another advanced quantum material, graphene, is explored.**

Keywords—high temperature superconductor; colossal magnetoresistance material; spin injection; nano-magnetism; graphene.

I. INTRODUCTION

With advance of superconducting quantum computing [1], there is renewed interest to higher-temperature superconductors in combination with spin-polarized materials [2], which is stimulated by the attempts to confine quantum processing on nanometer scale making computers more compact, and extend their operation to higher temperatures [3]. Graphene [4] is another important material that demonstrates quantum behaviour even at room temperature. Merging spin-polarized materials, superconductors and graphene would lead to novel quantum devices with enhanced performance and functionality.

Two particular materials: spin-polarized $La_{0.67}Ca_{0.33}MnO_3$ (LCMO) and high-temperature superconductor $YBa_2Cu_3O_{7-\delta}$ (YBCO) are of special interest [5,6], as they have similar crystal lattice and can be prepared epitaxially on top of each other. There are multiple investigations of these compounds and their effect on each other, see, for example [5-8]. However, simple experiments showing where their interaction is strongest are needed and combinations of these materials with graphene should be explored.

LCMO and YBCO are delicate compounds. Small changes in their chemical composition, especially oxygen content, presence of impurities or diffusion of elements through interface, when they are prepared together, can produce unexpected effects, like appearance of stripy magnetic structure and resistance peak below critical temperature of superconductor [9].

In this paper, using specific design of LCMO/YBCO bilayer, we clarify nature of the resistance peak, demonstrate effect of spin injection on superconducting and normal state of YBCO and explore possibility of combining LCMO and YBCO with graphene.

II. EXPERIMENTAL

A bilayer thin-film structure containing LCMO and YBCO was epitaxially grown by pulsed laser deposition on $SrTiO_3$ (STO) substrate. First, the 5x10-mm^2 substrate was fully covered by a 100-nm thick layer of LCMO. After that, using

mask, about half of LCMO layer was covered by a 200-nm layer of YBCO, as is shown in Fig. 1. Six indium contacts were attached to the sample, whose position is also shown on the figure. Some of them were attached to YBCO and some to LCMO. These contacts allow large variety of measurements depending on which of them are used for passing current and which for measuring voltage. For example, using as current contacts I_1 and I_3, charge carriers are forced to flow from LCMO to YBCO, whereas the choice of current contacts I_1, I_2 confines the carriers mainly to YBCO. At a defined current flow, a variety of potential measurements could be done using different potential contacts.

Before attaching contacts, sample was thoroughly investigated, as in [9], by magneto-optical imaging and scanning electron microscopy to insure desirable properties of both materials. In this paper, however, focus is on electrical transport measurements, for which a constant voltage load technique is chosen. The investigation mainly deals with the temperature dependence of the resistance for different parts of the sample.

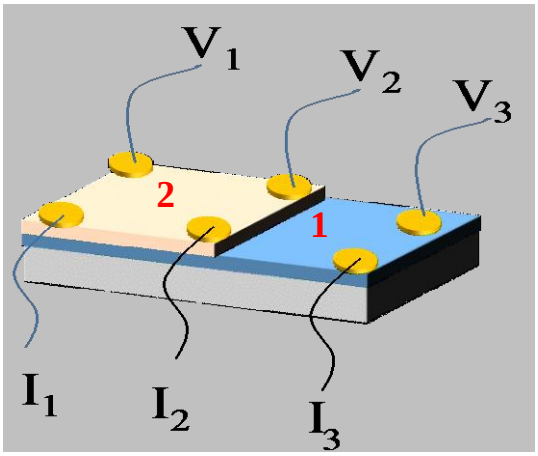

Figure 1: Schematic presentation of the measured sample. The number 1 marks a 100 nm thick layer of LCMO deposited on STO substrate, below. The 200-nm YBCO layer deposited above LCMO, is marked as 2. Several contacts are attached to the sample. Some of them are used for passing current (I_{1-3}) and some for measuring voltage (V_{1-3}).

The sample with attached wires was mounted on a thermally insulated rod, whose temperature was changed by immersing it to, or retracting it from, liquid nitrogen or liquid helium. This was done slowly to avoid appearance of hysteresis on the temperature dependence of resistance.

The constant voltage load to the measuring circuit is simple technique that does not require electronic adjustment of the current due to change of the resistance of the sample in the process of changing the temperature. Its disadvantage is that current does not remain constant during the measurement. However, registering current separately allows obtaining additional information about the sample.

III. Result and Discussion

Typical temperature dependence of resistance of the sample with current flowing through contacts I_1 and I_3 and voltage measured by contacts V_1 and V_3 is shown in Fig. 2. It was recorded at fixed circuit load with voltage of 6 V. Both magnetic (main plot) and superconducting transition (inset) are clearly seen. The magnetic transition is displayed as sharp decrease in resistance at Curie temperature (T_{Curie}) of about 250 K, typical for LCMO [5-8]. The superconducting transition (shown in the magnified part of the curve in the inset) takes place at temperature about 80 K, which is somewhat lower than critical temperature (T_c) of optimally-doped YBCO. This indicates inter-diffusion between YBCO and LCMO, which is, again, typical for the growth of these compounds on top of each other without thin separating barrier in-between. After superconducting transition, at lower temperatures resistance is not zero because in this configuration there is a layer of normal LCMO connected in series with YBCO. The long tail below T_c comes from overlap of R(T) curves of superconducting and spin-polarized materials.

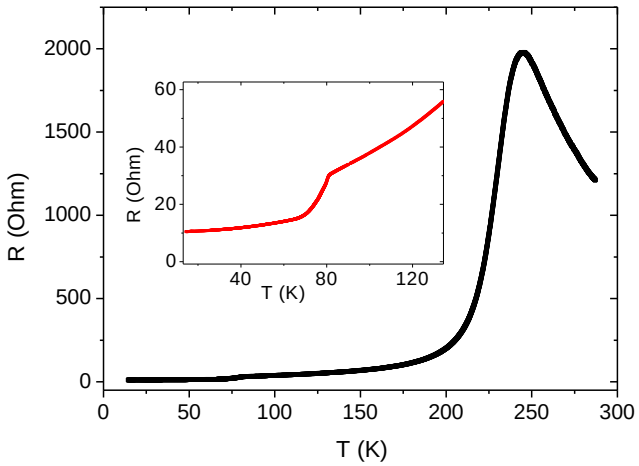

Figure 2: Temperature dependence of resistance of the sample in Fig. 1 with current flowing through contacts I_1 and I_3 and voltage measured by contacts V_1 and V_3. The curve was recorded at the fixed circuit load with voltage of 6 V. Inset shows magnified part of the curve around the superconducting transition of YBCO.

Several curves, similar to that shown in Fig. 2, were recorded at different voltage loads. They also register two transitions with minor systematic variations between them. In the technique, current does not stay constant during temperature scans. Its change with temperature is shown in Fig. 3 for six voltage loads (see color legend in the inset) from 1 to 15 V. The curves in Fig. 3 can also be used to identify temperature of magnetic and superconducting transitions. Indeed, there is sharp increase in current when resistance of LCMO drops below T_{Curie} of about 250 K, and there is another increase in current when YBCO becomes superconducting. To demonstrate this, a magnified part of the curve at 6 V (green color) at temperatures around T_c is shown in Fig. 4.

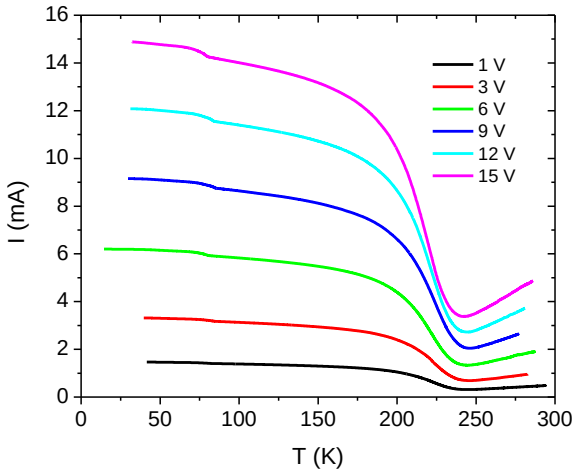

Figure 3: Temperature dependence of current at six constant voltage loads. Their values are shown in the legend in the inset.

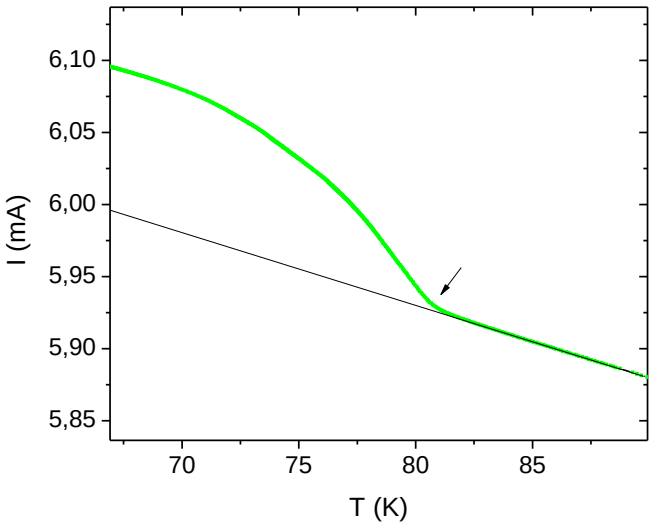

Figure 4: Magnified part of the curve at 6 V in Fig. 3 at temperatures around T_c of YBCO. A thin black line is shown for the guide of eye.

Analysis of the curves similar to those shown in Figs. 2-4 allows obtaining information about the sample as whole. The main advantage of the design in Fig. 1 is, however, ability to explore different parts of the sample at different paths for current, which can either be confined in one of the materials or flow between them.

In Fig. 5, temperature dependence of resistance is shown for the sample in Fig. 1 with current flowing, as in Figs. 2-4, between contacts I_1 and I_3, but voltage measured between contacts V_1 and V_2 that are connected directly to YBCO. Two curves for limiting voltage loads of 1 and 15 V are shown.

Since in Fig. 5 mainly properties of YBCO are measured, resistance shows monotonous quasi-linear decrease with decrease of temperature. Below superconducting transition, resistance is zero. This is typical R(T) curve for a YBCO with one exception: there is small but distinctive anomaly at Curie temperature of LCMO marked by small arrow.

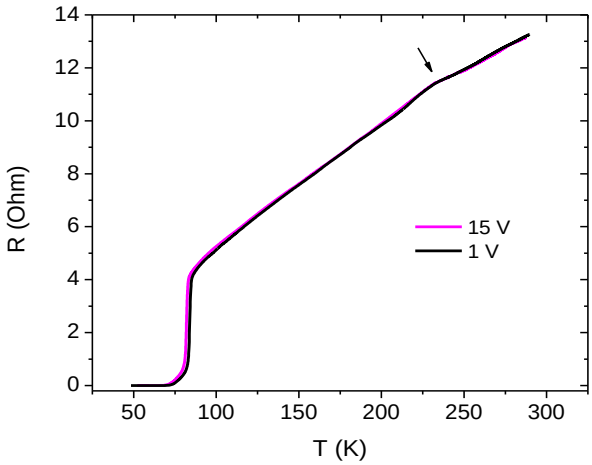

Figure 5: Temperature dependence of resistance for the sample in Fig. 1 with current flowing, as in Figs. 2-4, between contacts I_1 and I_3, but voltage measured between contacts V_1 and V_2. Two curves for voltage of 1 and 15 V are shown.

The shape of anomaly is counterintuitive. Since below YBCO is a layer of LCMO, one would expect decrease of resistance of the bilayer below T_{Curie}, where R of LCMO suddenly drops. Instead, resistance is increasing. It indicates that charge carriers have difficulties of overflowing from LCMO to YBCO at temperatures below T_{Curie}. This is effect of spin injection from LCMO into normal state of YBCO, which is not paid attention to or ignored in the literature, but which is as remarkable as spin injection into superconducting state of YBCO. Indeed, above T_{Curie} about half of electrons have spin up and half spin down both in YBCO and LCMO, so there is no energy cost for the them to overflow from one material to another. In contrast, below T_{Curie}, half of electrons are of spin up and half of spin down in YBCO, but in LCMO all electrons have spin up, and there is energy cost for changing spin population when overflowing between the materials.

One would expect that situation will change if current is not injected from LCMO to YBCO, but simply flows between different parts of YBCO, for example, when it passed through contacts I_1 and I_2. Indeed, in this case increase in resistance does not take place. A comparison between two cases in given in Fig. 6 for a set of load voltages shown in the legend in inset. Bold curves are for current between I_1 and I_3, and thin curves are for current between I_1 and I_2. For a better comparison, a linear curve is subtracted from each set of data. Black arrows indicate beginning of spin polarization transition, while red arrows show position of maximum or minimum in resistance, which develop in presence or absence of spin injection, respectively.

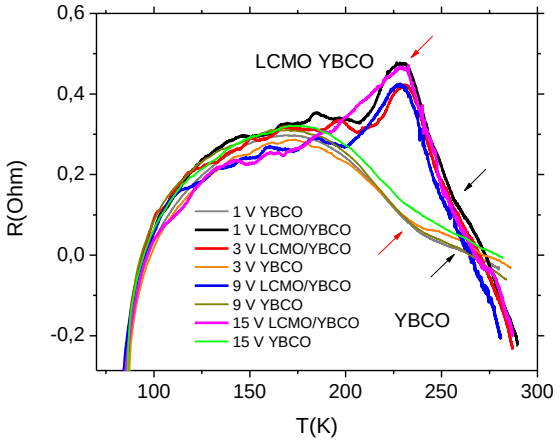

Figure 6: Temperature dependence of resistance for the sample in Fig. 1 with current flowing between contacts I_1 and I_3 (bold lines) and between contacts I_1 and I_2 (thin lines). The voltage is measured between contacts V_1 and V_2. A linear curve is subtracted from each set of data recorded at the same varied voltage loads shown in the legend.

The same technique of changing position of current leads, but keeping potential leads at the same contacts, i.e. injecting spin-polarized electrons or just passing current mainly in YBCO, can be used to demonstrate effect of spin injection on superconducting state of YBCO. Fig. 7 shows temperature dependence of the resistance of YBCO, measured between contacts V_1 and V_2, in the vicinity of the superconducting transition. In this experiment, current is passed through the contacts I_1 and I_3 (black curves) or I_1 and I_2 (red) at four voltage loads of 1, 3, 9 and 15 V. Black curves represent case of forceful spin injection, while red curves correspond to current mainly flowing in YBCO (some overflow of current to LCMO is still possible). It is clear that spin injection strongly affects superconducting transition and its influence increases with increase of the voltage load.

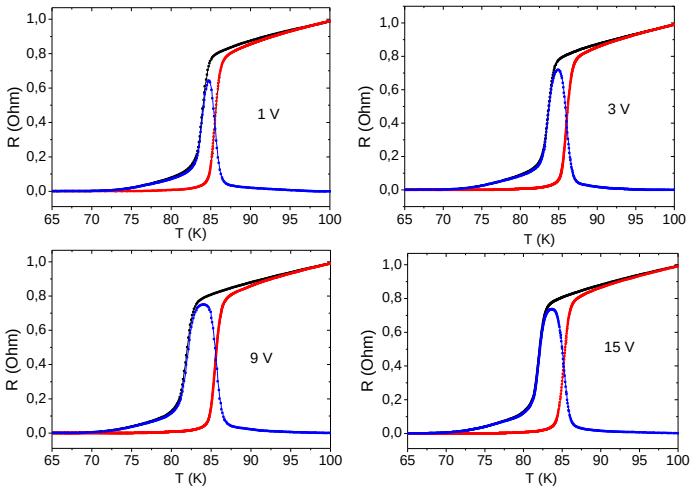

Figure 7: Temperature dependence of the resistance of YBCO measured between contacts V_1 and V_2 in the vicinity of superconducting transition, for the current flowing through the contacts I_1 and I_3 (black curves) and I_1 and I_2 (red). Curves are for four values of voltage load from 1 to 15 V shown in subplots.

Blue curves in Fig. 7 are the difference curves between black and red lines. These curves show the addition resistance due to the spin injection. One can see that effect of spin injection is strongest just below T_c, where superconductor is relatively weak. The addition resistance is overlapped with red curves resulting in the apparent shift of superconducting transition. Such a behavior explains additional resistance peak observed in [9]. One of the curves showing this peak is plotted in Fig. 8.

The sample in [9] was prepared ex-situ, i.e. deposition of LCMO above YBCO took place after removing sample from the deposition chamber. Due to modification of interface in air, T_{Curie} of LCMO shifted to temperature below T_c of YBCO. At the decrease of temperature, first superconducting transition takes place with corresponding drop in resistance at about 90 K. After that, spin-polarization transition starts in LCMO forming the peak similar to that shown by blue curves in Fig. 7. It is important to note that such peak can only be seen if T_{Curie} is close to T_c.

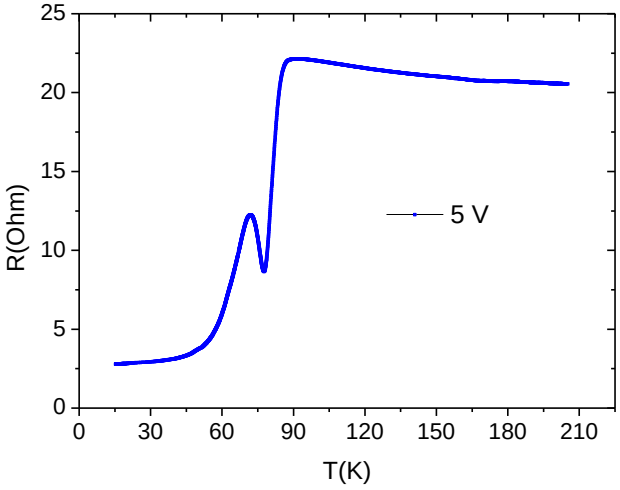

Figure 8: Temperature dependence of resistance for an ex-situ LCMO/YBCO bilayer showing peak effect below superconducting transition.

To extend the above activity to quantum superconducting circuits expected to operate at high temperatures, a combination of YBCO and LCMO with graphene [4] needs to be explored. In this paper, the latter was taken in form of nano-plates in a water solution. A drop of the solution was first deposited to YBCO covering its whole area between contacts V_1, V_2, I_1 and I_2. It was quickly dried to avoid possible interaction of YBCO with water. The result, however, was nearly complete suppression of superconducting transition, as it is shown in Fig. 9 in semi-logarithmic scale. The resistance measured between V_1 and V_2, with current flowing between I_1 and I_2, increases more than one order of magnitude exposing the resistance of LCMO below YBCO with its characteristic drop at T_{Curie} of about 250 K.

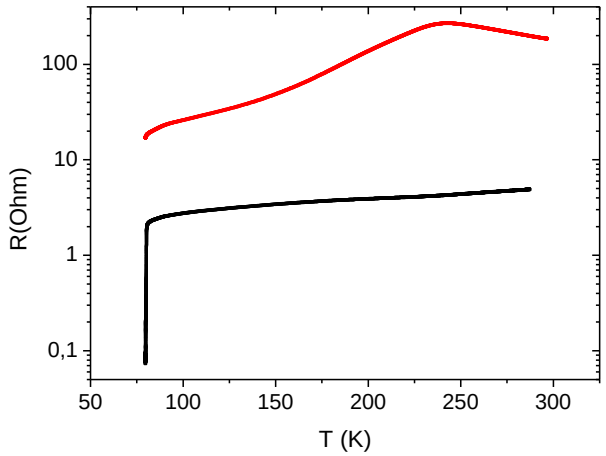

Figure 9: Temperature dependence of the resistance of YBCO measured between contacts V_1 and V_2 after deposition of the layer of graphene (red curve) and before the deposition (black curve). The current is flowing between contacts I_1 and I_2. The axis of resistance is in the logarithmic scale.

In contrast to YBCO, the influence of graphene on LCMO is very moderate. In Fig. 10, temperature dependence of the resistance of LCMO in the uncovered by YBCO area is shown before the deposition of graphene (black curve), after the deposition of first graphene layer (red curve) and the second layer (green curve). The first layer of graphene only slightly increases resistance of LCMO not shifting T_{Curie}. Second layer slightly shifts T_{Curie} to a lower temperature. A small decrease in resistance comparable with red curve is also registered for the green curve, which is probably due to contribution of the conductance of graphene.

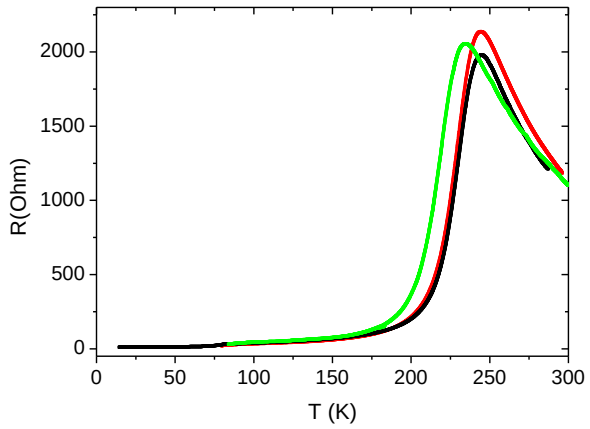

Figure 10: Temperature dependence of the resistance of LCMO in the uncovered by YBCO area before the deposition of graphene (black curve), after the deposition of first graphene layer (red curve) and the second layer (green curve).

In the experiments with graphene, it appears to be very harmful for YBCO. The influence of water still cannot be excluded, and the non-water solutions of graphene nanoflakes should be tried. The influence of graphene on LCMO is very moderate.

IV. Summary

A detailed study of in-situ YBCO/LCMO bilayer by electrical transport measurements in wide range of temperatures has been performed using an array of current and potential leads in the sample partially covered by YBCO. Effect of spin injection from LCMO on normal and superconducting state of YBCO was clearly demonstrated, and unusual peak in resistance appearing below superconducting transition of YBCO in ex-situ sample has been explained. The influence of graphene on YBCO and LCMO was investigated showing that graphene can be extremely harmful for YBCO, but its influence on LCMO is very moderate.

References

[1] D. Castelvecchi, "Quantum cloud goes commercial," Nature, vol. 543, p. 159, March 2017.

[2] J. Linder and J.W.A. Robinson, "Superconducting spintronics," Nat. Phys., vol. 11, pp. 307-315, August 2015.

[3] Y.-P. Shim and C. Tahan, "Semiconductor-inspired design principles for superconducting quantum computing," Nat. Commun., vol. 7, pp. 11059, March 2016

[4] A.K. Geim, K.S. Novoselov, "The rise of graphene," Nature Materials, vol. 6, pp. 183–191, March 2007.

[5] R. Werner, C. Raisch, A. Ruosi, B. A. Davidson, P. Nagel, M. Merz, S. Schuppler, M. Glaser, J. Fujii, T. Chassé, R. Kleiner, and D. Koelle., "$YBa_2Cu_3O_7/La_{0.7}Ca_{0.3}MnO_3$ bilayers: Interface coupling and electric transport properties," Physical Review B, vol 82, 224509, December 2010.

[6] N.C. Yeh, R. P. Vasquez, C. C. Fu, A. V. Samoilov, and K. Vakili, "Nonequilibrium superconductivity under spin-polarized quasiparticle currents in perovskite ferromagnet-insulator-superconductor heterostructures," Physical Review B, vol 60, pp. 10522-10526,1999.

[7] P. Mikheenko, M.S. Colclough, C. Severac, R. Chakalov, F. Welhoffer and C.M. Muirhead, "Effect of spin-polarized injection on the mixed state of $YBa_2Cu_3O_{7-\delta}$," Appl. Phys. Lett., vol. 78, pp. 356, November 2001.

[8] S.Soltan, J. Albrecht, and H.-U. Habermeier, "Transport properties of LCMO/YBCO hybrid structures," Materials Science and Engineering B, vol. 144, pp. 15-18, 2007.

[9] A.S. Fjellvåg, T.B. Hjelmeland, H.J. Mollatt, T. Qureishy, P. Mikheenko, "Interplay between spin polarization and superconductivity in an ex-situ bilayer $La_{0.67}Ca_{0.33}MnO_3$ - $YBa_2Cu_3O_{7-x}$," In Proceedings of the 2017 IEEE 7th International Conference on Nanomaterials: Applications & Properties (NAP-2017). IEEE. ISBN 978-1-5386-2810-2. Part 2., pp. 02NTF02-1 - 02NTF02-5, 2017.

Bibliography

[1] Magnetisation and superconductors. https://commons.wikimedia.org/wiki/File:Magnetisation_and_superconductors.png. Accessed: 2017-10-27.

[2] Magnetoelectronics. http://nptel.ac.in/courses/115103038/module2/lec8/2.html. Accessed: 2018-02-10.

[3] Nanoscale function group. http://www.nanofunction.org/images/afmschematic.jpg. Accessed: 2018-01-05.

[4] The nobel prize in physics 1913: Heinke kamerlingh onnes. https://www.nobelprize.org/nobel_prizes/physics/laureates/1913. Accessed: 2018-01-26.

[5] Piezoelectric materials: Crystal orientation and poling direction. https://www.comsol.com/blogs/piezoelectric-materials-crystal-orientation-poling-direction/. Accessed: 2018-01-26.

[6] Reflection high-energy electron diffraction. https://en.wikipedia.org/wiki/Reflection_high-energy_electron_diffraction. Accessed: 2018-01-23.

[7] Superfluidita, superconduttivita, solitoni. http://www.scienzenoetiche.it/synthesis/fisica_quantistica/11_superfluidita_superconduttivita.php. Accessed: 2017-10-21.

[8] Thin film. https://www.wmi.badw.de/methods/thin_film_deposition.htm. Accessed: 2018-01-22.

[9] Unfinished history of superconductivity. http://aappsbulletin.org/myboard/read.php?id=18&Page=5&Board=featurearticles&FindIt=&FindText=. Accessed: 2018-02-8.

[10] Yba2cu3o7. http://hiroi.issp.u-tokyo.ac.jp/data/crystal_gallery/Pages/10.html. Accessed: 2018-02-02.

[11] John Bardeen, Leon N Cooper, and John Robert Schrieffer. Theory of superconductivity. *Physical Review*, 108(5):1175, 1957.

[12] J George Bednorz and K Alex Müller. Possible high T_c superconductivity in the Ba-La-Cu-O system. *Zeitschrift für Physik B Condensed Matter*, 64(2):189–193, 1986.

[13] Francis Beech, S Miraglia, A Santoro, and RS Roth. Neutron study of the crystal structure and vacancy distribution in the superconductor $Ba_2YCu_3O_{9-\delta}$. *Physical Review B*, 35(16):8778, 1987.

[14] Karl-Heinz Bennemann and John B Ketterson. *Superconductivity: Volume 1: Conventional and Unconventional Superconductors Volume 2: Novel Superconductors*. Springer Science & Business Media, 2008.

[15] Stephen J Blundell. *Superconductivity: a very short introduction*. OUP Oxford, 2009.

[16] P. Bruzzone, R. Wesche, D. Uglietti, and N. Bykovsky. High temperature superconductors for fusion at the Swiss Plasma Center. *Nuclear Fusion*, 57(8):085002, 2017.

[17] Henning Bubert, John C Rivière, Heinrich F Arlinghaus, Herbert Hutter, Holger Jenett, Peter Bauer, Leopold Palmetshofer, Laszlo Fabry, Siegfried Pahlke, Alfred Quentmeier, et al. *Surface and Thin-Film Analysis*. Wiley Online Library, 2002.

[18] Alexandre I Buzdin. Proximity effects in superconductor-ferromagnet heterostructures. *Reviews of modern physics*, 77(3):935, 2005.

[19] JMD Coey, MV Viret, and S Von Molnar. Mixed-valence manganites. *Advances in physics*, 58(6):571–697, 2009.

[20] Elbio Dagotto, Takashi Hotta, and Adriana Moreo. Colossal magnetoresistant materials: the key role of phase separation. *Physics reports*, 344(1-3):1–153, 2001.

[21] Michel H Devoret and Robert J Schoelkopf. Superconducting circuits for quantum information: an outlook. *Science*, 339(6124):1169–1174, 2013.

[22] Robert Eason. *Pulsed laser deposition of thin films: applications-led growth of functional materials*. John Wiley & Sons, 2007.

[23] Changming Fang, G A. de Wijs, and R A. de Groot. Spin-polarization in half-metals (invited). 91:8340–8344, 05 2002.

[24] AS Fjellvåg, TB Hjelmeland, HJ Mollatt, T Qureishy, and P Mikheenko. Interplay between spin polarization and superconductivity in an ex-situ bilayer $La_{0.67}Ca_{0.33}MnO_3$ — $YBa_2Cu_3O_{7-\delta}$. In *Nanomaterials: Application & Properties (NAP), 2017 IEEE 7th International Conference*, pages 02NTF02–1. IEEE, 2017.

[25] AM Goldman, V Vas' ko, P Kraus, K Nikolaev, and VA Larkin. Cuprate/-manganite heterostructures. *Journal of magnetism and magnetic materials*, 200(1-3):69–82, 1999.

[26] Joseph I Goldstein, Dale E Newbury, Joseph R Michael, Nicholas WM Ritchie, John Henry J Scott, and David C Joy. *Scanning electron microscopy and X-ray microanalysis*. Springer, 2017.

[27] TYChen Group. Andreev reflection spectroscopy. http://chen.physics.asu.edu/research/ARS.html. Accessed: 2018-04-16.

[28] HZ Guo, A Gupta, Jiandi Zhang, M Varela, and SJ Pennycook. Effect of oxygen concentration on the magnetic properties of La_2CoMnO_6 thin films. *Applied Physics Letters*, 91(20):202509, 2007.

[29] A-M Haghiri-Gosnet and J-P Renard. CMR manganites: physics, thin films and devices. *Journal of Physics D: Applied Physics*, 36(8):R127, 2003.

[30] Thomas Heinzel. *Mesoscopic electronics in solid state nanostructures*. John Wiley & Sons, 2008.

[31] LE Helseth, RW Hansen, EI Il'yashenko, M Baziljevich, and TH Johansen. Faraday rotation spectra of bismuth-substituted ferrite garnet films with in-plane magnetization. *Physical Review B*, 64(17):174406, 2001.

[32] Kun-Rok Jeon, Chiara Ciccarelli, Andrew J Ferguson, Hidekazu Kurebayashi, Lesley F Cohen, Xavier Montiel, Matthias Eschrig, Jason WA Robinson, and Mark G Blamire. Enhanced spin pumping into superconductors provides evidence for superconducting pure spin currents. *Nature materials*, April 2018.

[33] Tom H Johansen and Daniel Shantsev. *Magneto-optical imaging*, volume 142. Kluwer Academic Publisher and IOS Press, 2003.

[34] Ch Jooss, J Albrecht, H Kuhn, S Leonhardt, and H Kronmüller. Magneto-optical studies of current distributions in high-T_c superconductors. *Reports on progress in Physics*, 65(5):651, 2002.

[35] JD Jorgensen, MA Beno, Di G Hinks, L Soderholm, KJ Volin, RL Hitterman, JD Grace, Ivan K Schuller, CU Segre, K Zhang, et al. Oxygen ordering and the orthorhombic-to-tetragonal phase transition in $YBa_2Cu_3O_{7-x}$. *Physical Review B*, 36(7):3608, 1987.

[36] Charles Kittel. *Introduction to solid state physics*. Wiley, 2005.

[37] Thaddeus D Ladd, Fedor Jelezko, Raymond Laflamme, Yasunobu Nakamura, Christopher Monroe, and Jeremy Lloyd O'Brien. Quantum computers. *Nature*, 464(7285):45, 2010.

[38] Jacob Linder and Jason WA Robinson. Superconducting spintronics. *Nature Physics*, 11(4):307, 2015.

[39] Fritz London and Heinz London. The electromagnetic equations of the supraconductor. In *Proc. R. Soc. Lond. A*, volume 149, pages 71–88. The Royal Society, 1935.

[40] Charles E Lyman, Dale E Newbury, Patrick Echlin, David C Joy, Eric Lifshin, Linda Sawyer, Joseph R Michael, and Joseph I Goldstein. *Scanning electron microscopy and X-ray microanalysis*. Springer, New York, 3rd ed. edition, 2003.

[41] Philippe Mangin and Rémi Kahn. *Superconductivity: An Introduction*. Springer, 2016.

[42] Walther Meissner and Robert Ochsenfeld. Ein neuer effekt bei eintritt der supraleitfähigkeit. *Naturwissenschaften*, 21(44):787–788, 1933.

[43] P Mikheenko. Superconductivity for hydrogen economy. In *Journal of Physics: Conference Series*, volume 286, page 012014. IOP Publishing, 2011.

[44] HC Montgomery. Method for measuring electrical resistivity of anisotropic materials. *Journal of applied physics*, 42(7):2971–2975, 1971.

[45] B Nadgorny, II Mazin, M Osofsky, RJ Soulen Jr, P Broussard, RM Stroud, DJ Singh, VG Harris, A Arsenov, and Ya Mukovskii. Origin of high transport spin polarization in $La_{0.7}Sr_{0.3}MnO3$: Direct evidence for minority spin states. *Physical Review B*, 63(18):184433, 2001.

[46] Georg Simon Ohm. *Die galvanische Kette, mathematisch bearbeitet*. TH Riemann, 1827.

[47] Heinke Kamerlingh Onnes. Commun. Phys. Lab. Univ. Leiden, (29), 1911.

[48] Ninos Poli, Jan Petter Morten, Mattias Urech, Arne Brataas, David B Haviland, and Vladislav Korenivski. Spin injection and relaxation in a mesoscopic superconductor. *Physical review letters*, 100(13):136601, 2008.

[49] CHL Quay, D Chevallier, C Bena, and M Aprili. Spin imbalance and spin-charge separation in a mesoscopic superconductor. *Nature Physics*, 9(2):84, 2013.

[50] Rudolf Reichelt. Scanning electron microscopy. In *Science of microscopy*, pages 133–272. Springer, 2007.

[51] C Ritter, MR Ibarra, JM De Teresa, PA Algarabel, C Marquina, J Blasco, J Garcia, S Oseroff, and SW Cheong. Influence of oxygen content on the structural, magnetotransport, and magnetic properties of $LaMnO_{3+\delta}$. *Physical Review B*, 56(14):8902, 1997.

[52] Ajay Kumar Saxena. *High-Temperature Superconductors*, volume 125. Springer Science & Business Media, 2012.

[53] P Schiffer, AP Ramirez, W Bao, and SW Cheong. Low temperature magnetoresistance and the magnetic phase diagram of $La_{1-x}Ca_xMnO_3$. *Physical Review Letters*, 75(18):3336, 1995.

[54] Ram Gopal Sharma. *Superconductivity: Basics and applications to magnets*, volume 214. Springer, 2015.

[55] WC Sheets, AE Smith, MA Subramanian, and W Prellier. Effect of oxygen concentration on the structural and magnetic properties of $LaRh_{1/2}Mn_{1/2}O_3$ thin films. *Journal of Applied Physics*, 105(2):023915, 2009.

[56] S Soltan, J Albrecht, and H-U Habermeier. Ferromagnetic/superconducting bilayer structure: A model system for spin diffusion length estimation. *Physical Review B*, 70(14):144517, 2004.

[57] S Soltan, J Albrecht, and H-U Habermeier. Spin-polarized quasiparticle injection effects in YBCO thin films. *Solid state communications*, 135(7):461–465, 2005.

[58] S Soltan, J Albrecht, and H-U Habermeier. Transport properties of LCMO/YBCO hybrid structures. *Materials Science and Engineering: B*, 144(1-3):15–18, 2007.

[59] Soltan Soltan. *Interaction of Superconductivity and Ferromagnetism in YBCO-LCMO Heterostructures*. Cuvillier Verlag, 2005.

[60] M Spankova, V Strbik, E Dobrocka, S Chromik, M Sojkova, DN Zheng, and J Li. Characterization of epitaxial LSMO thin films with high Curie temperature prepared on different substrates. *Vacuum*, 126:24–28, 2016.

[61] Marric Stephens. Superconducting quantum computer achieves 10-qubit entanglement. http://physicsworld.com/cws/article/news/2017/nov/10/superconducting-quantum-computer-achieves-ten-qubit-entanglement. Accessed: 2018-02-02.

[62] Eiji Takayama-Muromachi, Yoshishige Uchida, Motohiko Ishii, Takaho Tanaka, and Katsuo Kato. High T_c superconductor $YBa_2Cu_3O_y$ –oxygen content vs T_c relation–. *Japanese Journal of Applied Physics*, 26(7A):L1156, 1987.

[63] Evgeny Y Tsymbal and David G Pettifor. Perspectives of giant magnetoresistance. In *Solid state physics*, volume 56, pages 113–237. Elsevier, 2001.

[64] J Volger. Further experimental investigations on some ferromagnetic oxidic compounds of manganese with perovskite structure. *Physica*, 20(1-6):49–66, 1954.

[65] T Wakamura, N Hasegawa, K Ohnishi, Y Niimi, and YoshiChika Otani. Spin injection into a superconductor with strong spin-orbit coupling. *Physical review letters*, 112(3):036602, 2014.

[66] Taro Wakamura, H Akaike, Y Omori, Y Niimi, S Takahashi, A Fujimaki, S Maekawa, and Y Otani. Quasiparticle-mediated spin Hall effect in a superconductor. *Nature materials*, 14(7):675, 2015.

[67] John R Waldram. *Superconductivity of metals and cuprates*. CRC Press, 1996.

[68] Maw-Kuen Wu, Jo R Ashburn, ClJ Torng, Ph H Hor, Rl L Meng, Lo Gao, Z Jo Huang, YQ Wang, and aCW Chu. Superconductivity at 93 K in a new mixed-phase Y-Ba-Cu-O compound system at ambient pressure. *Physical Review Letters*, 58(9):908, 1987.

[69] Hyunsoo Yang, See-Hun Yang, Saburo Takahashi, Sadamichi Maekawa, and Stuart SP Parkin. Extremely long quasiparticle spin lifetimes in superconducting aluminium using MgO tunnel spin injectors. *Nature materials*, 9(7):586, 2010.

[70] Liu Yu-Kuai, Yin Yue-Wei, and Li Xiao-Guang. Colossal magnetoresistance in manganites and related prototype devices. *Chinese Physics B*, 22(8):087502, 2013.

[71] YG Zhao, YH Wang, GM Zhang, B Zhang, XP Zhang, CX Yang, PL Lang, MH Zhu, and PC Guan. Universal behavior of giant electroresistance in epitaxial $La_{0.67}Ca_{0.33}MnO_3$ thin films. *Applied Physics Letters*, 86(12):122502, 2005.